SCUOLA DI DOTTORATO

UNIVERSITÀ DEGLI STUDI DI MILANO-BICOCCA

Department of Biotechnology and Biosciences

PhD program in Biology and Biotechnology

Cycle XXXI

Structural and functional analyses of an ice-binding protein from an Antarctic bacterium

Surname: Mangiagalli Name: Marco

Registration number: 735393

Tutor: Prof. Marina Lotti

Coordinator: Prof. Paola Branduardi

ACADEMIC YEAR 2017/2018

Summary

Abstract

Ice-binding proteins (IBPs) are characterized by the ability to control the growth of ice crystals. IBPs are active in increasing thermal hysteresis (TH) gap as they decrease the freezing point of water. On the other hand, IBPs can inhibit ice recrystallization (IRI) and stabilize small ice crystals at the expense of the harmful, large ones. IBPs have been identified in several organisms including higher Eukaryotes and microorganisms such as bacteria, yeasts and algae. Although IBPs share the ability to bind ice crystals, proteins from different sources present different 3D structures, from α-helix to β-solenoid proteins.

This thesis is focused on the structural and functional characterization of *Efc*IBP, a bacterial IBP identified by metagenomic analysis of the Antarctic ciliate *Euplotes focardii* and the associated consortium of non-cultivable bacteria. The 3D structure of *Efc*IBP, solved by X-ray crystallography, consists in a β-solenoid with an α-helix aligned along the axis of the β-helix. It is possible to distinguish three different faces: A, B and C. Docking simulations suggest that B and C faces are involved in ice binding. This hypothesis was tested by the rational design of six variants that were produced and assayed for their activity. Overall, these experiments indicate that both solenoid faces contribute to the activity of *Efc*IBP.

*Efc*IBP displays remarkable IRI activity at nanomolar concentration and a TH activity of 0.53°C at the concentration of 50 μM. The atypical combination between these two activities could stem from the ability of this protein to bind ice crystals through two faces of the solenoid. In the presence of *Efc*IBP, ice crystals show a hexagonal trapezohedron shape within the TH gap, and a unique "Saturn-shape" below the freezing point. A chimeric protein consisting of the fusion between *Efc*IBP and the green fluorescent protein was used to deeper investigate on this aspects by analyses of fluorescence ice plane affinity and binding kinetics. Overall, experimental data suggest that the *Efc*IBP unique pattern of ice growth and burst are due to its high rate of binding at the basal and the pyramidal near-basal planes of ice crystals. These data, together with the signal sequence for the secretion, suggest that *Efc*IBP is secreted in local environment where it becomes active in increasing the habitable space.

In conclusion, *Efc*IBP is a new type of IBP with unusual properties of ice shaping and IRI activity. This study opens new scenarios in the field of IBPs by contributing to identify a new class of moderate IBPs potentially exploitable as cryoprotectants in several fields, such as cryobiology and food science.

Riassunto

Una proteina in grado di legare i cristalli di ghiaccio è definita proteina legante il ghiaccio o IBP acronimo dall'inglese *ice-binding protein*. Le IBP grazie alla loro capacità di abbassare il punto di congelamento dell'acqua, aumentando il *gap* di isteresi termica (TH). Questo intervallo è definito come la differenza tra il punto di fusione e di congelamento dell'acqua. La seconda attività delle IBP è l'inibizione della ricristallizzazione del ghiaccio (*ice recrystallization inhibition*, IRI). Infatti, queste proteine stabilizzano i piccoli cristalli di ghiaccio impedendo la formazione di cristalli di ghiaccio di grosse dimensioni che sono dannosi per le cellule. Le IBP sono state identificate in numerosi organismi tra cui pesci, insetti, batteri, alghe e lieviti. Queste proteine rappresentano un esempio di evoluzione convergente, infatti tutte le IBP condividono lo stesso meccanismo di legame con il ghiaccio nonostante una sorprendente diversità strutturale e funzionale.

Questo lavoro di tesi è focalizzato sulla caratterizzazione funzionale e strutturale di *Efc*IBP, una IBP batterica identificata da analisi di metagenomica effettuate sul ciliato Antartico *Euplotes focardii* e sul consorzio batterico ad esso associato. La struttura 3D di *Efc*IBP è stata risolta mediante cristallografia ai raggi X e consiste in un β-solenoide con un α-elica parallela all'asse principale della proteina. L'analisi strutturale ha permesso di identificare tre diverse facce del solenoide denominate A, B e C. Simulazioni di *docking* suggeriscono che *Efc*IBP è in grado di legare i cristalli di ghiaccio tramite le facce B e C del solenoide. Questa ipotesi è stata verificata attraverso la progettazione razionale di 6 varianti che sono state prodotte e saggiate per la loro attività. In generale, questi risultati indicano che *Efc*IBP è in grado di legare i cristalli di ghiaccio attraverso le facce B e C del solenoide. Questa peculiarità strutturale si riflette in un'insolita combinazione di attività di IRI e TH. Infatti, *Efc*IBP presenta una notevole attività di IRI in un intervallo di concentrazione nanomolare e una attività di isteresi termica di 0.53°C alla concentrazione di 50 μM che la rende una IBP moderata. All'interno del gap di TH, i cristalli di ghiaccio presentano una forma esagonale, mentre a temperature al di sotto della temperatura di congelamento presentano una forma a "Saturno". La proteina chimerica formata dalla "*green fluorescent protein*" e da *Efc*IBP è stata utilizzata per determinare a quali

piani del cristallo di ghiaccio la proteina è in grado di legarsi e con quale cinetica. I dati sperimentali suggeriscono che le peculiarità funzionali di *Efc*IBP sono dovute alla sua capacità di legare velocemente i piani basali e piramidali del cristallo di ghiaccio. Questi dati, insieme alla presenza di una sequenza segnale per la secrezione, suggeriscono che *Efc*IBP è secreta e svolge la funzione di mantenere liquido l'ambiente circostante aumentando lo spazio vitale. In conclusione, *Efc*IBP è un nuovo tipo di IBP con proprietà insolite di legame al ghiaccio e di attività di IRI.

Questo studio ha contribuito ad identificare una nuova classe di IBP moderate che potrebbero essere sfruttate come crioprotettori in diversi settori come la criobiologia e quello alimentare.

Co-Authorship

Section entitled: **"**Cryo-protective effect of an ice-binding protein derived from Antarctic bacteria" is co-authored with Maya Bar-Dolev, Pietro Tedesco, Antonino Natalello, Aleksei Kaleda, Stefania Brocca, Donatella de Pascale, Sandra Pucciarelli, Cristina Miceli, Ido Braslavsky and Marina Lotti, and has been published as:

Mangiagalli, M., Bar-Dolev, M., Tedesco, P., Natalello, A., Kaleda, A., Brocca, S., de Pascale, D., Pucciarelli, S., Miceli, C., Braslavsky, I. & Lotti, M. (2017). Cryo-protective effect of an ice-binding protein derived from Antarctic bacteria. The FEBS journal, 284(1), 163-177. doi:10.1111/febs.13965

Section entitled:" Structure of a bacterial ice binding protein with two faces of interaction with ice" is co-authored with Guy Sarusi, Aleksei Kaleda, Maya Bar Dolev, Valentina Nardone, Vittoria Federica Vena, Ido Braslavsky, Marina Lotti and Marco Nardini and has been published as:

Mangiagalli, M., Sarusi, G., Kaleda, A., Bar Dolev, M., Nardone, V., Vena, V. F., Braslavsky, I. Lotti, M. & Nardini, M. (2018). Structure of a bacterial ice binding protein with two faces of interaction with ice. The FEBS journal, 285(9), 1653-1666. doi:10.1111/febs.14434

Section entitled: "Saturn-shaped ice burst pattern and fast basal binding of an ice-binding protein from an Antarctic bacterial consortium" is co-authored with Aleksei Kaleda, Lotem Haleva, Guy Sarusi, Tova Pinsky, Maya Bar Dolev, Marina Lotti, Marco Nardini and Ido Braslavsky and has been published as:

Kaleda, A., Haleva, L., Sarusi, G., Pinsky, T., Mangiagalli, M., Bar-Dolev, M., Lotti, M., Nardini, M., & Braslavsky, I. (2018). Saturn-shaped ice burst pattern and fast basal binding of an ice-binding protein from an Antarctic bacterial consortium. Langmuir. doi: 10.1021/acs.langmuir.8b01914

Abbreviations

AFP: antifreeze protein; **AFGP**: antifreeze glycoprotein; **CPA**: cryoprotective agent; CFU: colony forming unit; ***Col*AFP**: *Colwellia* sp. strain SLW05 antifreeze protein; **DUF**: domain of unknown function; ***Efc*IBP**: *Euplotes focardii* bacterial consortium ice binding protein; ***Fc*IBP11**: *Fragilariopsis cylindrus* ice binding protein; **FIPA**: fluorescence based ice plane affinity; ***Ff*IBP**: *Flavobacterium frigoris* PS1 ice binding protein; **FT**: freezing and thawing; **GFP**: green fluorescent protein; **HGT**: horizontal gene transfer; **IBPv**: *Flavobacteriaceae* bacterium 3519-10 ice binding protein; **IBP**: ice binding protein; **IBS**: ice binding site; **INP**: ice nucleation proteins; **IRI**: ice recrystallization inhibition; **ISOCOMID**: isothermally-cooled microfluidic device; **LB**: Luria–Bertani; ***Le*IBP**: *Leucosporidium* sp. AY30 ice binding protein; **MCF**: microfluidic cold finger device; **MpIBP**: *Marinomonas primoriensis* ice binding protein; **PB**: phosphate buffer; ***Sf*IBP_1**: *Shewanella frigidimarina* ice binding protein; **TB**: terrific broth; **TH**: thermal hysteresis; ***Tis*AFP6**: *Typhula ishikariensis* antifreeze protein isoform 6; ***Tis*AFP8**: *Typhula ishikariensis* antifreeze protein isoform 8; **TRITC**: tetramethylrhodamine; **wt**: wild type.

1.Introduction

1.1 Life in cold environments

Cryosphere represents approximately 80% of the Earth biosphere and it is characterized by temperatures below 5°C. Cryosphere includes the polar regions, ocean sediments and glaciers [1, 2]. Cold environments are inhabited by psychrophilic and psycrhotollerant organisms, the first ones having an optimal grow temperature below 15°C, the second ones growing optimally in the range between 20-25°C and surviving below 0°C [2]. These organisms have developed several strategies to thrive in cold environments. Among these, the modification of cell membranes to increase their fluidity, and the overexpression of anti-oxidative enzymes, which counteract reactive oxygen species induced by the low solubility of gasses at the cold [1-3].

Organisms living in some cold environments are constantly exposed to sub-zero temperatures, where the main challenge is to contrast the formation of ice crystals, both inside and outside the cells [1]. Generally, the formation of ice crystals is lethal since induces osmotic unbalancing, which damages cell membranes and causes their lysis [4]. The cryoprotective "apparatus" of these organisms includes the production of cryoprotectant molecules such as glycine, betaine and mannitol, which decrease the freezing point of the cytoplasm in a colligative manner [5]. A complementary strategy consists in the production of ice-binding proteins (IBPs), which bind ice crystals and block their grow in a non-colligative manner [6, 7]. The first IBP was discovered in the late 1960's and described as antifreeze protein (AFP) because of its ability to depress the freezing point of biological fluids [8].

1.2 Activity of IBPs

The ability of IBPs to bind ice crystals is reflected in four main activities: thermal hysteresis (TH), inhibition of ice recrystallization (IRI), ice nucleation and ice shaping [6, 9]. These parameters allow to compare the IBPs to each other and to measure their effectiveness [9]. The following paragraph will describe the IBP activities and the methods used to measure them.

1.2.1 Thermal hysteresis (TH)

In pure water, the freezing point and the melting point are the same and are close to 0°C. The freezing point depression consists in the decrease of the solvent freezing point on addition of a non-volatile solute. This phenomenon is a colligative property of the solution and depend on the number of solute particles and not by their nature [10]. The differences between the melting point and the freezing point of the water is called thermal hysteresis (TH). IBPs are able to decrease the water freezing point and slightly increase the melting point [11, 12] (**Figure 1**). The TH activity of IBPs is mainly due to the lowering of freezing point. [12]. This activity is also a colligative, concentration-dependent property of antifreeze solutes, such as trehalose, ethylene glycol and ethanol. On the contrary, IBPs act on TH in a non-colligative manner [5, 13]. TH activity is usually measured with a nanoliter osmometer, where the size of microscopic, single ice crystal is monitored in response to finely tuned temperature changes [14]. Inside the TH gap, ice crystals neither grow nor melt, this state is called “supercooled state”. Below the freezing point, the growth of ice crystal is explosive, with different burst patterns depending on IBP features [7]. On the basis of TH activity, IBPs are classified as moderate, with TH of 0.1-2.0 °C, or as hyperactive, with TH of 2-13 °C [6, 15].

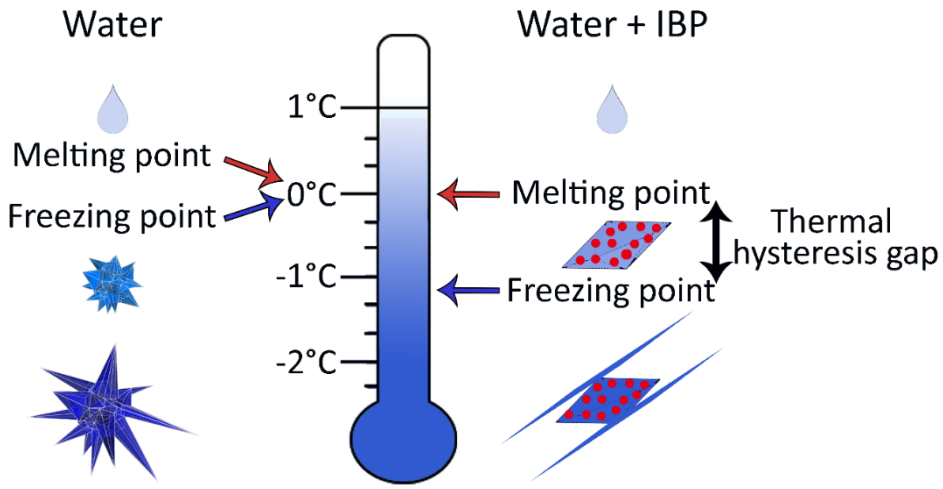

Figure 1. Thermal hysteresis. In the absence of IBPs (left), the melting point and the freezing point of water are nearly, and below this temperature (equilibrium freezing point) crystal growth occurs in all directions. IBPs (red dots, right side) can bind ice crystals and control their shape. These abilities reflect in the decrease of the freezing point and in the rise of the melting point. At temperatures below the freezing point, the direction of ice crystals growth depends on the ability of IBPs to bind the crystal surface and on the ice planes involved in binding. Figure adapted from [16].

1.2.2 Inhibition of ice re-crystallization (IRI)

Over time, at the frozen state, large ice crystals grow at the expense of smaller ones in a process called ice recrystallization [17-19] (**Figure 2A**). The underlying phenomenon is the Ostwald ripening, where solutions or colloidal suspensions of very small solid particles evolve over time towards an inhomogeneous structure, with redisposition of particulate matter onto larger crystals or solid particles [20]. Ice recrystallization can occur with different mechanisms, based on small temperature variations around the equilibrium freezing point. In the "migratory recrystallization" mechanism, at a given increase of temperature, the melting of small ice crystals occurs faster and causes the rise of liquid phase embedding large crystals still present. When the temperature decreases, the water molecules freeze again around large ice crystals, thus increasing their size [21]. On the other hand, in the mechanism of "accretive recrystallization" two neighbor ice crystals blend into a large ice crystal [22]. Large ice crystals are very harmful for the cells, indeed they induce the cell rupture, either

physically or through dehydration [4]. These damages are alleviated in freeze-tolerant organisms producing IBPs endowed with inhibition of ice recrystallization (IRI) activity (**Figure 2A**) [6].

Two methods have been described to measure IRI activity, the so-called "splat assay" and "IRRINA assay" [23, 24]. In both cases, a polycrystalline film is obtained starting from water solution at different IBP concentrations. Crystals are observed over the time, under an optical microscope, in order to measure their mean radius. In the splat assay, the polycrystalline ice film is obtained by dropping the IBP solution on a cold surface. During the assay, the temperature is tuned around the equilibrium freezing point [23]. In the IRRINA assay, the polycrystalline film of IBP solution is sandwiched between two microscope glass plates. During this time, the number and the size of ice crystals are monitored for 2 hours at -8°C [24, 25] (**Figure 2B i**).

Only in the case of IRRINA assay, the quantitative analysis of observed parameters has been described in detail. The cubic means radius of ice crystal is in linear regression with the time according with the follow equation:

$$r^3(t) = r_0^3 + kt$$

Where: r^3(t) is the time-dependent cubic mean radius, r_0^3 is the initial cubic mean radius at the start of the experiment and k is the ice recrystallization rate constant (**Figure 2B ii**). The effective rate constant (k_{l0}) depends on the concentration of IBP in accordance with a sigmoidal curve. In this context the inhibitory concentration (C_i) has been defined as the IBP concentration causing 50% reduction of k_{l0} (**Figure 2B iii**). Based on C_i values, IBPs are classified in three classes: very effective ($C_i < 10^{-1}$ μmol L^{-1}), effective ($10^{-1} < C_i < 10^3$ μmol L^{-1}), and noneffective ($C_i > 10^3$ μmol L^{-1}) [25].

Unfortunately, although the two IRI assays are in many respects similar, data obtained from them are not directly comparable due to differences in sample composition and assay conditions [9]. However, the overview of literature data allows some generalization, indicating that IRI occurs with sub-micromolar concentration of IBPs, while TH activity requires millimolar concentration of the same protein.

Although IBPs present both activities, significant correlation was not established to date between the two activities [26].

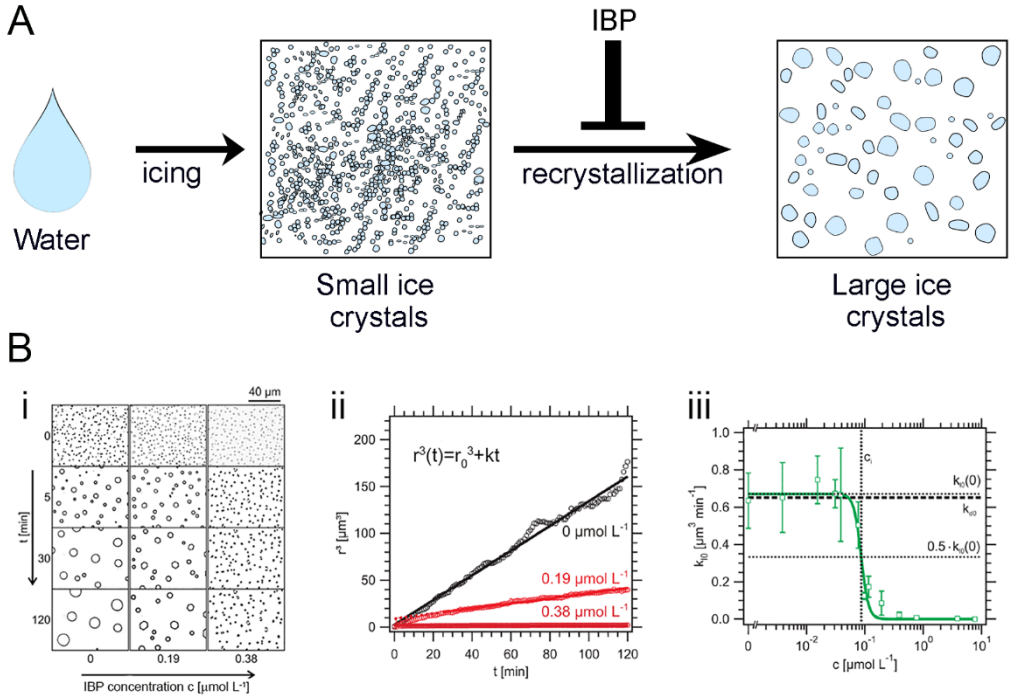

Figure 2. Inhibition of ice recrystallization. A) In the absence of IBPs, the icing process implies the growth of large ice crystals at the expense of smaller ones. The presence of IBPs stabilizes and favors the formation of small ice crystals. Figure adapted from [27]. B) IRRINA assay. i) Growth of ice crystals monitored for two hours in the presence of different concentrations of IBP; ii) the cubic means radius $r^3$of the ice crystals is represented as a function of time. The rate constant k depends on IBP concentration (iii), the inhibitory concentration of IBP (C_i) is defined as the concentration causing the halving of the initial constant rate, k_{I0}. Figure adapted from [25].

1.2.3 Ice shaping and ice planes affinity

In ice lattice, the oxygen atoms of water molecules are in tetrahedral coordination forming four hydrogen bonds with other water molecules. This disposition reflects in the formation of a parallelepiped with hexagonal base [28]. The main axes of ice lattice are *a*1, *a*2, *a*3 and *c*, while eight faces form the ice surface. Two of these faces are called basal planes and contain the three *a*-axes arranged in 120°-angles (**Figure 3A i**), whereas the *c* axis is perpendicular to basal planes. Primary prism planes are sides of the hexagon unit cell (**Figure 3A ii**), whereas the secondary prism planes are perpendicular to the *a*-axes (**Figure 3A iii**). Pyramidal planes cut the unit cell (**Figure 3A iv and v**).

IBPs are characterized by the ability to bind ice crystals on single or multiple planes [7]. As a consequence, the shape of ice crystal is modified (ice shaping). In pure water, ice forms flat disks whose basal planes are the only observable. By contrast, in the presence of IBPs, ice crystals assume peculiar and diverse morphologies depending on the affinity of the IBP for specific plane(s) [29]. Moderate IBPs typically induce the growth of bipyramidal ice crystals, whereas the hyperactive ones cause the formation of lemon-shaped ice crystals [6, 29]. Also, the explosive growth depends on crystal planes bound by IBPs, or, more precisely, on those remained unbound.

The observations of bound ice planes require the use of fluorescently labelled IBPs. The technique is known as “fluorescence based ice plane affinity” (FIPA) analysis [30, 31]. Typically, IBPs are labeled by conjugation with tetra-methylrhodamine, or by fusion with green fluorescent protein (GFP). The labelled IBP is slowly incorporated into a macroscopic single ice crystal hemisphere that is oriented to determine *a* and *c* growth axes. The ice planes bound by IBP are evaluated based on the pattern observed by imaging upon the probe excitation [32]. Figure 3B represents the ice-binding patterns observed by FIPA analysis and the corresponding bound ice planes. As previously anticipated, FIPA analysis allowed clarifying the difference in terms of ice-binding pattern between hyperactive and moderate IBPs, with hyperactive IBPs typically binding the basal plane and possibly additional

planes, and moderate IBPs binding prismatic and pyramidal planes, but not the basal one [6, 32].

Combination of fluorescence-labelled IBPs and of a microfluidic device allows to dynamically study the growth of single ice crystals and the interactions between IBPs and ice planes [33, 34]. The main advantages of the microfluidic system consist in the ability to control physical parameters such as temperature and flow rate. Different methods were described by the same research group [33-36]. The first microfluidic devices were isothermally-cooled (ISOCOMIDs), with temperature control obtained by a copper plate [34]. An improvement was obtained by including an infrared laser to melt ice in specific site, chip-valves to block the fluid flow and by additional temperature control units [33, 35]. At the present, the most advanced device is represented by the microfluidic cold finger (MCF), where a temperature gradient can be finely controlled [36].

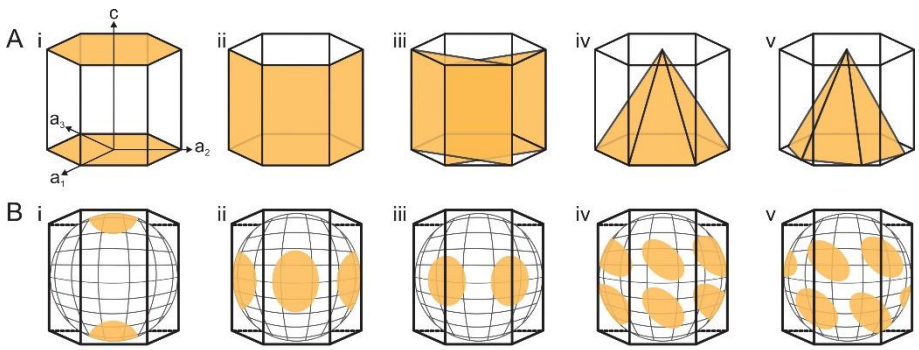

Figure 3. Ice crystal planes. A) Representation of planes and main axes of an ice crystal (*a*1, *a*2, *a*3 and *c*). B) Representation of FIPA analysis by microfluidic cold finger. A single ice crystal is mounted with a primary prism plane perpendicular to the cold finger. Panels represent (i) basal plane, (ii) primary prism plane, (iii) secondary prism plane, (iv) pyramidal plane aligned with the *a*-axes, and (v) pyramidal plane offset to the *a*-axes. Figure adapted from [32].

1.2.4 Ice nucleation activity

Ice crystallization takes place in two phases, the nucleation, *i.e.* the formation of a stable *core*, and the growth of the ice crystal starting from the *core*. Crystals growth can be inhibited by binding of IBPs with ice nuclei. By contrast, ice nucleation proteins (INPs) induce nucleation events of ice crystals at high sub-zero temperatures. These events lead to the formation of embryonic ice crystals and subsequent freezing. The INPs have been identified in bacteria, insects and plants and their main function seems related to trophic purposes [37-39]. For instance, the INP from the plant pathogenic bacterial *Pseudomonas syringae* is found on plant leaves where it induces the freezing of water, causing tissue injury and facilitating trophic activity [38, 40]. The INP from *P. syringae* is a megaDalton multimer whose structure is not yet available. Surprisingly, the 3D model consists in a β-solenoid similar to that of *Marinomonas primoriensis* IBP (*Mp*IBP) [41]. Both structures present large surfaces which may be necessary to align water molecules in ice-like ordered structures. This may favor the formation of ice nuclei in the case of INP [40, 41] and inhibit their growth in the case of IBP. The hypothesis that the two proteins share the mechanism of ice binding described in the next paragraph is supported by experiments on a truncated variant of the *P. syringae* INP, which acquired TH and ice shaping activities [42].

1.3 Mechanisms of ice binding

The inhibition of ice crystals growth has been explained since long through the adsorption-inhibition mechanism proposed by Raymod and DeVries [11]. According to this mechanism, the binding between IBPs and the ice surface is irreversible and induces a curvature of the ice surface (**Figure 4A**). This micro-curvature makes thermodynamically less favorable the addition to ice surface of new water molecules from bulk solution. This phenomenon drives the depression of the freezing point, which is strictly correlated with the curvature radius through the Gibbs-Thomson effect [30]. The main assumption of this model is the irreversibility of the binding between IBPs and ice. The irreversibility of binding has been demonstrated for the

hyperactive IBP from *Tenebrio molitor* fused with the GFP. After binding, the IBP presents in bulk solution was removed without causing any change in ice-associated fluorescence and in the growth of ice crystals. This indicates that once bound to ice, IBP is not able to exchange with IBP free molecules present in solution [33]. Moreover, this and other experimental works support the hypothesis that bulk IBP molecules are required to inhibit secondary nucleation events causing the deposition of new ice layers on planes not bound by IBPs [35, 43]. The adsorption–inhibition mechanism explains how IBPs depress the water freezing point, but does not explain the mechanism of interaction between IBPs and ice surface. The functional region of IBPs is called ice binding site (IBS) and it is described in detail in the paragraph 1.6. Briefly, IBS are flat, relatively wide and rich of threonine (Thr) residue repeats. The lateral chain of Thr contains one methyl group and one hydroxyl group. The chemical properties of Thr have suggested a first interaction model where interaction with ice is dominated by hydrogen bonds (**Figure 4A i**) [44]. Mutagenesis studies did not support this hypothesis. Indeed, the TH activity remained unchanged when the Thr residues of IBS were substituted with valine, which is devoid of hydroxyl groups and has two methyl groups. By contrast, the substitution of Thr with Ser residues, which has only a hydroxyl group, negatively affects the TH activity of the mutant [45]. Subsequently, the discovery of new IBPs with IBS rich of hydrophobic residues led to hypothesize a prominent role of hydrophobic effect (**Figure 4A ii**). According to this model, water molecules close to hydrophobic side chains of IBS negatively contribute to IBP solvation energy. The strong negative entropic contribute is alleviated when IBS are bound to ice, thermodynamically fostering the adsorption process [46].

To date the most widely accepted model is based on the "anchored clathrate" hypothesis, which was suggested by molecular dynamic simulations and experimentally validated by X-ray crystal structures [47, 48]. According to this model, the side chains of solvent exposed IBS residues induce water molecules to form an ice-like, *quasi*-liquid layer at the ice-water interface [7]. In *Mp*IBP, clathrates of water molecules were found around the Thr methyl groups of IBSs. Moreover,

clathrates are hydrogen bonded to IBS though hydroxyl groups of Thr and backbone amide groups (**Figure 4A iii**) [49].

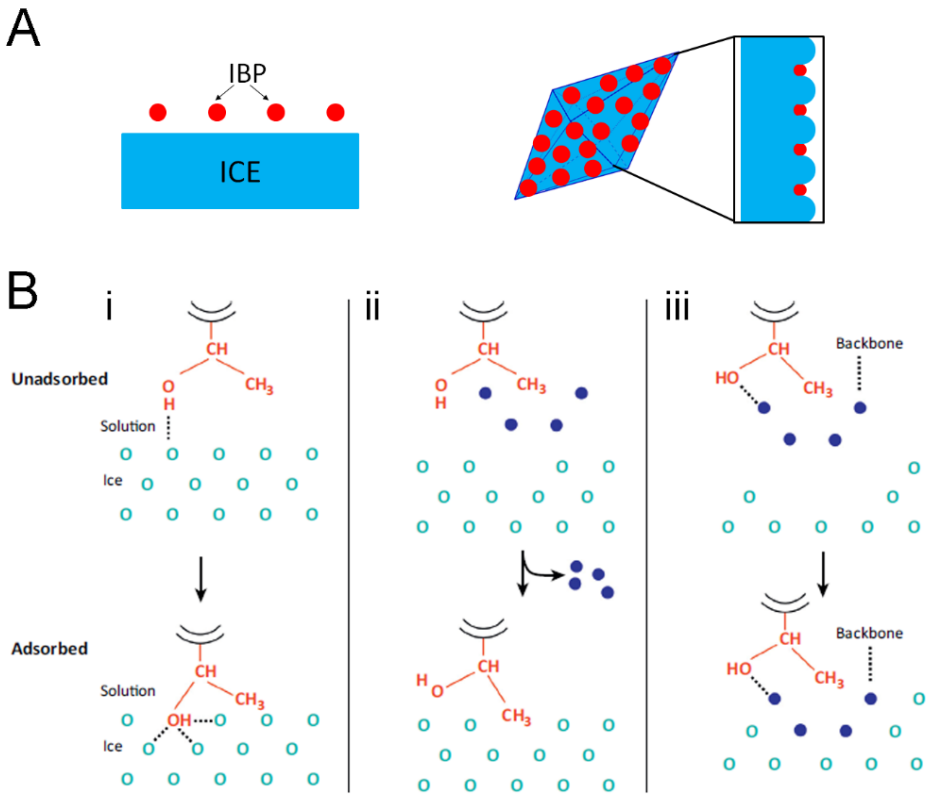

Figure 4. Models of IBP ice binding. A) Adsorption-inhibition mechanisms. When an IBP binds the ice surface induces a micro-curvature, which hampers the addition of new water molecules. B) Mechanisms proposed to explain the ice binding. The side chain of Thr residues is in orange, water molecules in the *quasi*-liquid layer are light blue spheres. i) Hydrogen bond model: in the unabsorbed state, the hydroxyl group of Thr is hydrogen bonded with ice; when Thr is inserted in the ice lattice, additional hydrogen bonds are formed. ii) Hydrophobic model: the methyl group of Thr is embedded in a clathrate (blue spheres), which is dissolved upon the adsorption of IBS to ice. iii) Anchored clathrate model: the clathrate is anchored by the hydroxyl group of Thr and constitutes the water quasi-liquid layers that become ice. Panel B is reproduced by [7].

1.4 Biological role of IBPs

The first IBP was discovered by Arthur DeVries in the blood of Antarctic notothenioid fishes in the late 1960s [8]. Since then numerous IBPs have been isolated from different organisms exposed to sub-zero temperature, including fishes, insects, plants, algae and bacteria [6, 7]. To date it is possible to attribute to IBPs five different physiological functions [9]. In organisms such as fishes and insects, the main function of IBPs is to avoid freezing. Hence, IBPs from these organisms present moderate or hyperactive thermal hysteresis (TH) activity (**Figure 5A**) [6]. The presence of these kinds of IBP is joined with the production of colligative solutes, such as polyols, which maintain biological fluids liquid at sub-zero temperatures, favouring *de facto* the surviving [50, 51]. In freeze-tolerant species, the main function of IBPs is to protect the organisms from the injuries derived from the formation of large ice crystals (**Figure 5B**) [18, 52]. Generally, the IBPs from these organisms present low TH activity and high IRI activity [53, 54].

In microorganisms such as algae, yeasts, fungi, diatoms and some bacteria isolated in several habitats from sea to glaciers, the IBPs are secreted in the body surroundings. The main function of these IBPs is to maintain liquid the environment, create "channels" in the ice mass and to facilitate trophic functions (**Figure 5C**) [55-58]. In the case of the already mentioned *Mp*IBP, the complex structural feature of this multi-domain protein, allows, among other functions, the interaction between the bacterium *M. primoriensis* and the diatom *Chaetoceros neogracile* [48, 59]. Thank to this symbiosis, the diatoms can adsorb to ice surface, which means exposed to the sun light required for the photosynthesis, while the bacterium can use the oxygen and the nutrient produced by diatom [60]. Finally, we can consider again in this context the INPs produced from some pathogens, which induce freezing of plants and fruits tissues, promoting their rot and increasing the availability of nutrients [50, 61].

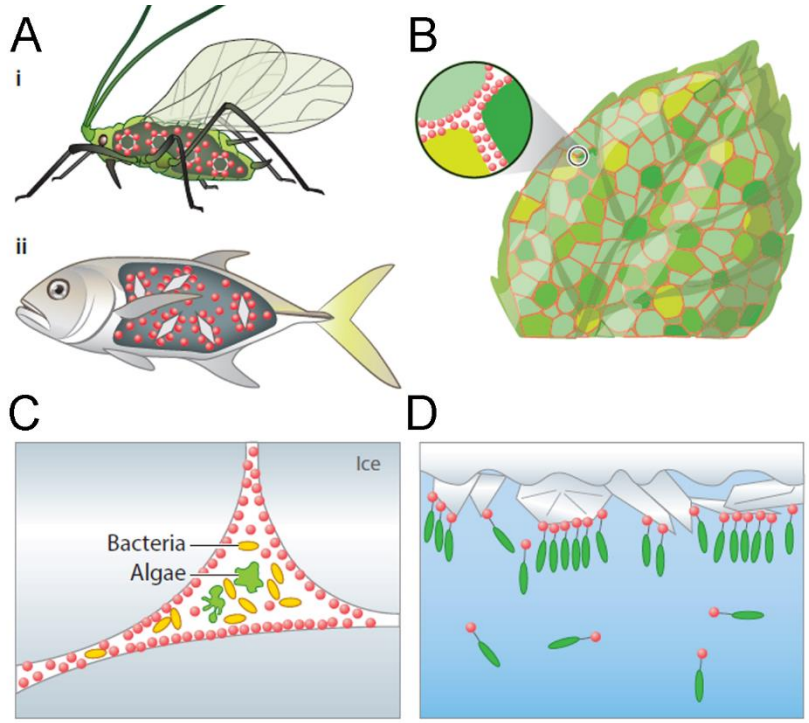

Figure 5. Biological roles of IBPs. A) In freeze-avoiding organisms, such as insects (i) and fishes (ii), the function of IBPs is to maintain liquid the biological fluids. Generally, in these organisms IBPs have moderate or hyperactive TH. B) In plants, IBPs have low TH and prominent IRI activities, which prevent the formation of large ice crystals. C) Secreted IBPs have the function to maintain liquid the cell environment, hence increasing the habitable space. IBPs from these organisms show from moderate to hyperactive TH activity. D) Hyperactive *Mp*IBP from *M. prymoriensis* promotes the adhesion between bacteria and ice surface. IBPs are represented as red spheres. Reproduced from [6].

1.5 Structural diversity of IBPs

Although sharing the same mechanism of ice binding, IBPs have diverse sequence and 3D structures. To date, 11 folds are associated to proteins able of to bind ice crystals (**Figure 6**) [6]. Usually, IBPs are classified based on their origin and their fold. There are five types of fish AFPs. The so-called type I AFP is characterized by large structures dominated by alanine-rich α-helices [62]. By contrast, type II and type III AFPs are small globular proteins [63, 64], whereas type IV is predicted to have a four-helix bundle fold [65, 66]. Finally, the antifreeze glycoproteins (AFGP) contain the repeats $(Ala\text{-}Ala\text{-}Thr)_n$ and the disaccharide galactose-N-acetylgalactosamine linked to the hydroxyl group of Thr [67, 68].

On the other hand, IBPs identified in plants, insects and microorganisms present a β-solenoid fold. The IBPs isolated from the insects *Tenebrio molitor* (*Tm*AFP) and *Rhagium inquisitor* (*Ri*AFP) share the β-solenoid fold, with internal disulfide bonds stabilizing the solenoid [49, 69]. By contrast, the AFP from the snow flea *Hypogastrura harveyi* presents an atypical fold consisting in a bundle of polyproline type II coil [70].

For the plant IBPs, only the 3D structure of *Lp*IBP from *Lollium perenne* is available and consists in a β-solenoid with ice binding sites less ordinate than those found in insect IBPs [54]. To date, two folds have been identified in IBPs from microorganisms: the huge, regular β-solenoid stabilized by calcium ions found in the lone structure of *Mp*IBP, and the IBP-1 fold, a discontinuous β-solenoid coupled with a α-helix alongside the main axis of the protein, found in IBPs containing the domain of unknow function (DUF) 3494 [71, 72].

The structural diversity of IBPs suggests that proteins arose several times and encountered convergent evolution reaching similar functions and structures [6, 7]. One cannot exclude lateral gene transfer as an important mechanism of spreading anti-icing activities. For instance, horizontal gene transfer may have occurred among cold-adapted fishes from different species, which produce very similar type II AFP [73].

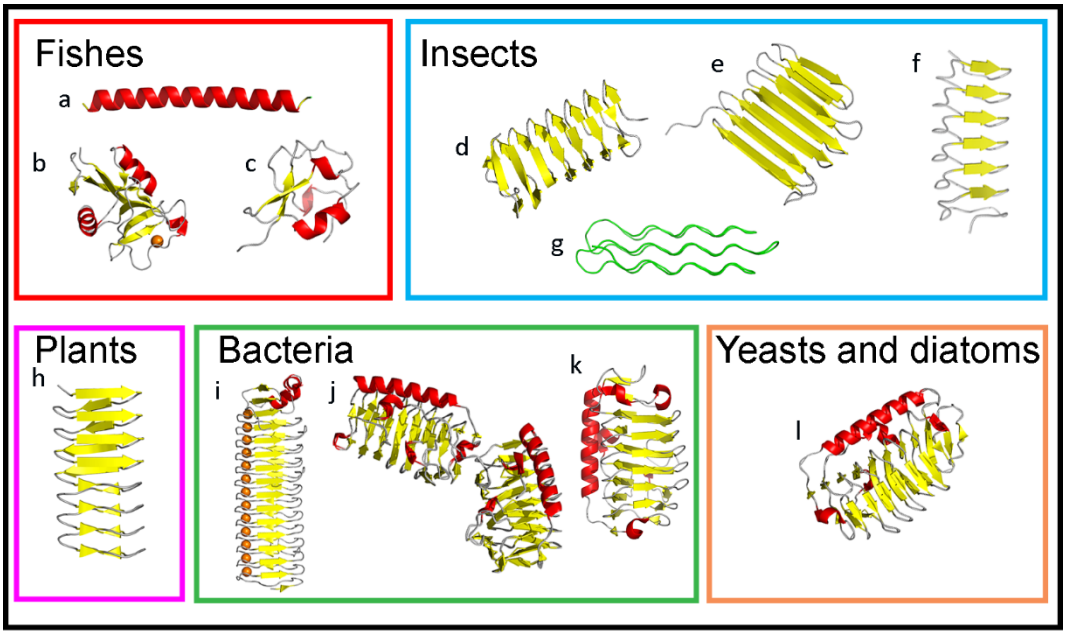

Figure 6. 3D structure of IBPs. IBPs are classified based on their origin. Fish IBPs are type I AFP (a, PDB: 1wfa); type II AFP (b, PDB: 2py2) and type III AFP (c, PDB: 1ame); Most insect IBPs share a β-solenoid fold and are represented by *Tenebrio molitor Tm*AFP (d, PDB: 1ezg), *Ragium inquisitor Ri*AFP (e, PDB: 4dt5) *spruce budworm sbw*AFP (f, PDB: 1m8n), while the snow flea (sf) AFP (g, PDB: 2pne) has a bundle of polyproline type II coil fold. *Lolium perenne Lp*IBP (h, PDB: 3ult) is the only representative of plant IBPs. The bacterial MpIBP has a β-solenoid fold (i, PDB: 3p4 g), while the IBP-1 fold was identified in bacteria (j, PDB: 5UYT, k, PDB: 3wp9), yeasts (l, PDB: 3vn3) and algae.

1.6 Ice binding sites: the functional region of IBPs

The functional part of an IBP is the ice binding site (IBS). Generally, the IBSs are relatively wide and flat regions, rich of threonine, largely devoid of charged residues, and often characterized by structural repeats [6, 7]. The identification of one IBS is challenging due to the high diversity in terms of primary and tertiary structure of IBPs. A first approach for the identification of putative IBS consists in the multiple alignment of amino acid sequence of target IBP with isoform and ortholog sequences. This analysis can be successfully combined with structural analysis of the 3D structure and ice docking simulation. After the identification of putative IBS, a site-directed mutagenesis experiment is undertaken to disrupt the regularity of the IBS and to intentionally interfere with IBS activity [7]. A classic example of mutagenesis is the substitution of Thr of the putative IBS with tyrosine (Tyr) residues, followed by the analysis of TH activities of the mutants. Mutants with decreased TH activity shall identify residues involved in ice binding and possibly belonging to the IBS. This approach has been used to identify the IBS of several IBPs, including *Mp*IBP and *Lp*IBP [54, 59].

Unfortunately, the high diversity of IBPs is reflected also in the IBS composition and this makes it difficult to decipher the structural features required for the ice binding [7]. For instance, the IBSs from insects are usually regular and formed by two rows of Thr belonging to tandem repeats [49, 74, 75]. However, the IBS of AFP from *Rhagium inquisitor* (*Ri*AFP), one of the most TH-active IBPs, is larger if compared to other insect IBSs and is made of four parallel rows of Thr residues. Molecular dynamic simulations suggest that the high activity of *Ri*AFP is due to a layer of water molecules covering the IBS surface, which allows the protein to bind multiple crystal planes [69]. Another example of uncommon IBS is offered by the IBP from Lake Ontario midge (*Chironomidae*). In this case, the IBS is formed by a row of seven outward Tyr residues embedded in the motif CxGxYCxGxx [76].

1.7 Biotechnological applications of IBPs

The applications of IBPs are several and widespread from organ to food storage. In the food industry, the IBPs are mainly used to inhibit the ice recrystallization, in fact the formation of large ice crystals during the storage affect the food texture decreasing its quality [77]. The IBPs are added in low-fat ice creams to maintain smoothness during long storage [78]. However, the effects of IBPs on ice cream are controversial and most probably are strictly correlated with the ice-cream formulation [79]. Similar applications of IBPs are developed also with other frozen foods, such as meat and dough, to increase storage life [77].

During the storage of mammal cell lines, cells suffer of severe freezing damages leading to cell lysis, necrosis or apoptosis [19, 80]. Underlying phenomena include the formation of intracellular large ice crystals [81] and dehydration [82]. The most common cryoprotective agents (CPAs) used in cells storage are glycerol and dimethyl sulfoxide (DMSO), which have toxic effects and must be removed during the thawing [83, 84]. Generally, the IBPs are added to the freezing medium in combination with chemical CPAs, thus lowering the required amount and its cytotoxicity [19]. The concentration of the IBPs used in this kind of application ranges from 0.1 mg/mL to 1 mg/mL (micromolar concentration), depending on the chosen protein and experimental conditions [80]. Promising results were obtained in the cryopreservation of several human cell lines, including hepatocytes, oocytes and spermatozoa [80, 81, 85, 86]. By contrast, when the IBPs are used to preserve red blood cells [87] and cardiomyocytes [88, 89] they induce cellular damage during the cryopreservation.

The major challenges of industrial IBP application are related to the stability of these proteins and to their availability. For these reasons, future research with the aim to increase the stability and the recombinant production of IBPs will be necessary.

1.8 DUF3494-containing proteins: a new class of IBPs

Recently, the research on bacterial and algae communities brought to the discovery of IBPs containing a domain of unknown function (DUF) 3494, whose fold consists in a discontinuous β-solenoid. Proteins with the DUF3494 were found in psychrophilic organisms, prevalently bacteria, belonging to the phylum of *Flavobacterium* and *Bacteroidetes*, and Archaea [90]. Among DUF3494-containig proteins, some are able to bind ice crystals and were classified as IBPs [72, 91-99].

DUF3494 IBPs were identified in several species including diatoms, algae, fungi, copepods, bacteria and yeasts from different environments (i.e. seas, lakes, glaciers, ice and snow-covered fields) spread from Artic to Antarctica [100]. On the basis of this observation, it is very difficult to delineate the evolutionary path of DUF3494 IBPs. However, in the phylogenetic tree DUF3494 IBPs from different organisms cluster together. For this reason, is possible to speculate that the distribution of DUF3494 IBPs occurred through horizontal gene transfer (HGT) [101-103]. One of the best example of HGT is occurred between eukaryotes, where the diatom *C. neogracile* transferring its DUF3494 IBP to the copepod *Stephoslongipes* [101, 104].

Remarkably, all DUF3494 IBPs share an N-terminal export signal peptide suggesting that these proteins are secreted or anchored to the membrane. The secretion of DUF3494 IBPs might be related to the ecology of "brine pockets" i.e. small cavities or fissures included in ice block and containing high salinity seawater. The secretion of IBPs may contribute to keep liquid the microenvironment of brine pockets, thus representing a valuable adaptive advantage [56, 102, 105] (**Figure 7A**).

A second function of secreted IBPs is offered by the symbiosis of the bryophyte *Bryum argenteum* with IBP-producing bacteria living on its surface. The secretion of IBPs prevents the recrystallization of ice crystals on the moss surface favouring the freezing tolerance, on the other hand, bacteria receive nutrients derived from photosynthesis [58] (**Figure 7B**).

In the case of *Sf*IBP_1 from *Shewanella frigidimarina*, the multi-domain architecture, together with the localization on cell membrane suggest that this protein

represent a new example of ice adhesin. The function of this protein is unknown, but it is possible to speculate that the function of *Sf*IBP_1 is similar to that of *Mp*IBP, suggesting that ice adhesion may be a strategy for surviving cold aquatic environments (**Figure 7C**).

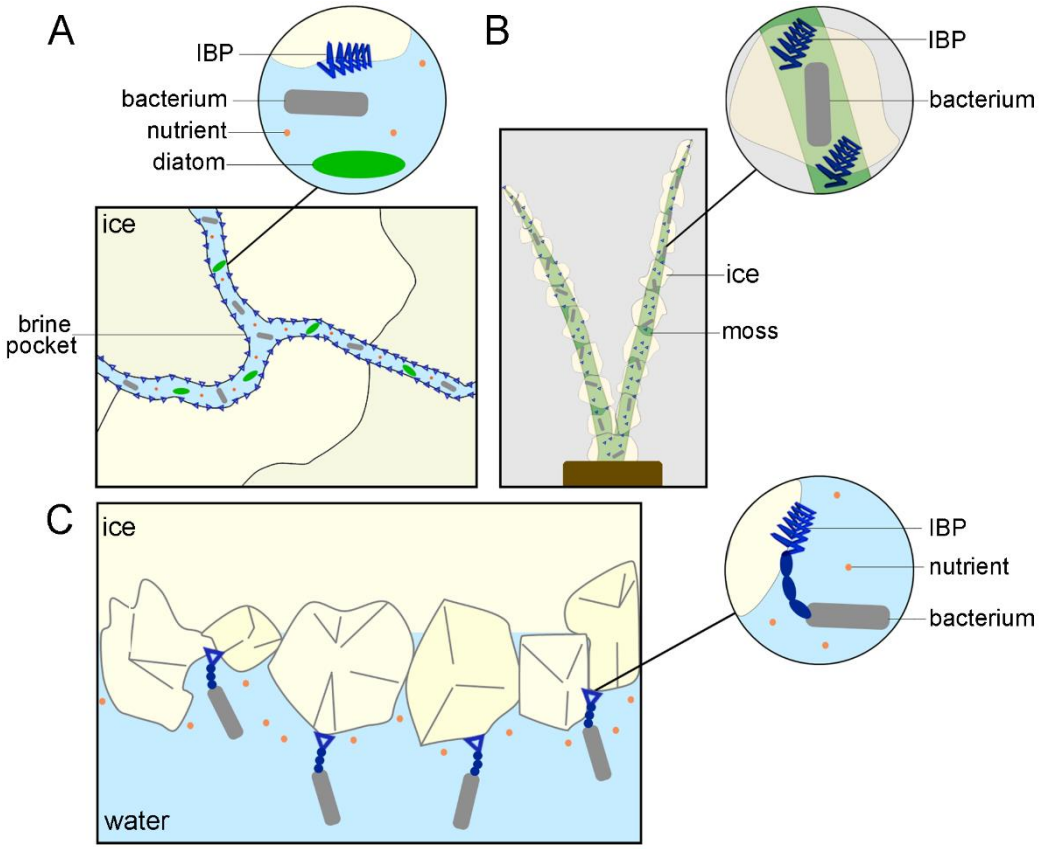

Figure 7. Biological functions of DUF3494 IBPs. A) Secreted DUF3494 IBPs stabilize the brine pockets maintaining liquid the environment near the cells. B) Symbiosis between the aquatic moss, *Byrum argenteum* and epiphytic bacteria living on its surface. DUF3494 IBPs are secreted from bacteria and accumulate on the moss surface protecting it from freezing damage. C) *Sf*IBP_1 from *Shewanella frigidimarina* is anchored to the cell membrane and favourite the adhesion between the bacteria and the ice surfaces. Figure from [27].

1.8.1 Architecture of DUF3494 IBPs

To date, 865 proteins present in PFAM library are predicted to contain a DUF3494 belonging to 84 different architectures. Although this overall wide heterogeneity, only three architectures have been found to date in DUF3494 IBPs. However, the paucity of characterized DUF3494 IBPs does not allow to exclude that other architectures could be associated to ice binding. Among the characterized DUF3494 IBPs, most have single-DUF3494 architecture [71, 72, 95, 96, 106, 107](**Figure 8A**). In *Sf*IBP_1, a single DUF3494 domain is preceded by an N-terminal series of tandem Bacterial Immunoglobulin-like domain (**Figure 8B**) [94]. Recently, IBPv from the *Flavobacteriaceae* strain 3519–10 has been described to contain two consecutive DUF3494 connected by a linker of 17 residues and ending with a short C-terminus domain (**Figure 8C**) [97, 108].

Common to all types of architecture is an N-terminal signal peptide, supporting the hypothesis that these proteins are secreted in the environment or associated to the cell membrane. The hypothesis of membrane association is made realistic also by the identification in *Sf*IBP_1 of a lipoprotein box, a sequence that might mediate its association to the cell membrane [94].

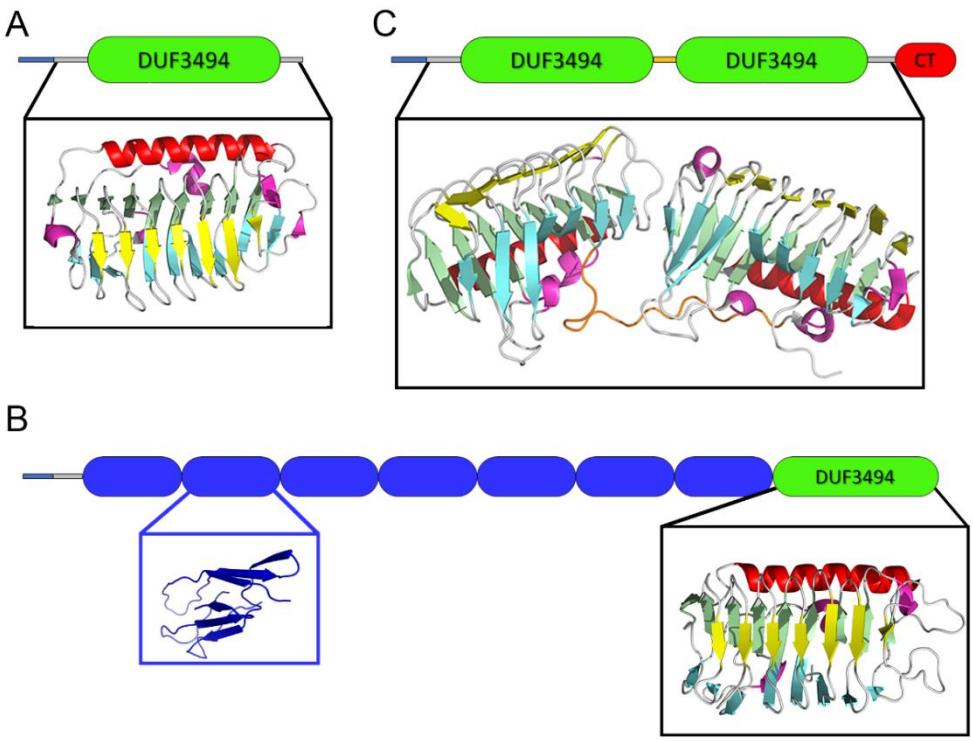

Figure 8. Architectures and 3D structures of DUF3494 IBPs. A) Single DUF3494 domain architecture. Boxed the 3D structure of *Tis*AFP6 (PDB code: 3VN3). B) Architecture of multi domain DUF3494 IBP: the bacterial immunoglobulin (BIg) domains are coloured in blue (Blue box contains the Phyre2 model of BIg2), whereas black box contains the 3D structure of *Sf*IBP_1 (PDB code: 6BG8). C) Architecture of double-domain DUF3494 IBP: two DUF3494 elements are connect by a linker (in orange), the C-terminal domain is in red; the 3D structure of IBPv (PDB code: 5UYT) is boxed. In all architecture representations, the N-terminus signal peptide is coloured in light blue. In all 3D structures, β strands belonging to the A, B, and C faces of β-solenoid are in green, yellow, and cyan, respectively. The helix α1 is in red and the 3_{10} helices in magenta.

1.8.2 Activity of DUF3494 IBPs

On the basis of TH activity, it is very difficult to classify the DUF3494 IBPs as moderate or hyperactive. Indeed, for these proteins, TH activity value ranges from 0.08 °C (at 200 μM of Afp4 from *Glaciozyma antarctica*) [98] to 3.8 °C (at 140 μM of *Col*AFP) [96]. An example of the heterogeneity of TH activity is given by the isoforms 6 and 8 of AFP from the snow fungus *T. ishikariensis* (*Tis*AFP). Despite the high sequence identity (83.4%), TH activity is 2.0 °C for *Tis*AFP8 at 0.11 mM, and 0.3 °C for *Tis*AFP6 at the same protein concentration.

Interestingly, the DUF3494 IBPs seem to share the ability to bind the basal planes of ice crystals, a feature that was deemed responsible of TH hyperactivity of IBPs [15]. Noteworthy, the binding of basal planes was observed for the hyperactive (*i.e*. *Tis*AFP8, *Col*AFP and *Sf*IBP_1) as well as for moderate DUF3494 IBPs (*i.e. Le*IBP, *Tis*AFP6 and *Fc*IBP11 from *Fragilariopsis cylindrus*) [71, 72, 94-96, 109] . It can be observed that hyperactive DUF3494 IBPs have affinity for multiple crystal planes, including the basal one. On the other hand, moderate IBPs may bind exclusively basal planes, but with low affinity [54, 72, 109]. The binding affinity might be related to β-solenoid fold and to the spacing of residues making up the IBS [54].

1.8.4 Structural features of DUF3494 IBPs

The 3D structure of DUF3494 IBPs consists of a discontinuous right-handed β-solenoid formed by three parallel β-sheets (faces A, B and C), with a triangular cross-section and an α helix alongside the main axis of the protein (**Figure 9**). This fold is called IBP-1 and is peculiar of IBPs belonging to this family. Two faces of the β-solenoid (faces B and C) are completely solvent-exposed and may be involved in ice binding, while the A face is hidden by the α helix.

To date all the DUF3494 IBPs of known 3D structure (*i.e. Le*IBP from *Leucosporidium* sp. AY30, *Col*AFP, *Ff*IBP, *Sf*IBP_1, *Tis*AFP6, *Tis*AFP8 and *Fc*IBP11) contain a “cap” head region at the top of the β-solenoid. This region is made by an unstructured loop connecting between two β-strand (**Figure 9**) [71, 72, 94-96, 106, 107]. Interestingly, in *Col*AFP and *Ff*IBP the capping region is stabilized by an

intramolecular disulphide bridge [96, 106]. A peculiar capping region was identified in *Sf*IBP_1, where two hairpin loops are stabilized through interactions between them, the 3_{10} helix and the solenoid β-strand [94]. The role of this region is still unknown, most probably involved in protein stabilization. This hypothesis is supported by mutagenesis experiments where the capping region of *Le*IBP (T_m 61 °C) and of *Ff*IBP (T_m 56.4 °C) were exchanged. Indeed, the "grafting" of *Ff*IBP capping region to *Le*IBP caused an increase of T_m (~ 5 °C), while the reciprocal exchange ("body" of *Ff*IBP, with capping region of *Le*IBP) gave a lower T_m (~ 10 °C) [106]. Another possible function of the cap region could be related to the high propensity of β-solenoid structures to form amyloid fibrils. The cap region could prevent the formation of supramolecular aggregates [110].

Although DUF3494 IBPs share the same fold, the composition of their IBS is very heterogeneous, thus causing their high functional heterogeneity. Structural analysis and docking simulations combined to site-directed mutagenesis experiments allowed to localize the IBS on the B face of the solenoid [71, 72, 95, 96, 106]. In contrast with the general rule indicating in repetitive motifs of Thr the signature of an hyperactive IBS, among hyperactive DUF3494 IBPs only *Ff*IBP shows the motif T-A/G-X-T/N [106]. On the other hand, hyperactivity might be due to the conformational flatness of the B face (e.g. *Col*AFP) [96], or to the marked hydrophobicity of IBS and of loop region (e.g. *Tis*AFP8) [72, 95].

The case of the hyperactive IBPv is noteworthy. The architecture of this protein is unique and consists in two IBP-1 homologous domains stabilized by hydrophobic interactions and intra-domain disulphide bonds [108]. IBPv has a TH activity >2°C, at concentrations higher than 50 μM, while single domains A and B exhibit much lower TH activity (0.40 °C and 1.37 °C, respectively, at similar concentration) [97]. Hence, the hyperactivity of IBPv seems related to DUF3494 duplication and not to the specific composition of its IBS. Indeed, the duplication of the DUF3494 increases the surface and size of IBPv, both these features are known to rise the TH activity in other IBPs [111-113].

In conclusion, the low number of to-date available 3D structures and the heterogeneity of IBS make difficult to understand the molecular mechanism and rationalize the structural determinants of DUF3494 IBPs (hyper)activity. In order to decipher the mechanism of ice binding in this class of proteins, further structural and functional studies are necessary.

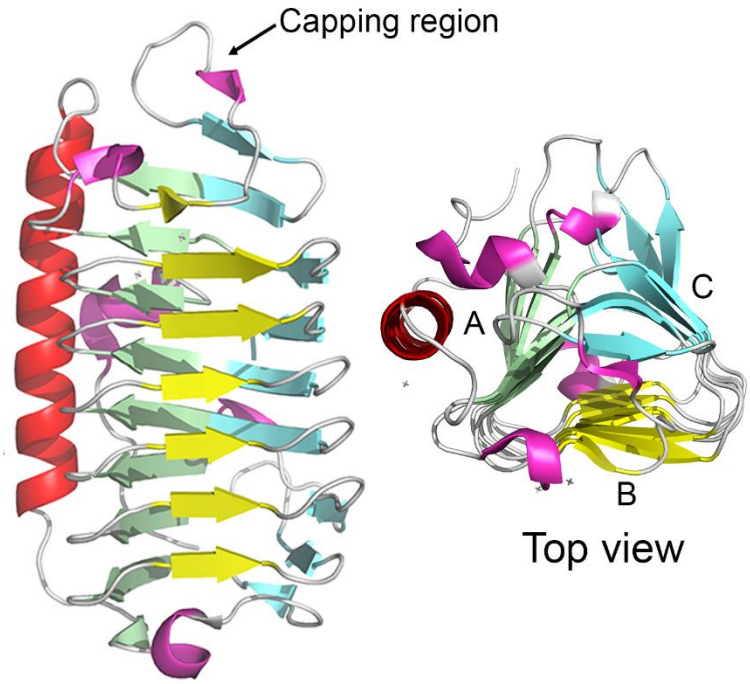

Figure 9. 3D structure of *Tis*IBP6. 3D structure of *Tis*IBP6 (PDB code: 3VN3) has been used as example of the structure of DUF3494 IBPs. The colour code of structural elements is the same of **Figure 8.**

1.9 *Euplotes focardii* and its bacterial consortium

Euplotes focardii is a free-swimming protozoan endemic of the oligothrophic coastal sediments of Terra Nova Bay, in Antarctica [114]. Its optimal growth temperature is around 4-5 °C, and its viability decreases upon exposition to temperatures above 10 °C [115]. Collections of *E. focardii* coming from expeditions in Antarctica were maintained as laboratory strains during the last 20 years and are valuable resource for the study of cold-adaption. *E. focardii* lives associated with a bacterial consortium, which is a common trait for ciliates inhabiting extreme environments [116]. In general, the role of these bacterial consortia is not yet completely understood, although in some cases the identification of mutualistic benefits received from both ciliates and bacteria has supported the hypothesis of a symbiotic relationship. Genomic analysis of *E. focardii*-associated bacteria gave indication on the prevalence of *Bacteroidetes* or *Proteobacteria*, including gamma and alpha *Proteobacteria* [117]. More in detail, among the bacterial genomes associated to *E. focardii*, the sequences of two putative IBPs, *EF*symbAFP (GenBank code AHG59376) and *EF*symbIBP (GenBank code A0A023J6X7), were identified. *EF*symbAFP has a single DUF3494 domain, while *EF*symbIBP has a double-domain architecture and share 53.4% of sequence identity with IBPv [117].

Reported in this thesis is the characterization in the depth of *EF*symbAFP, indicated from now on as *Efc*IBP. This study has disclosed new combinations of TH, IRI never described to date. Moreover, the comparison of functional and structural properties of *Efc*IBP contributed to the identification of structural features relevant for its activity and physiological role.

2. Main results and discussion

Although sharing the same 3D structure, ice-binding proteins containing the DUF3494 domain coming from different sources show surprising functional diversity [6, 7]. It is also likely that the exploration of biodiversity could allow the identification of new IBPs belonging to the DUF3493 family with new combinations of TH, IRI and ice shaping activities never described to date.

In Mangiagalli *et al.* (2017) [93] it has been demonstrated that *Efc*IBP is a single domain IBP belonging to the DUF3494 family. This protein was identified in the metagenome of the bacterial consortium living associated with the marine Antarctic ciliate *E. focardii*. *Efc*IBP presents a very effective IRI activity (*Ci*: 2.5 nM), which makes it one of the more powerful IBPs described to date. Although literature data on IRI activity were obtained from diverse techniques applied to a few DUF3494 IBPs only, they agree in witnessing that these proteins are from effective to highly effective in inhibiting the recrystallization, which may be their most physiologically relevant feature [56, 58, 91, 93, 94, 109]. We still do not know if a relationship between TH and IRI exists [26]. However, observations on the combination of these two activities among DUF3494 IBPs may be useful to give insight in the mechanism of ice binding and its physiological role. For instance, *Efc*IBP and *Sf*IBP_1, which are very effective in IRI activity (2.5 nM and 5 nM for *Efc*IBP and *Sf*IBP_1, respectively), show very different TH activities, with *Efc*IBP being a moderate IBP (0.53 °C at 50 µM), and *Sf*IBP_1 hyperactive (2°C at 80 µM) [93, 94]. The different behaviour of the two proteins could be related to the different physiological role or evolutive pressure exerted by different environments on organisms producing very similar proteins.

The molecular bases of the atypical combination of TH and IRI in *Efc*IBP were described in Mangiagalli *et al.* (2018) [118]. The X-ray crystallographic structure of *Efc*IBP consists of a right-handed β-helix with a triangular cross-section formed by three faces made by parallel β-sheets, and an α-helix, aligned along the axis of the β-helix (**Figure 2.1**).

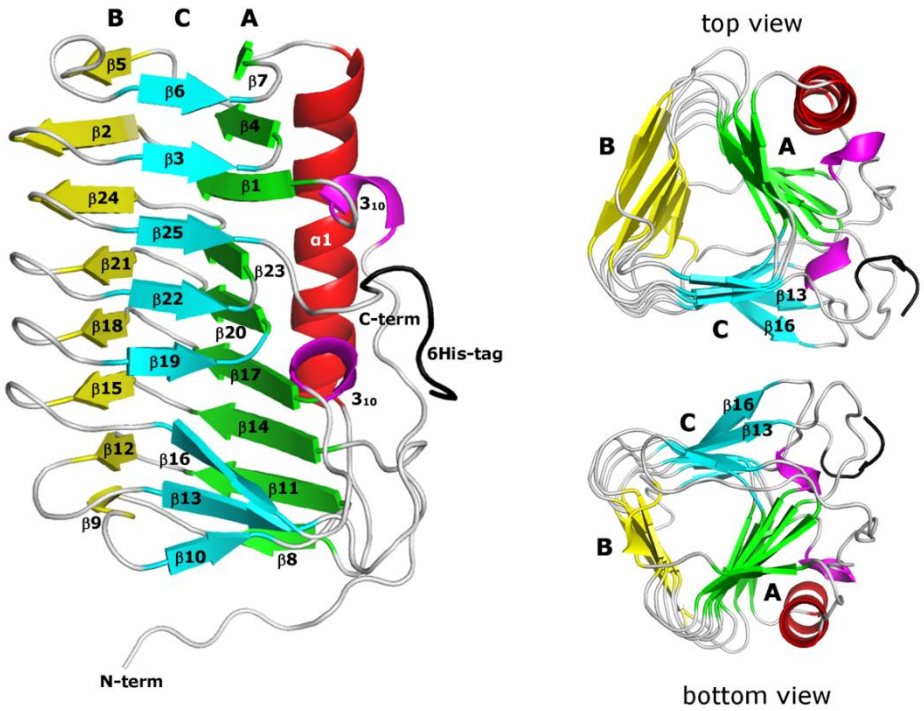

Figure 2.1. Three-dimensional structure of *Efc*IBP. Ribbon diagram showing the secondary structure elements of *Efc*IBP: β strands belonging to the A, B, and C faces of the β-helix are in green, yellow, and cyan, respectively. The helix α1 is in red and the 3_{10} helices in magenta. The triangular section of the *Efc*IBP structure is evident in the top and the bottom views. The β13 e β16 strands, which diverge towards the outside from the core of the β-helix, are indicated.

A peculiarity of *Efc*IBP not present in other DUF3494 IBPs is the absence of a "cap", a disordered region located at the top of the solenoid (**Figure 9**).

Some authors proposed that this region plays a key role in structural stabilization, however the fold of *Efc*IBP is stable to heat and to freeze-and-thaw process, suggesting that the primary function of the capping region is not related to stabilization of protein itself. On the other hand, it has been proposed that the capping might avoid fibrillar aggregation [110, 119, 120]. The low propensity of *Efc*IBP to form supramolecular aggregates (**data not show**) may be due to the presence of other cryptic signals, internal to β-solenoid structure and able to stop its end-to-tail assembly [110].

It is possible to distinguish three different faces of the β-solenoid: A, B and C. The B and C faces are both fully exposed to the solvent. The B face is flat and regular, while

the C face presents some irregularities. Overall, both faces are potentially involved in ice binding. Docking simulations indicate that the B face can bind the basal and the primary prismatic plane of ice crystals, whereas the C face has weak complementarity to the primary prismatic plane. Surprisingly, the addition of water molecules which co-crystallize with the protein favours the complementary between all the faces with the ice pyramidal plane. Based on structural analysis and docking studies, we have identified and mutagenized some residues possibly important in ice binding. More in detail, three residues on the B face (T67, T178 and T223) and three residues on the face C (S188, T209 and T247) were substituted with tyrosine, which is expected to disrupt the regularity of the IBS. Experiments of TH and IRI activity on the *Efc*IBP variants show that both faces are important in ice binding. This feature is a peculiarity of DUF3494 IBPs, not yet found in any homologous protein [72, 95, 96, 106], thus suggesting that *Efc*IBP presents an unusual mechanism of ice binding and recognition. However, structural analysis and site-directed mutagenesis do not provide a deeper insight in the molecular mechanism and dynamics of ice binding.

Despite the growing number of available crystallographic data, understanding the mechanisms of ice recognition and binding is very challenging. Several experiments of molecular dynamic simulation suggested that the formation of an ice-like layer of water on the IBS favors ice recognition. In this complex *scenario*, also the reason of hyperactivity remains unclear. Some authors proposed that the hyperactivity is due to the ability of IBPs to bind the basal plane of ice crystals and to the ability of their IBS to pre-order the interfacial water molecules [7]. However, atomistic simulation indicated that the preordering of water on the IBS surface is not a prerequisite for ice recognition by hyperactive IBPs [121]. Moreover, also moderate IBPs (i.e. *Fc*IBP11 and *Lp*IBP) are able to bind the basal plane of ice crystals [54, 72, 109]. Studies of Kaleda et al. (2018) [122] on chimeric GFP-*Efc*IBP are useful to shed light on this question. A unique pattern of ice growth and burst emerges for *Efc*IBP. In details, in the presence of this protein, ice crystals assume a hexagonal shape within the TH gap and encounter a “Saturn-shape” during the burst (**Figure 2.2.**). This

peculiarity might be ascribed to the ability of *Efc*IBP to bind the basal and the pyramidal near-basal planes of ice crystal as observed by FIPA analysis.

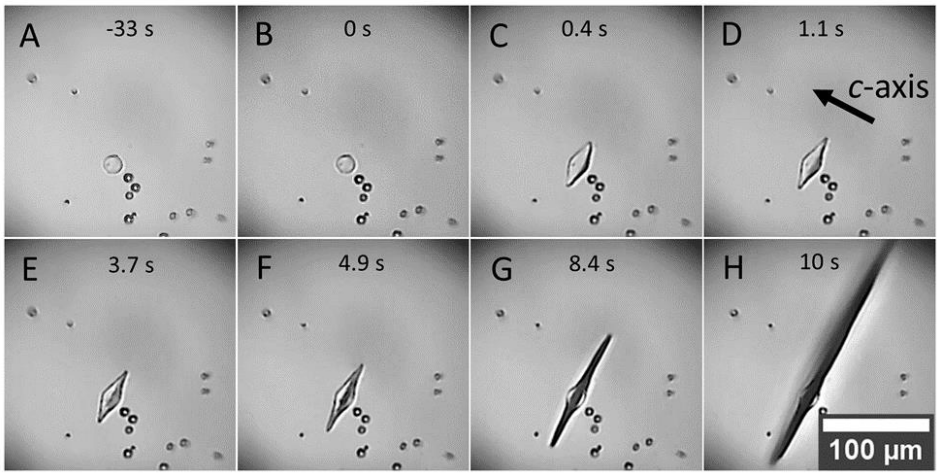

Figure 2.2. Pattern of ice growth and burst in the presence of *Efc*IBP. Selected video frames of ice crystal growth (A-F) and burst pattern (G-H) in wt *Efc*IBP 5 µM solution during cooling. Time from the beginning of growth is shown. The burst starts at 7.5 s.

Another issue to be raised is the correlation between TH hyperactivity and 3D structure. Indeed, the β-solenoid fold is typical of hyperactive IBPs, suggesting that the regularity of its residue spacing might increase the basal plane affinity [49, 74, 123]. On the other hand, all IBPs belonging to the family of "moderate basal binders" share the β-solenoid 3D structure [71, 72, 109]. This means that belonging to the β-solenoid fold is not a sufficient requirement to develop hyperactivity. The kinetics of binding to ice crystals add another piece to our puzzle. Such analyses carried out on *Efc*IBP indicate a binding rate comparable to that measured in the moderate AFP type III [35]. Interestingly, these values are ten time faster to that observed for the hyperactive sbwAFP from spruce budworm. Overall, these data indicate that basal plane affinity is not sufficient to induce hyperactivity, whereas the fast binding of *Efc*IBP to the basal plane may be related to its moderate TH and high IRI activities. For these reasons, the DUF3494 IBPs, which present unusual combination of TH and IRI activities, seems to be a good model to study the mechanisms of basal plane affinity and hyperactivity.

In conclusion, through the in-depth structural characterization of *Efc*IBP and the studies on its IRI activity, this thesis offers a set of unprecedented data and new perspectives in understanding the structure-function relationship of DUF3494 IBPs, which are widespread among diverse microorganisms. Moreover, *Efc*IBP is a good candidate for potential applications in the field of cryobiology and food preservation.

3. Results

Cryo-protective effect of an ice-binding protein derived from Antarctic bacteria

Marco Mangiagalli[1], Maya Bar-Dolev [2], Pietro Tedesco[3], Antonino Natalello[1], Aleksei Kaleda[2,4], Stefania Brocca[1], Donatella de Pascale[3], Sandra Pucciarelli[5], Cristina Miceli[5], Ido Braslavsky[2], Marina Lotti[1*]

[1]Department of Biotechnology and Biosciences, State University of Milano-Bicocca, Milano, Italy; [2]Institute of Biochemistry, Food Science and Nutrition, Faculty of Agriculture, Food and Environment, The Hebrew University of Jerusalem, Rehovot, Israel; [3]Institute of Protein Biochemistry, National Research Council, Naples, Italy [4]Department of Food Processing, Faculty of Chemical and Materials Technology, Tallinn University of Technology, Tallinn 12086, Estonia; [5]School of Biosciences and Veterinary Medicine, University of Camerino, Camerino (MC), Italy

* corresponding author

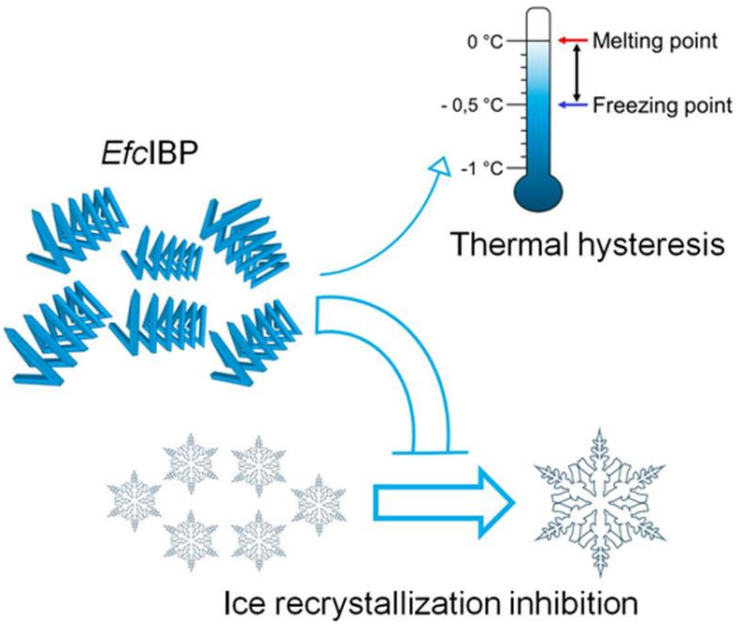

Keywords: ice recrystallization inhibition, ice binding protein, cold adaptation, thermal hysteresis, *Euplotes focardii* consortium

The FEBS Journal 284 (2017) 163–177. 2016 Federation of European Biochemical Societies
doi:10.1111/febs.13965

ABSTRACT: Cold environments are populated by organisms able to contrast deleterious effects of low temperature by diverse adaptive strategies, including the production of ice binding proteins (IBPs) that inhibit the growth of ice crystals inside and outside cells. We describe the properties of such a protein (*Efc*IBP) identified in the metagenome of an Antarctic biological consortium composed by the ciliate *Euplotes focardii* and psychrophilic non-cultured bacteria. Recombinant *Efc*IBP can resist freezing without any conformational damage and is moderately heat stable, with a midpoint temperature of 66.4°C. Tested for its effects on ice, *Efc*IBP shows an unusual combination of properties not reported in other bacterial IBPs. First, it is one of the best performing IBPs described to date in the inhibition of ice recrystallization, with effective concentrations in the nanomolar range. Moreover, *Efc*IBP has thermal hysteresis activity (0.53°C at 50 μM) and it can stop a crystal from growth when held at a constant temperature within the thermal hysteresis gap. *Efc*IBP protects purified proteins and bacterial cells from freezing damage where exposed to challenging temperatures. *Efc*IBP also possesses a potential N-terminal signal sequence for protein transport and a DUF3494 domain that is common to secreted IBPs. These features lead us to hypothesize that the protein is either anchored at the outer cell surface or concentrated around cells to provide survival advantage to the whole cell consortium.

Abbreviations

AFP: antifreeze protein; **CFU**: colony forming units; **DUF**: domain of unknown function; ***Efc*IBP**: *Euplotes focardii* bacterial consortium ice binding protein; **FT**: freeze and thaw; **GFP**: green fluorescence protein; **IBP:** ice binding protein; **IBS**: ice binding site, **IR**: ice recrystallization; **IRI**: ice recrystallization inhibition; **LB**: Luria-Bertani medium; **PB**: phosphate buffer; **TB**: terrific broth; **TH**: thermal hysteresis

Introduction

Earth is a cold place where the temperature of over 85% of soil and water environments is close to the freezing point of water. Under these conditions, challenges for Life are multifaceted, as temperature affects several key biological processes. In the cold, the fluidity of cell membranes decreases and protein folding is impaired because hydrophobic interactions weaken. Moreover, the rates of transcription, translation, cell division, and chemical reactions slow down. Nevertheless, a rich variety of organisms widespread across the Nature kingdoms thrives in cold habitats [1]. To cope with the constrains mentioned above, the so-called *cold-adapted* or *psychrophilic* organisms have evolved different adaptive strategies, for example changes in the composition of cell membranes towards higher content of unsaturated lipids, and the synthesis of cold-shock proteins and cold-active enzymes [2]. In the extreme condition of permanent sub-zero temperature, as it occurs in permafrost soils and ice seas, or seasonal temperature dropping, another risk threatens even cold-adapted organisms: freezing. The formation of ice crystals both inside and outside cells is a cause of cell damage and death [124]. Fishes, insects, plants, algae, diatoms, yeasts and bacteria that colonize very cold habitats, as for example Arctic and Antarctic regions, avoid ice injuries by producing ice binding proteins (IBPs) which inhibit the growth of ice crystals [6]. Though all IBPs bind the same ligand - ice - their molecular and functional diversity is astonishing, what surmises recent evolution [6] and makes it difficult to draft a picture of structure function relationships in this group of

proteins. The identification and detailed characterization of novel proteins is expected to add pieces of information useful to rationalize IBP's properties and functions. To this end, this work investigates an IBP from a peculiar biological source, the bacterial community (consortium) that lives in association with a cold-adapted ciliate isolated from cold seawaters at Terranova Bay.

IBPs decrease the water freezing temperature in a non-colligative manner, thereby creating a hysteresis between the melting and the freezing temperature (thermal hysteresis, TH) [11, 125]. TH derives from IBPs binding to water molecules at the outer layer of ice and inhibiting further ice growth at the position of binding. This local pinning of the surface induces a micro curvature of the rest of the ice surface in between the pinned positions and makes the association of other water molecules unfavourable from a thermodynamic point of view and *de facto* decreases the water freezing point. IBPs are classified based on their effectiveness on TH. For example, "hyperactive" IBPs from insects and from some bacteria induce TH of 2-13 °C. As the main function of many IBPs is to prevent cell freezing, they are often referred to as "antifreeze proteins". However, IBPs are present also in living beings that have ice crystals within cells or fluids and, therefore, their function is to help cells tolerating freezing rather than resisting it. In this context, the most remarkable effect of IBPs is the inhibition of ice recrystallization (IR). IR is the growth of large ice crystals at the expenses of smaller ones [126] and is very harmful for biological matter since it causes dehydration and cellular damage, particularly of cell membranes. Moreover, several microorganisms like bacteria, fungi, algae and diatoms secrete IBPs to create channels in iced water around cells to allow for the uptake of oxygen and nutrients [100]. Extracellular IBPs contain a conserved region classified in the Pfam database (http://pfam.xfam.org/) as "domain of unknown function" (DUF) 3494, and most of them carry a signal peptide for secretion at their amino-terminus [58, 100, 127].

Crystallographic structures available to date classify IBPs in at least 11 different folds, utilizing different strategies of structural stabilization such as networks of hydrogen bonds and/or disulfide bonds, and/or Ca^{2+} stabilization, whereas the usual hydrophobic core of globular proteins is less relevant [7]. IBP active site is the protein surface devoted to interact with ice and is called Ice Binding Site (IBS). Again, different proteins adopt different solutions. Still, common features to most IBSs described to date are that they are quite extended, flat and hydrophobic surfaces and include threonine residues [7]. IBSs are mostly devoid of charged residues and often contain repeated amino acid sequences, consistent with their ability to mimic ice surface [6]. Even more puzzling than structural diversity are the effects of IBPs binding to ice crystals, since some IBPs are more active in TH and others in IR. Explaining the rationale of such differences is not straightforward [6]. Since it was reported that moderate and hyperactive IBPs bind to different planes of ice crystals [33], the concept was developed that IBP properties depend on their specific spatial interaction with ice [6]. However, what drives IBPs to associate to a specific crystal face is still an open issue.

Here we describe the features of a bacterial ice binding protein, whose coding sequence was identified in the metagenome of bacterial symbionts of *Euplotes focardii*, a free-swimming psychrophilic ciliate endemic of the oligothrophic coastal sediments of Terra Nova Bay, in Antarctica. Previous studies on this single cell organism contributed to the understanding of the

molecular bases of cold adaptation and suggested a pivotal role for ice binding proteins [115, 117, 128]. The sequence studied in this work was identified upon sequencing the *E. focardii* genome. This analysis showed that out of the 201,918 contigs identified, 11,179 (from 100 to 25,584 bps) did not contain the telomeric repeats typical of *Euplotes* nanochromosomes (CCCCAAAA-3'/3'-GGGGTTTT-5') and were attributed to marine bacteria on the basis of a comparison with all bacterial genomes available in the NCBI data bank. Analysis of the 16S RNA sequences [129] revealed that major bacterial genera were either Bacteroidetes (16%) or Proteobacteria (78%). Search of IBP sequences within genomic contigs was carried out by Blast analysis, using IBP genes from the diatom *Fragilaropsis cylindrus* as the query. A contig of 3221 bps was found to contain an ORF for a putative IBP of 253 amino acids (GeneBank code AHG59376 [15]). In this work, we show that the recombinant protein *Efc* (*Euplotes focardii* consortium) IBP is stable to freezing and thawing, exerts a moderate effect of cryo-protection of pure proteins and whole bacterial cells and displays a remarkable activity in inhibiting ice recrystallization even at very low concentration.

Results

Attempts to produce the recombinant protein in *E. coli* failed whatever the conditions applied (data not shown). Analysis of sequence AHG59376 by Prosite [130] and SignalP 4.1 [131] suggested that an N-terminal stretch of 23 amino acid residues (MKKIKITMLTATVLFGLLTVVGC) may be a signal for anchorage to the cell surface or for protein transport [117]. Therefore, we designed a sequence devoid of the N-terminal stretch that is referred along the paper as *Efc*IBP. Production of the recombinant protein was assayed in *E. coli*, at different temperatures and in different growth media as reported in Materials and Methods. The highest yield of soluble *Efc*IBP was achieved after 16-hour incubation at 25°C in ZYM-5052 medium [132]. The yield of *Efc*IBP, determined after affinity chromatography purification, was ~2 mg from 1 L culture. Under the same conditions we obtained ~8 mg of GFP from 1 L culture (**Fig. 1**).

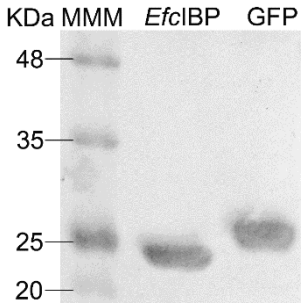

Figure 1. SDS-PAGE of recombinant proteins purified by affinity chromatography. MWM: molecular weight marker. Each lane contains ~ 5 μg of purified protein.

Secondary structure and conformational properties of *Efc*IBP

Fourier Transform Infrared (FTIR) and Circular Dichroism (CD) spectroscopies were applied to investigate the composition in secondary structure and the conformational stability of *Efc*IBP (**Fig. 2**).

FTIR analysis was performed in the Amide I region, where the signal is mainly due to C=O stretching vibrations of the peptide bond, which is particularly sensitive to the polypeptide secondary structures. **Figure 2A** shows the second derivative spectrum [133] of *Efc*IBP and bands are assigned as described in [134].

The spectrum is dominated by a component at ~ 1634 cm^{-1}, assigned to native β-sheet structures. The component at about 1653 cm^{-1} occurs in the spectral region of α-helices and random coils, and peaks at ~1669 cm^{-1}

and ~1689 cm^{-1} can be assigned to turn and turn/β-sheet structures, respectively.

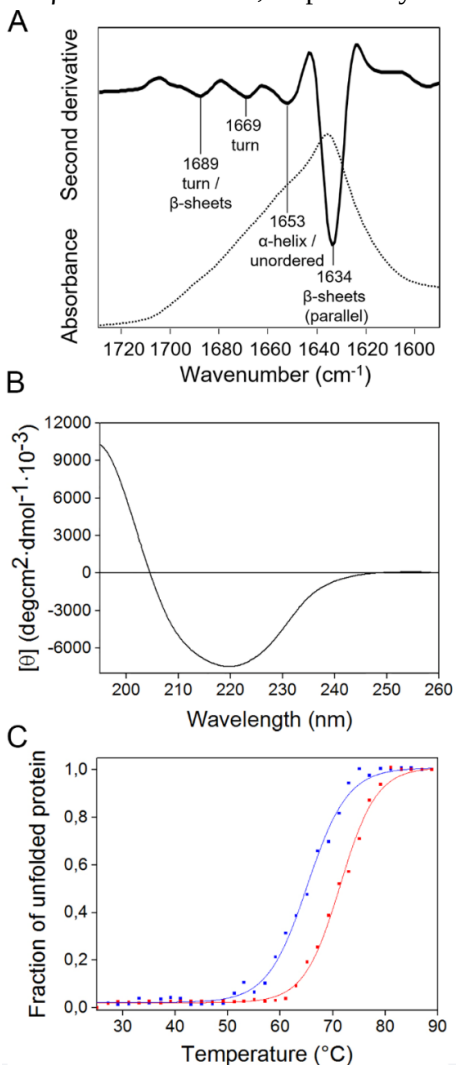

Figure 2. Secondary structure analysis of *Efc*IBP. A) FTIR absorption spectrum (dotted line) and second derivative spectrum (continuous line) of *Efc*IBP (40 µM). B) far-UV CD spectrum of *Efc*IBP (8 µM). C) Heat stability of *Efc*IBP (in blue) and GFP (in red, 8 µM). Ellipticity at 215 nm was recorded during heating from 25 °C to 90 °C. Initial CD signal was normalized to 100%.

The ratio of peak intensity at ~1689 and ~1634 cm^{-1} indicates a parallel orientation of the β-sheet structures. Indeed, as suggested by theoretical and experimental works [134, 135], in the Amide I region the presence of parallel β-sheets is revealed by either a single band at 1640-1623 cm^{-1} or by this signal together with a very low intensity peak at 1695-1675 cm^{-1}.

The high content of β-sheet structures in the *Efc*IBP protein is also highlighted by its CD spectrum displaying a negative band at ~ 219 nm and positive ellipticity at ~ 195 nm (**Fig. 2B**). Accordingly, the 3D structural model built using the structure of the IBP from *Flavobacterium frigoris* (33.5% sequence identity) as the template, predicts a mainly-beta structure. The model is showed later on, in the frame of the discussion on IBS sites **(Fig. 10)**.

In order to investigate the robustness of the *Efc*IBP structure towards freezing and towards repeated freezing and thawing steps (FT), we analysed by FTIR and near-UV CD spectroscopies the structure of the protein stressed by up to 14 FT cycles followed by overnight freezing, as described in Material and Methods.

For the sake of completeness, we show also results obtained with GFP, used as a probe to assess the performances of *Efc*IBP as a cryoprotectant (see later). GFP is similar to *Efc*IBP as for size and for the prevalence of beta elements in the secondary structure. Changes in the secondary structure of both proteins revealed by FTIR spectra are hardly detectable (data not shown), whereas effects on the tertiary structures are different and protein-dependent (**Fig. 3**). Indeed, after FT cycles, we observed a small loss of intensity (-15% at 287 nm) in the near-UV CD spectra of *Efc*IBP (**Fig. 3A**). Under the same conditions of freeze-thaw cycles, the TH values were not affected. These results show that structural and functional properties of this IBP are suitable to cope with low temperature and freezing stresses. On the other hand, the spectrum of native GFP revealed a marked flattening of the signal, mainly around 279 nm, where the signal loss is 70% (**Fig. 3B**).

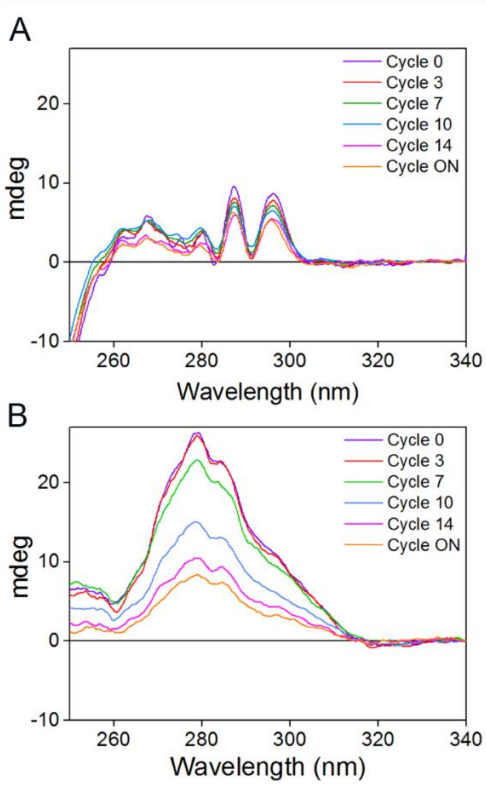

Figure 3. Robustness of *Efc*IBP (A) and GFP (B) analysed by near-UV CD spectroscopy. Spectra were acquired in PB before freezing (cycle 0), upon several cycles of FT and upon further overnight freezing following the 14th FT cycle (cycle ON).

To gain a more complete view about the proteins temperature sensitivity, we analysed both *Efc*IBP and GFP by CD spectroscopy, monitoring ellipticity changes at 215 nm in samples heated from 25 °C to 90 °C (**Fig. 2C**). Above ~ 60 °C, the ellipticity signal of *Efc*IBP was rapidly lost with midpoint at ~ 66.4 ± 2.7 °C. The appearance of visible protein precipitates in the cuvette suggested that aggregation occurs. Similar behaviour has been reported for *Le*IBP and *Ff*IBP, two homologous of *Efc*IBP with midpoint temperature of 61 °C and 56.4 °C respectively (**Table 1**) [106]. GFP displayed higher thermal stability with a midpoint of signal loss at ~ 71.4 ± 0.8 °C. From these data we surmise that *Efc*IBP not only well withstands repeated freezing and melting, but is also surprisingly thermostable, although less than GFP. Temperature stability of proteins from psychrophilic organisms may sound counterintuitive. However, stability may be a side effect to the rigidity necessary for IBPs when binding to ice crystals. In fact, according to the anchored clathrate waters mechanism the ice binding sites of IBPs need to be well positioned to allow water molecules to be arranged on top of it in an ice-like structure, that mimics ice crystals and allows binding of anchored water to a nearby ice crystal [123].

Ice-binding properties

The thermal hysteresis values of *Efc*IBP are similar to those of moderate fish AFPs [7] with activity of 0.53 °C at 50 µM concentration, as shown in the TH plot in **Figure 4A**. The activity at this concentration did not reach a plateau, indicating that higher concentrations may yield higher TH values. However, higher concentrations are more difficult to measure due to fast melting of superheated crystals. The same TH was obtained with 300 µM (2.1 mg/mL) of AFP type III. In comparison, 40 µM at 8 minute incubation time yield 1.1 °C for the *Tenebrio molitor* AFP, a representative of the hyperactive proteins [136].

The growth and melting patterns observed with *Efc*IBP differ from the bipyramidal patterns obtained with fish AFPs, and have some features similar to the shapes observed with hyperactive insect AFPs [29] and the ryegrass IBP [54] (**Fig. 4B**). Ice in the presence of *Efc*IBP appears to grow and melt layer-by-layer in the direction of the basal planes, leading to very thin ice crystals (**Movie S1**). Although the crystals do not grow when held at constant temperatures within the hysteresis gap, stepwise lowering of the temperature leads to step growth of the crystals, until the freezing point is reached and the crystals burst. Similar phenomenon

was noted with fish AFGPs, despite differences in crystal morphologies [29]. The step growth was less pronounced at higher concentrations, although it still occurred at 50 µM (1.2 mg/ml). Crystals that grew new ice layers within the TH gap did not continue to grow if held at a constant temperature. To check whether the protein accumulates on the ice surface over time, we incubated the crystal in 50 µM *Efc*IBP for 1 or 10 minutes before temperature lowering.

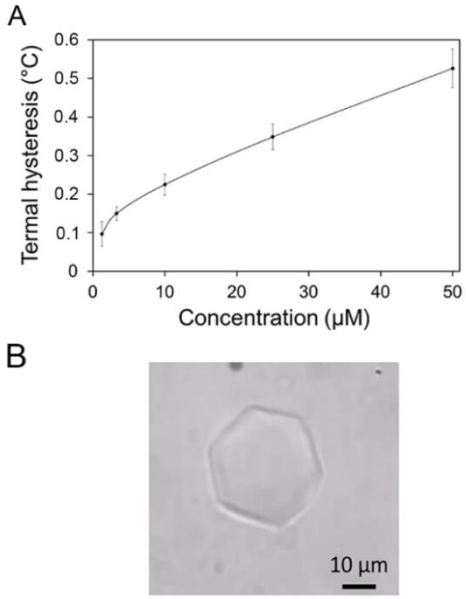

Figure 4. A) Thermal hysteresis activity of *Efc*IBP. See text for details. Each data point is the average of at least 3 measurements. Standard deviations are presented. B) Ice morphology in the presence of *Efc*IBP (~1 µM).

We did not detect any significant difference in TH values, indicating that *Efc*IBP bind fast (within the first minute) on the crystal surface. Still, after both annealing times, we observed step growth during the temperature decrease.

The IRI activity of *Efc*IBP is shown in **Figure 5.** We observed that 0.1 µM of protein was overall sufficient to inhibit IR, but some crystals did grow. At 1 µM *Efc*IBP, IR was completely inhibited. We calculated the IRI efficacy of *Efc*IBP following the analysis derived by Budke et al. [24] and compared it to the efficacy of type III AFP from ocean pout (*Zoarces americanus*, QAE isoform named HPLC12). This fish IBP was chosen as a control since its TH activity is in the same range. The IRI efficacy (C_i) is the inflection point of a curve that describes the dependence of IR rate on protein concentration (**Fig.6**). The C_i value represents the concentration of *Efc*IBP below which the IRI is not effective. We found that the C_i of *Efc*IBP is 0.0025 (±0.0006) µM. For comparison, we measured IRI for ocean pout type III AFP and found a C_i value of 0.05 (±0.02) µM. The effectivity of *Efc*IBP in IRI is 20-fold higher than type III AFP and it is also very high compared to other IBPs [25, 26] . Values of C_i in the nanomolar range were previously reported only for antifreeze glycoproteins [25].

Cryoprotection assays

The biological activity of *Efc*IBP was explored in experiments of cryoprotection of a single pure protein (GFP) and of whole *E. coli* cells. In the first set of experiments, purified GFP was exposed to FT treatment in the presence of 0.6 µM *Efc*IBP or other proteins known to be either active (BSA) or inactive (lysozyme) as cryo-protectors [137].

GFP fluorescence was measured before freezing, after 7 and 14 cycles of FT, and finally after 14 FT cycles and overnight freezing. Under these conditions, we observed a rapid loss of intrinsic fluorescence in GFP (**Fig. 7A**) likely as a result of denaturation induced by FT treatment and consistent with the results reported in Figure 3B. The fluorescence decay was milder in the presence of *Efc*IBP and of BSA, but not in the presence of lysozyme, used as a negative control (**Fig.7A**).

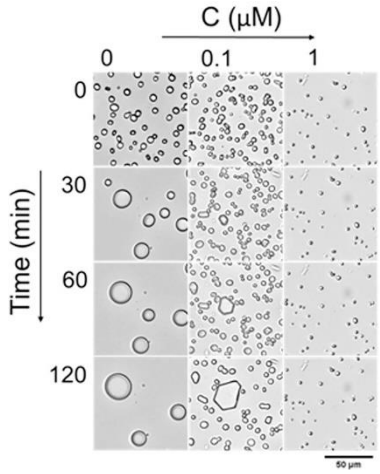

Figure 5. Ice recrystallization inhibition by *Efc*IBP. A sucrose sandwich assay with and without *Efc*IBP was carried for 2 h at an annealing temperature of -7.4 °C. Snapshots along the experiment are presented. The time lapse is noted to the left. Protein concentration in 45% sucrose solution is noted at the top.

To evaluate the protection effect of *Efc*IBP on whole cells we had to perform experiments at less severe temperature, since *E. coli* exposed to FT according to the previous schema was not viable. *E. coli* BL21 (DE3) cells were incubated at a temperature close to the water freezing point in the presence of either 50% (v/v) glycerol or of different proteins (1 mg/mL) as in the previous experiment. Cell viability was assayed every two days, by counting colony forming units (CFUs) formed by cells exposed to cold treatment (**Fig. 7B**). After 12 days, the percentage of viable cells was 6.50 % for cells in phosphate buffer (PB) and lysozyme, 9.21% for samples with BSA, 24.6% for samples containing *Efc*IBP and 35% for those with glycerol.

Structure and function in the context of IBP evolution

The maximum likelihood phylogenetic tree (**Fig. 8**) built with 29 selected sequences from bacteria and eukaryotic microorganism (mostly cold adapted) placed *Efc*IBP within the *Stigmatella aurantica* AFP/IBP lineage. With the exception of *Fimbriimonas ginsengisoli*, the members of the cluster are Antarctic or cryophilic microbes.

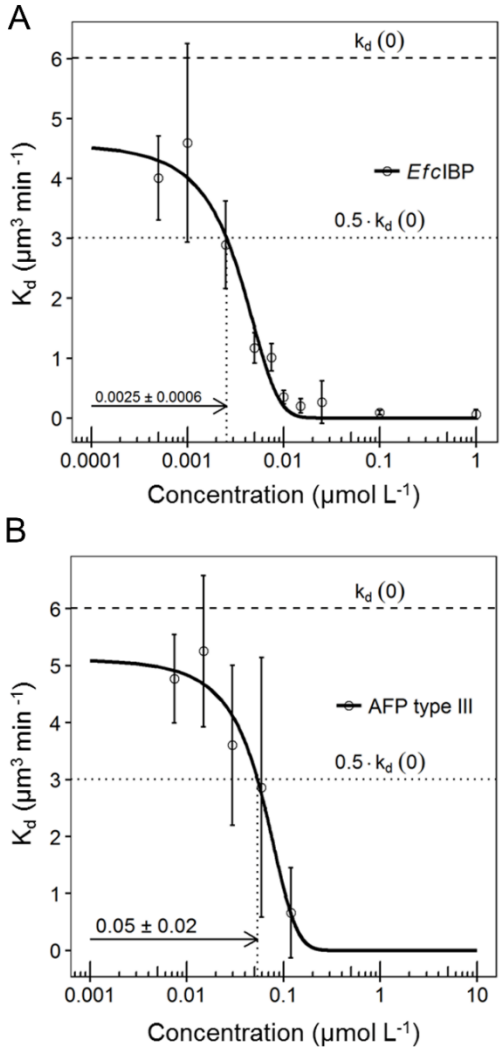

Figure 6. Quantitative ice recrystallization efficacy of *Efc*IBP and type III AFP. The recrystallization rate constant K_d was measured as a function of protein concentration. Standard deviations are shown. The inflection point of the curve is the intercept of the dotted lines. The C_i values are noted at the bottom left. A) *Efc*IBP. B) Type III AFP (HPLC12 isoform from ocean pout).

The same result was obtained when aligned sequences were restricted to 23 IBPs containing a Domain of Unknown Function (DUF) 3494 retrieved from Pfam server

[138] using the *Efc*IBP amino acid sequence as the query (**boxed in Fig. 8**).

To integrate functional and structural analyses, we restricted the cluster to 8 IBPs with over 30% sequence identity to *Efc*IBP and whose TH activity had been determined (**Table 1**) [71, 91, 92, 96, 98, 99, 106, 139]. The 3D structure of three IBPs included in the comparison (*Ff*IBP, *Le*IBP and *Col*AFP) is known and consists in a β-helix with an α-helix alongside the main axes of the protein [71, 96, 106]. Structural information allowed building the structure-driven multiple alignment showed in **Figure 9**.

The alignment highlights high conservation in both primary and secondary structures, as well as in the sequence of IBSs **(Fig. 10A)**, with a mean sequence identity of 26.3%, 23.7% and 23.9% with the IBSs of *Ff*IBP, *Le*IBP and *Col*AFP, respectively. A high content of polar residues is observed, in particular threonine and serine. In the structural model, some of these polar amino acids (highlighted in cyan in **Figure 10A**) line up on β-sheets, on the same face of the protein, suggesting a putative ice binding face (**Figure 10B**).

We observed that, in spite of sequence and structure conservation, considered IBPs display different TH activity. We are aware that comparison of TH determined by different Authors is not straightforward because of possible discrepancies in concentration and in the analytical methods. However, with all due caution, data available point to a non-relatedness of general structural organization and TH.

Data on IRI, unfortunately, are still too sporadic to be included in the analysis. In case of *Fc*AFP, IRI activity is 1.2 μM and 0.12 μM in low- and high-salinity conditions, respectively [91].

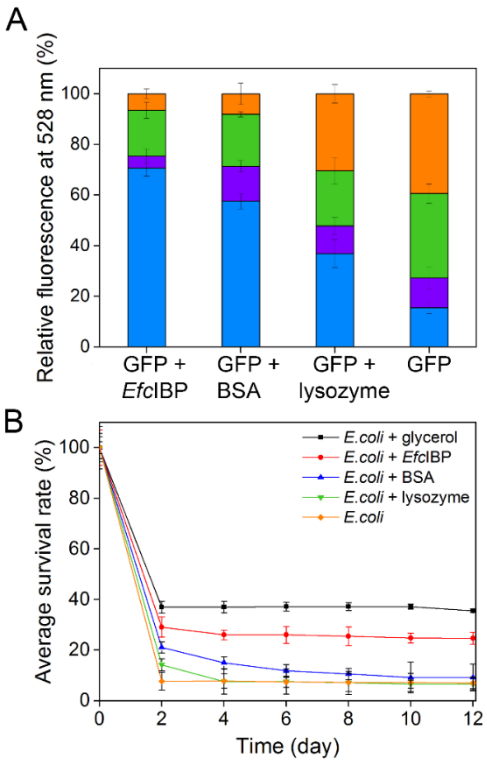

Figure 7. Cryoprotection assay. A) Cryoprotection of GFP. GFP fluorescence in the presence of cryoprotectants was acquired before freezing (orange), after 7 (green) and 14 cycles (purple) of FT and after a further overnight freezing following the 14th FT cycle (blue). Initial fluorescence was normalized to 100%. Excitation was at 474 nm and spectra were recorded at 528 nm in PB. Each data point is the average of 4 measurements. Standard deviations are shown. B) Cryoprotection of *E. coli* BL21 (DE3) cells. Cells viability in the presence of cryoprotectants was determined in terms of CFUs at different time points in the course of a 12-day incubation at ca. 0°C. For each sample, the number of viable cells before chilling was taken as 100%. Each data point is the average of 3 measurements. Standard deviations are shown.

Discussion

As the body of knowledge increases, the heterogeneity of proteins able to bind to ice becomes more and more evident. The widespread occurrence of IBPs within organisms unrelated to each other and the

striking variety of sequences, structures and functional strategies is considered as a proof of recent evolution pathways aimed at providing cells and tissues with defences against intracellular and environmental freezing. Polar marine environments are being intensively investigated in the frame of programs for the study and exploitation of biodiversity and provide a rich reservoir of novel organisms.

*Efc*IBP shows structural and functional properties common to IBPs, but also a combination of TH and IRI activity not previously described in a bacterial IBP. In particular, we detected a very effective IRI (C_i values of 2.5 nM) showing that *Efc*IBP is among the best performing IBPs described to date. Moreover, *Efc*IBP has TH activity and it can stop a crystal from growth when held at a constant temperature within the TH gap. Yet the observed stepwise growth of a crystal when the temperature is lowered but not below the hysteresis freezing point indicates that *Efc*IBP is less efficient in preventing ice from growth at these conditions. Altogether these data suggest that freezing point depression is not likely to be the natural role of this IBP. Rather, *Efc*IBP may serve to depress ice recrystallization or have an effect on preservation of liquid environment in the vicinity of the consortium. IRI activity was demonstrated in several IBPs secreted by microorganisms that inhabit icy niches, in particular in communities of microorganisms living in sea ice [140]. Such a role would support the importance for *E. focardii* of living together with a bacterial community able to secrete an IBP or at least to export it to the cell surface and is consistent with the cryoprotection effect observed when the IBP is supplemented in sufficient amounts. In the absence of direct evidence about protein transport, the hypothesis of secretion is substantiated by two observations that are the presence of a putative sequence of transport/anchorage to the cell membrane at the amino-terminus and the identification of a DUF3494 domain common to several secreted IBPs [127]. Still to clarify is the function of this IBP within the cell consortium as it might well be active in the structuring of ice around the ciliate cells but could also play a role when in association with the ciliate cells surface. Such a function has been shown for the Antarctic moss *Bryum argenteum* that accumulates proteins on its surface [58]. Either anchored at the outer cell surface or concentrated around cells, this protein might provide survival advantages to the entire consortium and may have contributed to the successful colonization of the Antarctic habitat by the ciliate.

.

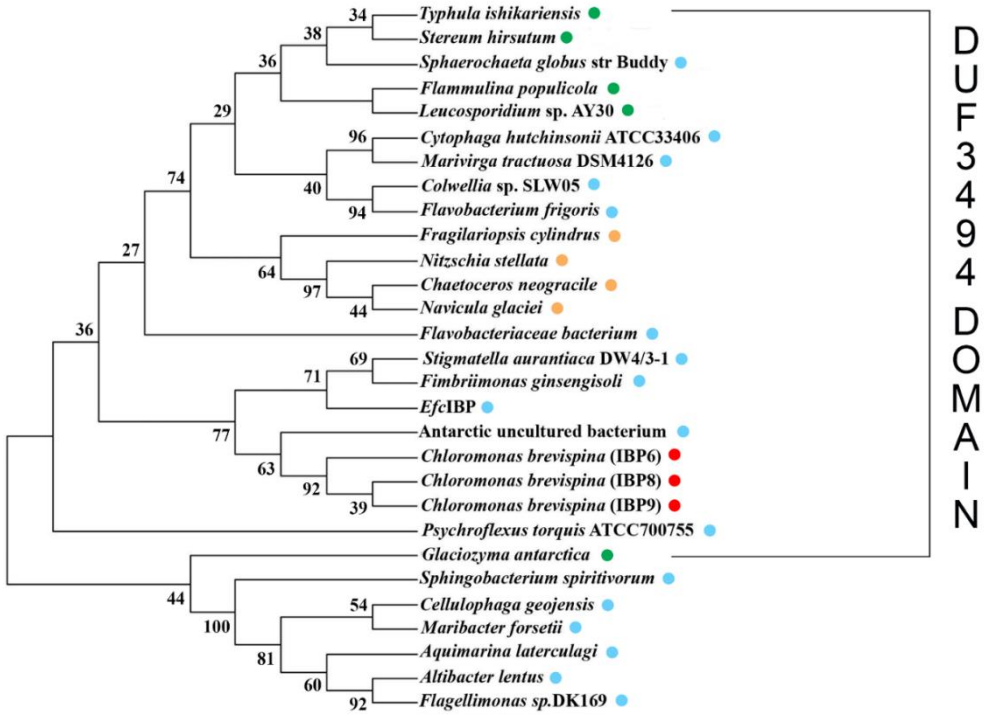

Figure 8. Phylogenetic tree based on amino acid sequences of ice binding proteins from fungi, bacteria, diatoms and algae (maximum likelihood method on JTT matrix, 1050 bootstraps). Branches reproduced in less than 50% bootstrap replicates are collapsed. The percentage of bootstraps in which the associated taxa clustered together are shown next to the branches. The bullets indicate the sequences obtained from fungi (green), bacteria (blue), diatoms (orange) and algae (red). The sequences were obtained from the NCBI database with the following codes: *Sphaerochaeta globus* (str.Buddy), YP_004248731; *Navicula glaciei*, AAZ76251; *Fragilariopsis cylindrus*, CN212299; *Fragilariopsis curta*, ACT99634; *Chlamydomonas* sp., EU190445; *Typhula ishkarioensis*, BAD02897; *Flammulina populicola*, ACL27144; *Lentinulaedodes edodes*, ACL27145; *Glaciozyma antarctica* ACX31168; *Psychromona ingrahamii*, ZP_01349469; *Colwellia* sp., DQ788793; *Deschampsia antarctica*, ACN38296; *Lolium perenne*, ACN38303, *Marivirga tractuosa* (strain DSM4126), YP_004052221, *Cytophaga hutchinsonii* (strain ATCC33406), YP_676864; *Chaetoceros neogracile*, ACU09498; *Nitzschia stellata*, AEY75833; *Psychroflexus torquis* (strain ATCC700755), YP_006867144; *Stigmatella aurantiaca* (strain DW4/3-1), gi_115375670; an uncultured bacterium (EKD52074.1), *Stereum hirsutum* FP-91666 SS1, XP_007299923.1; Antarctic unidentified bacterium, gi|930810610|gb|ALG05165.1; *Chloromonas brevispina* IBP 6, 8, 9, gi|649907359|gb|AIC65766.1, gi|649907413|gb|AIC65768.1, gi|649907440|gb|AIC65769.1; *Fimbriimonas ginsengisoli* Gsoil 348, gi|663071654|gb|AIE83809.1; *Leucosporidium* sp. AY30gi|255709878|gb|ACU30806.1

Materials and Methods

Strains, media and production assays

E. coli BL21[DE3] (Novagen) was used as the host for heterologous expression. Production assays of recombinant *Efc*IBP were carried out in low-salt LB (tryptone 1%, yeast extract 0.5%, sodium chloride 0.5%), terrific broth (TB, tryptone 12%, yeast extract 24%, glycerol 4%, potassium phosphate monobasic 0.17 mM, potassium phosphate dibasic 0.72 mM) or ZYM-5052 medium [132], added of 100 mg/L ampicillin. In these analytical experiments, pre-cultures were grown in LB medium to OD_{600} ~ 0.6-0.8 and diluted 1:25 in different

media. Cultures in LB or TB medium were incubated at 30 °C to reach OD_{600} 0.6–0.8 before adding 0.2 µM isopropylthio-β-D-galactoside as inducer. Each induced culture was subdivided in three shaking flasks and incubated at different temperatures (13, 30 and 37 °C). Samples were withdrawn after 2, 4, 18 hours, with additional samples obtained after 48 and 72 hours from the 13 °C cultures. Analytical cultures in ZYM-5052 medium were incubated at 13 and 25°C, for 16 - 72 h, depending on incubation temperature and samples withdrawn at the end of incubation.
.

Table 1. TH activities of *Efc*IBP homologs. Identity with *Efc*IBP was calculated on full-length sequences.

Protein ID	**Organism**	**Identities**	**TH activity**	**Reference**
*Efc*IBP	Bacterium consortium of *Euplotes focardii*	-	0.53 °C at 50 µM	This work
*Col*AFP	*Colwellia sp.* strain SLW05	37.3%	3.8 °C at 0.14 mM	[96]
*Ff*IBP	*Flavobacterium frigoris* PS1	33.5%	2.5 °C at 50 µM	[106]
*Fc*AFP	*Fragilariopsis cylindrus*	30.9%	0.9 °C at 350 µM	[91]
*Cn*AFP	*Chaetoceros neogracile*	36.3%	0.8 °C at 40 µM	[92]
*Nag*IBP	*Navicula glaciei*	33.5%	3.2 °C at 1.6 mM	[99]
*Tis*AFP8	*Typhula ishikariensis*	35.4%	2 °C at 180 µM	[139]
Afp4	*Glaciozyma antarctica*	31.3%	0,08°C at 200 µM	[98]
*Le*IBP	*Leucosporidium sp.* AY30	33.2%	0.35 °C at 370 µM	[71]

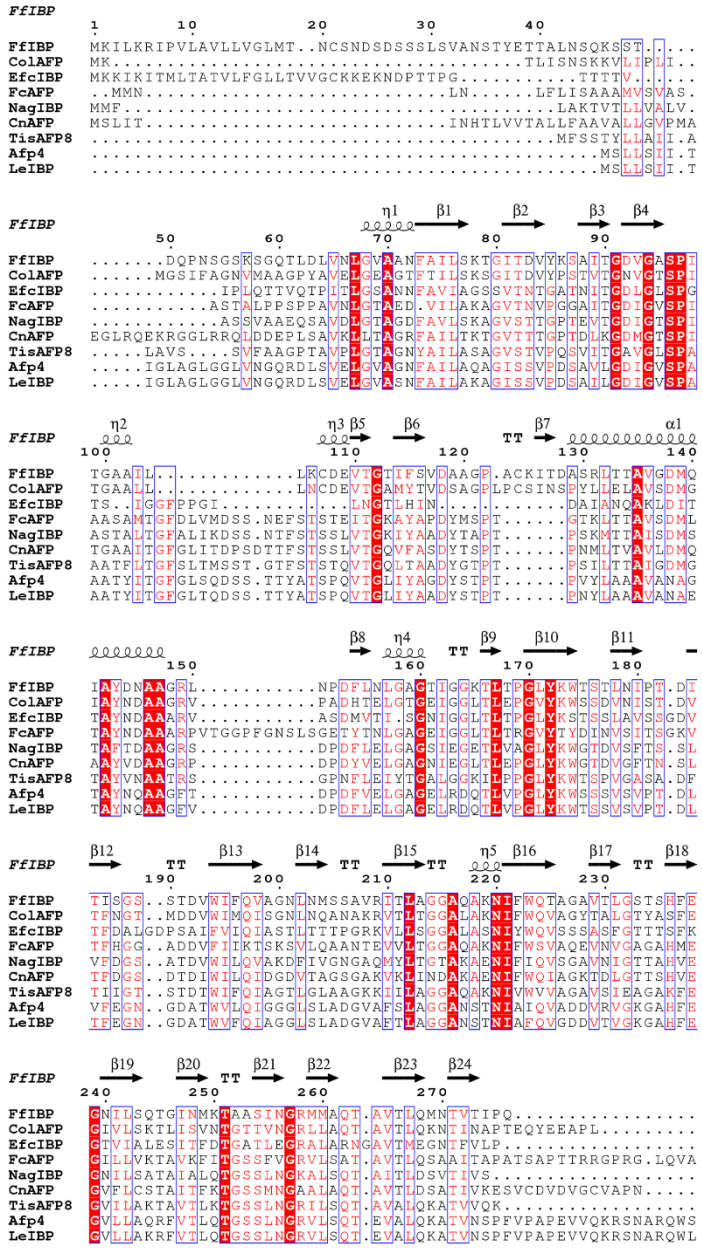

Figure 9: Structure-based amino acid sequence alignment of *Efc*IBP and other DUF3494 IBPs from *Colwellia* sp. strain SLW05 (*Col*AFP), *Flavobacterium frigoris* PS1 (*Ff*IBP), *Leucosporidium* sp. AY30 (*Le*IBP), *Typhula ishikariensis* (*Tis*AFP8), *Navicula glaciei* (*Ngl*IBP) *Fragilariopsis cylindrus* (*Fc*AFP) and *Chaetoceros neogracile* (*Cn*AFP) using **ESPript** [141]. At the top are indicated alpha helixes (helixes), 3_{10} helixes (η), beta strands (arrows), strict β-turns (TT) and strict α-turns (TTT) extracted from the tertiary structure of *Ff*IBP (PDB: 4NU2 [106]). Residues strictly conserved have a red background, residues well conserved are indicated by red letters. Both strictly and well conserved residues are framed in blue box. The alignment includes the full-length sequence of each protein

Cloning of the *Efc*IBP coding sequence

*Efc*IBP gene corresponds to nucleotides 70-762 of the genomic sequence *Efsymb*AFP previously described by [115]. The sequence encoding *Efc*IBP was amplified by PCR using a forward primer (5'-**CATATGAAGAAAGAAAAGAACGAT**-3') that inserts in 5' the initial ATG along with the restriction site for *Nde*I (underlined) and a reverse primer (5'-**CTCGAGCGGCAGAACAAA**- 3') that inserts in 3' the restriction site for *Xho*I (underlined). Reactions were carried out using MyCycler (Bio-Rad) under the following conditions: 1 cycle (95° C for 5 min), 30 cycles (95° C 1 min, 54° C 1 min, and 72°C 1 min), and a final cycle of 72 °C for 7 min. PCR products were cloned in frame with a sequence coding for C-terminal 6xHis-Tag into the pET-21a expression

vector previously cleaved with *Nde*I and *Xho*I to obtain pET-21 a[*Efc*IBP]. Sequence of cloned DNA was verified by bidirectional DNA sequencing.

GFP was produced from pET-19b [GFP] [142]. Type III AFP is a recombinant version of HPLC12, a type III isoform that belongs to the QAE subgroup of IBPs from ocean pout *Macrozoarces americanus.* The protein was produced in *E. coli* and purified as described elsewhere [143]

Production and purification of recombinant proteins

Production of recombinant *Efc*IBP and GFP was in ZYM-5052 [132] added of 100 mg/L ampicillin. Pre-cultures were grown in low-salt LB medium up to OD_{600} ~ 0.6-0.8, diluted 1:25 in ZYM-5052 and incubated overnight at 25 °C.

Proteins were purified by affinity chromatography using resin of Nichel-nitrilotriacetic acid agarose. Elution fractions containing the highest protein concentrations were pooled and buffer was exchanged to 10 mM ammonium acetate pH 7.0 by two consecutive gel filtrations on *PD-10* columns (GE Healthcare, Little Chalfont, UK) according to the manufacturer's instructions. Samples were lyophilized in a freeze-dryer (Heto FD1.0) and stored at -20°C or re-suspended in PB (25 mM sodium phosphate pH 7.0).

Protein concentration was determined by the Bradford protein assay (Bio-Rad, Hercules, USA), using bovine serum albumin as the standard. SDS-PAGE was on 14% acrylamide gels [144] stained with Coomassie dye (Bio-Rad, Hercules, USA) after electrophoresis. Broad-range, pre-stained molecular-weight markers (GeneSpin, Milan, Italy) were used as standards.

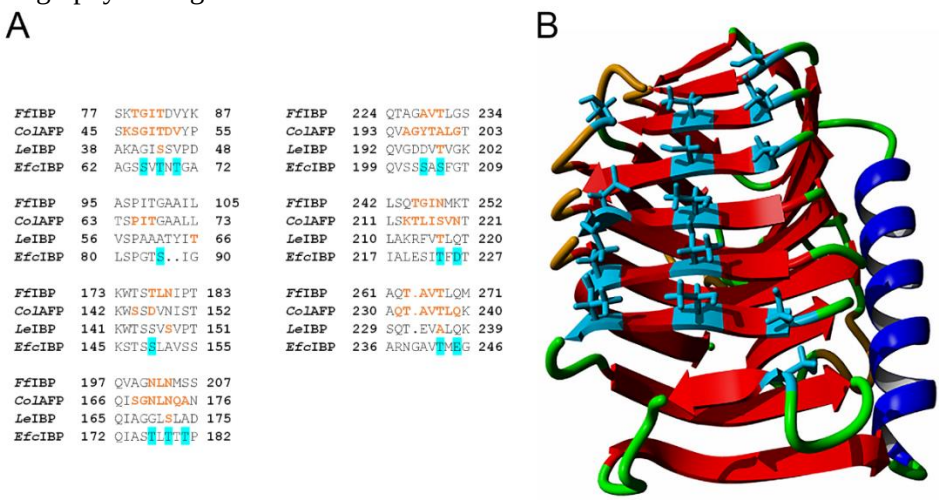

Figure 10: Ice binding site prediction. A) Sequence alignment of the IBSs from *Ff*IBP [106], *Col*AFP [96], *Le*IBP [71] and *Efc*IBP. The residues involved in ice binding are in orange bold. The polar residues located in β-sheet on the same face of *Efc*IBP are highlighted in cyan. The alignment includes the full-length sequence of each protein. B) Molecular model of *Efc*IBP. The 3D structure was modelled with SWISS-MODEL [145] using *Ff*IBP as a template [106]. β-sheets are indicated in red, α-helices in blue, coils in orange and turns in green. Sidechains of polar residues predicted to belong to IBS are in cyan.

Analysis of protein conformation and stability

CD spectroscopy

CD spectra of proteins dissolved in PB (8 µM for far-UV measurements and 40 µM for near-UV measurements) were recorded with a J-815 spectropolarimeter (Jasco Corp., Easton, MD, USA), using either 0.1-cm (for far-UV) or 1-cm path-length quartz cuvettes (for near-UV). Experiments were in duplicate.

Spectra in the far-UV were measured in the range 195–260 nm, while near-UV measurements were at 240–340 nm, with 0.1-nm data pitch and 20-nm/min scanning speed. All spectra were corrected for buffer contribution, averaged from two independent acquisitions, and smoothed by using a third-order least square polynomial fit.

Thermal denaturation spectra were obtained measuring the CD signal at 215 nm fixed wavelength when progressively heating the sample from 25 to 90 °C. Measurements were performed with a data pitch of 0.2 °C and a temperature slope of 5 °C/min.

Mean ellipticity values per residue [θ] were calculated as:

$$[\theta] = \frac{3300 \cdot m \cdot \Delta A}{c \cdot n \cdot l}$$

where ΔA is the difference in the adsorption between circularly polarized right and left light of the protein corrected for blank, m is the protein molecular mass in daltons, l is the path length (0.1 cm), c is the protein concentration (mg/ml) and n is the number of residues [142].

FTIR spectroscopy

FTIR spectra in attenuated total reflection (ATR) were collected by using the Quest device (Specac, UK) equipped with a single reflection diamond element. Aliquots of 2 µl of protein solution (40 µM in PB) were deposited on the ATR plate and dried at room temperature in order to obtain a protein film. ATR/FTIR spectra were then measured using a Varian 670-IR spectrometer (Varian Australia PtyLtd., AU) under the following conditions: 2-cm^{-1} spectral resolution, 25-kHz scan speed, 512 scan co-additions, triangular apodization and nitrogen-cooled mercury cadmium telluride detector. Absorption spectra were corrected for buffer contribution and normalized to the Amide I band intensity. Analyses of spectra were performed with the software Resolutions-Pro (Varian Australia Pty Ltd, AU).

Assessment of stability to freeze and thaw (FT)

IBP and GFP samples (40 µM) were subjected to up to 14 cycles of freezing (-20°C for 20 min) and thawing (25°C for 10 min) or to 14 cycles of FT followed by overnight freezing (-20°C for 16 hours). Effects on protein structure were assessed by Near-UV CD and FTIR spectroscopies.

Ice binding assays

Thermal hysteresis and ice crystal morphology

We observed ice morphologies and determined TH using a LabVIEW-operated custom-designed nanoliter osmometer as described [14, 146]. Lyophilized proteins were recovered in double distilled water to 50 µM solution and diluted in 20 mM ammonium bicarbonate (pH 8.5). Rehydrated proteins exhibit the same secondary structure of freshly prepared, soluble samples, as revealed by FTIR spectra (data not shown). Samples of ~ 10 nL immersed in oil were cooled until freezing (~ -30 °C) and then warmed until a single ice crystal of less than 20 µm diameter remained. The melting temperature of the crystal was measured and then the crystal was incubated for 1 or 10 min at a few hundredths of a degree below the melting point. After incubation, the temperature was

reduced by 0.01 °C every 4 or 10 sec and the crystal image was recorded. The temperature at which fast growth commenced was determined as the freezing point. The difference between the melting point and the hysteresis freezing points is the TH value.

Ice recrystallization inhibition

Ice recrystallization inhibition (IRI) was conducted using a sucrose-sandwich assay [147] with some modifications [24]. The final solutions contained 45% sucrose, 50 mM NaCl, 10 mM Tris (pH 8.0) and up to 1 µM of protein. One-µL samples were placed on a sapphire sample holder and covered with a 13-mm diameter circular glass cover slip. The sapphire was used to reduce temperature fluctuations. The sample was sealed with type-B immersion oil (Sigma-Aldrich, Saint Louis, Missouri, USA) to avoid evaporation and mounted on the stage of a Motorized Cryobiology System (model MDBCS196, Linkam, Surrey, UK). A copper plate with a 2.5-mm diameter slit was placed on top of the sample to further reduce temperature fluctuations. Immersion oil was used between the sample, the stage and the slit to improve thermal contact. The Linkam stage was placed on a light microscope (BX41, Olympus America Inc, NY) and operated using a Labview interface. The system was cooled from room temperature to -50 °C at a rate of 130 °C/min and sustained at -50 °C for 1 min. The temperature was then elevated to -20 °C at a warming rate of 130 °C/min and then continued to warm to -10 °C at a warming rate of 10 °C/min. The final stage of heating up to the annealing temperature of -7.4 °C was conducted at a slow rate of 1 °C/min to avoid overheating. The sample was maintained at this temperature for 60 min. During this period, recrystallization was recorded using a QImaging EXi Aqua bio-Imaging camera every 1 min. The experiment was carried out with different concentrations of protein and repeated at least three times for each concentration.

The IRI was calculated following the mathematical description derived by Budke et al. [24]. The images were processed using Fiji (public domain software) to calculate the number of crystals, the mean radius of the crystals, and the total crystal volume. The cube of the mean crystal radius was calculated for all images in each data set and plotted against time. The slope of the curve obtained from time points 30 min to 60 min was taken as the recrystallization rate constant. The ice volume fraction (Q) was also calculated for all images in each data set and only experiments with less than 1% variation in Q were considered. In all experiments the ice volume fraction was up to 9% (in high volume fraction the theory for IRI calculation is not legitimate). The recrystallization rates (K_d) were plotted against protein concentration, with at least three replicates for each concentration. This data set was fitted to a sigmoidal curve using R (public domain software). The inflection point of the curve, termed the C_i value, represents the effective protein concentration below which recrystallization is not efficiently inhibited [24]. A profile likelihood confidence interval (α=0.05) for the C_i point was calculated using "nlstools" R package. The rate constant for in the absence of protein ($K_d(Q)$ at [C]=0) was determined by measuring the recrystallization rate of buffer without protein. This experiment was repeated 8 times and the averaged $K_d(Q)$ value was used for curve fitting. To accommodate the possible effects of different Q, we extrapolated all K_d values for zero volume fraction Q=0 as described [24] and plotted the new K_{I0} values against protein concentration (data not shown). The difference between the original C_i value and the corrected C_i value was very small.

Cryoprotection assays

Cryoprotection of GFP

Fluorescence spectroscopy experiments were carried out to detect the effects of FT on GFP fluorescence in either the presence or the absence of the *Efc*IBP. All protein samples were dissolved or prepared in PB. Samples of GFP (0.6 µM) were mixed with equimolar concentrations of *Efc*IBP, or BSA (Sigma-Aldrich, Saint Louis, Missouri, USA), or lysozyme (Sigma-Aldrich, Saint Louis, Missouri, USA) or with PB alone, in a final volume of 500 µL in PB. Samples were divided in four 100-µL aliquots and deposited in a 96-multiwell plate to replicate each measurement. Plates were then frozen and thawed according to the scheme previously described "Assessment of stability to FT" section. Emission spectra were recorded before freezing, after 7 and 14 FT cycles and finally after overnight freezing. Fluorescence emitted from GFP was measured by a Cary Eclipse (Varian Inc., Palo Alto, CA, USA) spectrofluorimeter using 96 multiwell plates. GFP fluorescence was recorded at room temperature with excitation at 474 nm and emission at 528 nm. The experiment was repeated three times.

Cold-tolerance assays were carried out on *E. coli* BL21 (DE3) cells exposed to low temperature in the presence or in the absence of *Efc*IBP. Cells carrying empty plasmid pET21 (to confer ampicillin resistance) were grown in ZYM-5052 medium and incubated overnight at 25 °C until they reached an OD_{600} of ~3. One-mL aliquots of fresh culture were mixed with equal volumes of 1 mg/mL PB solutions of *Efc*IBP, or BSA (Sigma-Aldrich, Saint Louis, Missouri, USA), or lysozyme (Sigma-Aldrich, Saint Louis, Missouri, USA), or glycerol (50%) (Euroclone, Pero, Italy), or with PB alone as a control. Cell aliquots in 1.5-mL plastic tubes were kept submerged in ice for several days at the temperature of -0.5 °C. After 0, 2, 4, 6, 8, 10, and 12 days, samples were diluted in LB broth added with 100 mg/L ampicillin, and inoculated on LB-agar plates to count CFUs after 16-h incubation at 37 °C. Plates were inoculated in three replicates for each point.

Sequence analysis and modelling of 3D structure

The evolutionary history was inferred by using the maximum likelihood method based on the JTT matrix-based model [148]. The bootstrap consensus tree was inferred from 1050 replicates and assumed to describe the evolutionary history of the analyzed taxa [149]. Initial tree for the heuristic search was obtained by applying the neighbor-joining method to a matrix of pairwise distances estimated using a JTT model. The analysis involved 29 amino acid sequences. There were a total of 792 positions in the final dataset. Evolutionary analyses were conducted with MEGA5 [150]. Multiple alignments were performed by ESPript [141]. The 3D structure of *Efc*IBP was modelled on the structure of *Ff*IBP (PDB: 4NU2 [106]) using SWISS-MODEL [145]. *Efc*IBP displays a sequence identity of 33.5% compared to the *Ff*IBP. The resulting model was visualized using YASARA (www.yasara.org) and POVRay (www.povray.org).

Movie S1: Ice crystal growth. A single ice crystal grown in a solution containing 3.3 µM *Efc*IBP (Tm = -0.02). After incubation of 1 minute at -0.03 °C, the temperature (noted at the bottom as T (meas) was lowered. During the temperature decrease, events of growth occurred and then stopped (step growth). Eventually, at a temperature of -0.18 °C fast growth occurred, indicating the hysteresis freezing point. The TH measured is 0.16 °C.

https://febs.onlinelibrary.wiley.com/doi/full/10.1111/febs.13965

Acknowledgements
This work was supported by a grant of the Progetto Nazionale di Ricerche in Antartide PEA 2014-2016 entitled “Genome scanning and characterization of novel antifreeze proteins for industrial application” coordinated by DdP and by a grant of ERC to IB. AK acknowledges support by the *Estonian national scholarship program Kristjan Jaak*. We thank Dr. Lior Segev (Weizmann Institute of Science, Israel) for LabVIEW programming and Lotem Haleva for her contribution to TH analysis.

Author’s contribution
M. Mangiagalli and S. Brocca carried out production and purification of the recombinant proteins and assessed stability and cryoprotection activity; A. Natalello performed analyses by infrared spectroscopy; M. Bar-Dolev, A. Kaleda and I. Braslavsky characterized the TH and IRI activity and studied ice crystals morphology; P. Tedesco and D. de Pascale designed and produced the coding sequence; S. Pucciarelli and C. Miceli performed evolutionary analysis; D. de Pascale and M. Lotti conceived and supervised the project; M. Lotti wrote the paper. All Authors have read and approved the content of the manuscript.

Structure of a bacterial Ice Binding Protein with two faces of interaction with ice

Marco Mangiagalli[1], Guy Sarusi[2], Aleksei Kaleda[2,3], Maya Bar Dolev[2], Valentina Nardone[4], Vittoria Federica Vena[1], Ido Braslavsky[2], Marina Lotti[1*], Marco Nardini[4*]

[1]Department of Biotechnology and Biosciences, University of Milano-Bicocca, Piazza della Scienza 2, 20126 Milan, Italy; [2]Institute of Biochemistry, Food Science and Nutrition, The Robert H. Smith Faculty of Agriculture, Food and Environment, The Hebrew University of Jerusalem, Rehovot, 7610001, Israel; [3]Department of Chemistry and Biotechnology, School of Science, Tallinn University of Technology, Ehitajate tee 5, 19086 Tallinn, Estonia; [4]Department of Biosciences, University of Milano, Via Celoria 26, 20133 Milan, Italy

* corresponding authors

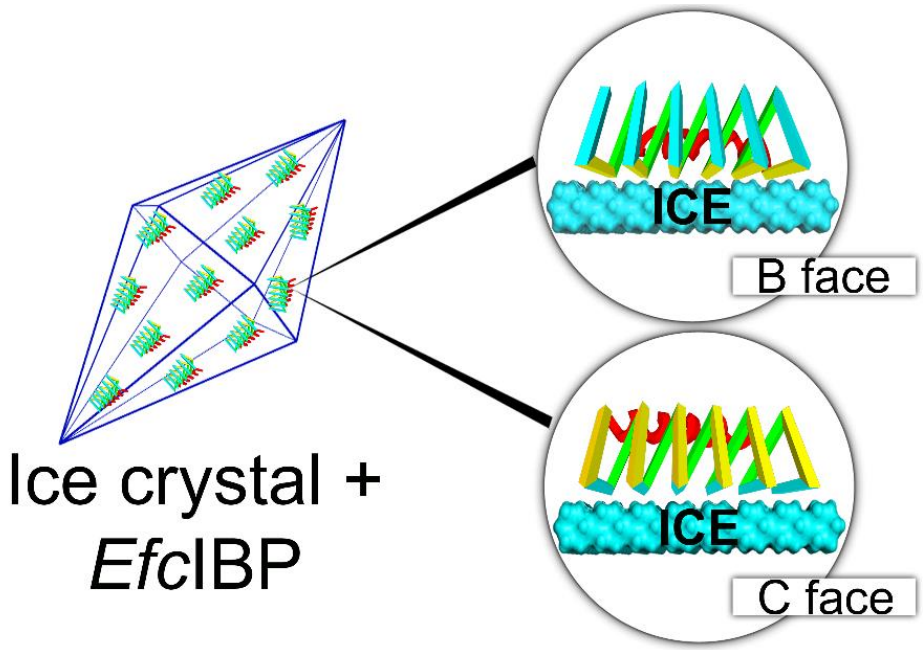

Keywords: cold adaptation, IBP-1 fold, DUF3494, thermal hysteresis, ice recrystallization inhibition.

The FEBS Journal 285 (2018) 1653–1666 2018 Federation of European Biochemical Societies
doi:10.1111/febs.14434

ABSTRACT: Ice Binding Proteins (IBPs) contribute to the survival of many living beings at sub-zero temperature by controlling the formation and growth of ice crystals. This work investigates the structural basis of the ice binding properties of *Efc*IBP, obtained from Antarctic bacteria. *Efc*IBP is endowed with a unique combination of thermal hysteresis (TH) and ice recrystallization inhibition (IRI) activity. The three-dimensional structure, solved at 0.84 Å resolution, shows that *Efc*IBP belongs to the IBP-1 fold family, and is organized in a right-handed β-solenoid with a triangular cross-section that forms three protein surfaces, named A, B and C faces. However, *Efc*IBP diverges from other IBP-1 fold proteins in relevant structural features including the lack of a "capping" region on top of the β-solenoid, and in the sequence and organization of the regions exposed to ice that, in *Efc*IBP, reveal the presence of threonine-rich ice-binding motifs. Docking experiments and site-directed mutagenesis pinpoint that *Efc*IBP binds ice crystals not only *via* its B face, as common to other IBPs, but also *via* ice binding sites on the C face.

Abbreviations

***Col*AFP**: *Colwellia* sp. strain SLW05 antifreeze protein; ***Efc*IBP**: *Euplotes focardii* bacterial consortium ice binding protein; ***Ff*IBP** *Flavobacterium frigoris* PS1 ice binding protein; **IBPv**: *Flavobacteriaceae* bacterium 3519-10 ice binding protein; **IBP**: ice binding protein; **IBS**: ice binding site, **IRI**: ice recrystallization inhibition; ***Le*IBP**: *Leucosporidium* sp. AY30 ice binding protein; **TH**: thermal hysteresis; ***Tis*AFP6**: *Typhula ishikariensis* antifreeze protein isoform 6; ***Tis*AFP8**: *Typhula ishikariensis* antifreeze protein isoform 8; **wt**: wild-type.

Introduction

Organisms living in cold habitats such as polar regions, high mountains, oceans or other cold environments of the Earth, permanently or seasonally have to cope with sub-zero temperatures. In several cases protection towards freezing and ice injuries is provided by "ice binding proteins" (IBPs) that bind ice crystals and control their growth and shape [151, 152]. Since the first description of an IBP from an Antarctic fish back in the '60s [8] these proteins have been identified in a number of fishes, insects, diatoms, algae, yeasts, fungi and bacteria [6, 7]. Over the years, the growing body of information available fostered the development of models and hypotheses to explain the peculiar features and properties of IBPs. Particularly challenging are the relationships between structure and activity. In fact, while IBPs structures are classified in at least 11 different folds [6], all of them associate to the very same ligand: ice crystals. This apparent paradox is justified by the presence of specific ice binding sites (IBSs) in all IBPs that share similar structural properties. IBSs are typically flat and extended surfaces, relatively hydrophobic, able to organize water into an ice-like arrangement that merges and freezes with the quasi-liquid layer next to the ice lattice [7]. In many cases, IBSs are also characterized by the presence of threonine-rich repeats, such as Thr-X-Thr or Thr-X-Asx, whose involvement in ice binding has been recognized by site-directed mutagenesis studies [49, 69, 74, 75, 123, 153].

Nevertheless, the correlation between structural differences and effects induced by IBPs on ice crystals growth and structuring, i.e. thermal hysteresis (TH) and inhibition of ice recrystallization (IRI), still wait for a comprehensive explanation. TH is the gap between the melting and the freezing points of ice produced by the adsorption of IBPs to the crystals. The bound IBPs induce micro curvatures on the growing ice front and, following the Gibbs-Thomson effect, the association of further water molecules on the ice is less favorable, leading to reduction of the freezing point below the melting point. IRI, instead, refers to the ability of IBPs to contrast the formation of large ice crystals from small ones [6, 154]. While TH is

relevant in avoiding freezing, IRI activity seems to be related to freeze tolerance, since injuries to living matter by large crystals are by far more severe than those produced by small ice particles, that can be tolerated inside or between cells [4]. On the basis of TH activity, IBPs are classified as moderate, with TH of 0.1-2.0 °C, or as hyperactive, with TH of 2-13 °C. Several lines of evidence support the idea that the extent of TH activity may depend on the specific plane of ice crystals to which the IBP adsorb. Most hyperactive IBPs bind to the basal plane of ice, in addition to the prismatic and pyramidal crystal planes to which moderate IBP associate [6, 76]. Data of IRI activity have been reported only for a subset of IBPs. Nevertheless, information available raises questions and issues about the mechanistic basis of TH and IRI which, in all major classes of IBPs, seem to be non-related [26]. This conclusion is also supported by mutagenesis experiments on an IBP from *Lollium perenne* showing that amino acid substitutions may decrease or increase IRI activity without changing TH [155].

A deeper insight in the molecular basis of IBP properties is required to advance our understanding of the evolution of this very peculiar cold adaptation strategy and of the IBP biological function. In fact, IBPs play different roles in distinct organisms, for example, they can restrain body fluids from freezing, promote ice structuring to preserve a liquid environment around cells, or mediate cells adhesion to ice [6, 7, 9].

In this work, we tackle IBP function from a structural viewpoint and we report the 3D structure at 0.84 Å resolution of an IBP derived from the metagenome of bacterial symbionts of the Antarctic ciliate *Euplotes focardii* (*Efc*IBP). *Efc*IBP shows atypical combination of TH and IRI activities, not reported for other bacterial IBPs, with moderate TH activity (0.53 °C 50 µM) and one of the highest IRI activity (2.5 nM) described to date. According to primary sequence analysis, *Efc*IBP contains a domain of unknown function DUF3494, which was predicted to fold in a discontinuous β-solenoid structure [93]. This fold is typical of bacterial IBPs, where is defined as IBP-1 fold [6], and it might have been horizontally transferred to other organisms sharing the same environment, such as algae, fungi, yeasts and diatoms [100, 102, 103, 140]. Our results show that *Efc*IBP is a novel member of IBP-1 family with a modified fold and the presence of repetitive IBS sequence motifs. Site-directed mutagenesis and docking simulations reveal how *Efc*IBP exerts its moderate TH activity. The IBS of *Efc*IBP presumably has two different protein surfaces characterized by low hydrophobicity and repetitive sequence motifs. This composite IBS allows binding to multiple ice planes, including the basal plane.

Results and discussion

*Efc*IBP structure

Recombinant *Efc*IBP was crystallized as described in the Experimental Procedures section. Crystals belong to the orthorhombic $P2_12_12_1$ space group and diffracted to the atomic resolution of 0.84 Å using synchrotron radiation (ESRF, Grenoble), one of the highest resolution reached for this kind of protein so far. The final model was refined to a final R_{work} =11.5% and R_{free} =12.8% with good stereochemical parameters, and contains 223 amino-acids (including the *Efc*IBP residues 37-253, and the C-terminal 6His-tag), 411 water molecules, 4 sulfate ions, and 1 glycerol molecule. Data collection analysis and refinement statistics are summarized in Table 1.

The *Efc*IBP displays an IBP-1 fold [6], consisting of a right-handed β-helix with a triangular cross-section formed by three parallel β-sheets (here named A, B, and C faces) and by an additional single α-helix (α1) aligned along the axis of the β-helix (**Fig. 1**). The A face is formed by nine β-strands and is not directly exposed to the solvent region, but screened by the α1 helix

and by the N-terminal region (residues 44-54) preceding the β1 strand (**Figs. 1 and 2**). This protein surface is, therefore, not suited for the interaction with ice crystals.

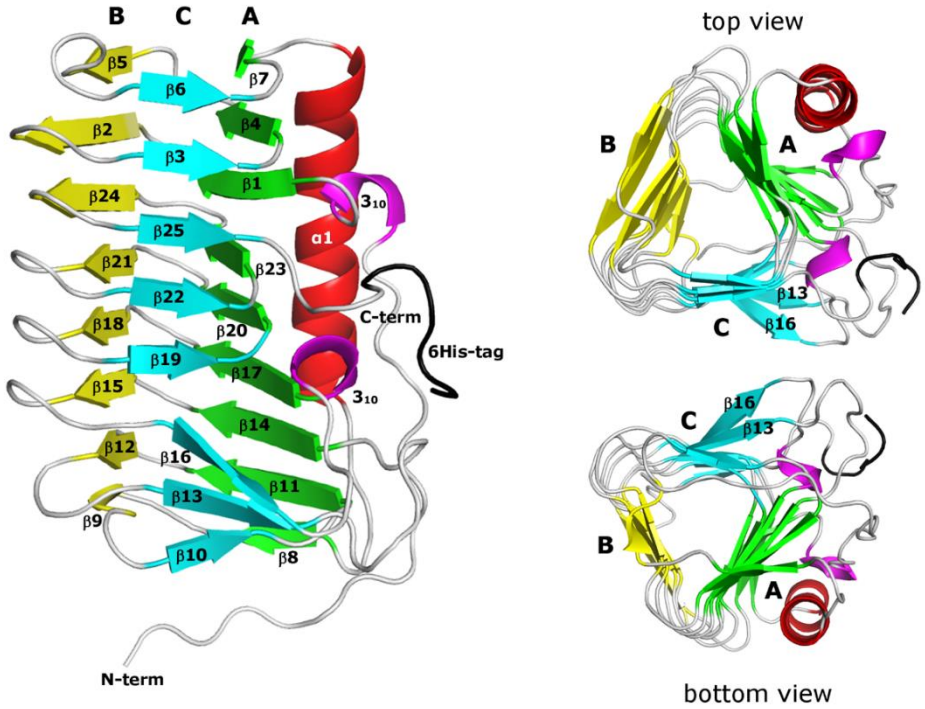

Figure. 1. Three-dimensional structure of *Efc*IBP. Ribbon diagram showing the secondary structure elements of *Efc*IBP: β strands belonging to the A, B, and C faces of the β-helix are in green, yellow, and cyan, respectively. The helix α1 is in red and the 3_{10} helices in magenta. The triangular section of the *Efc*IBP structure is evident in the top and the bottom views. The β13 e β16 strands, which diverge towards the outside from the core of the β-helix, are indicated.

The B and C faces are each formed by eight β-strands. The B face is flat and regular, while the C face is divided in two regions. The first region consists of strands β3, β6, β10, β19, β22 and β25, forming a flat surface that maintains the triangular section of the structure. Instead, strands β13 and β16 markedly diverge towards the exterior of the protein body (Fig. 1). The B and C faces are both fully exposed to the solvent region and, therefore, potentially involved in ice binding. Two shorts 3_{10} helices (one turn each) are also present in the *Efc*IBP structure. They are located just after a long loop region running outside of the protein solenoid and they seem to help the following β-strands (β1 and β17, respectively) to insert back into the β-helix core structure (**Figs. 1 and 2**).

The *Efc*IBP structure is very similar to other single domain IBP-1 fold proteins, specifically to those from *Colwellia* sp. (*Col*AFP; DALI Z-score of 32.3, residue identity of 38%) [96], from *Flavobacterium frigoris* (*Ff*IBP; DALI Z-score of 32.4, residue identity of 35%) [106], from *Typhula ishikariensis* (*Tis*AFP6 and *Tis*AFP8 isoforms; DALI Z-score of 31.0, residue identity of 37%) [72, 95], and from *Leucosporidium* sp. (*Le*IBP; DALI Z-score of 30.8, residue identity of 35%) [71]. Furthermore, *Efc*IBP matches well the structure of each domain of the two-domain IBP secreted by a *Flavobacteriaceae* bacterium (IBPv; DALI Z-score of 31.9 and 32.8, residue identity of 35% and 32%, for domain A and B, respectively) [108] (Fig. 2). Backbone comparison among these IBPs

highlights an excellent conservation of secondary structure elements within the central core of the β-helix and helix α1, with an RMSD in the 0.9-1.2 Å range, calculated over 198 Cα pairs (Figs. 2 and 3).

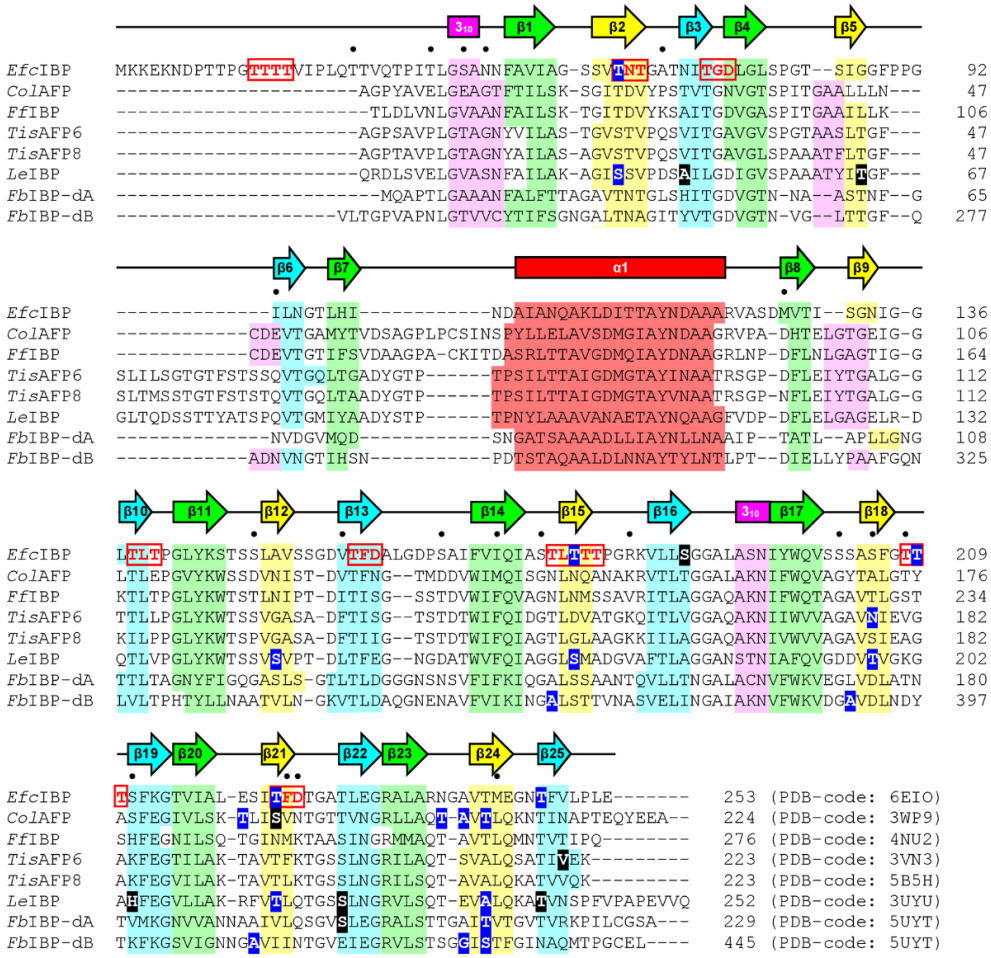

Figure. 2. Structural-base sequence alignment of *Efc*IBP with related IBP-1 fold proteins**.** *Efc*IBP is aligned with *Col*AFP [23], *Ff*IBP [24], *Tis*AFP6 and *Tis*AFP8 isoforms [25,26], *Le*IBP [27], and with the two domains (dA and dB) of IBPv [28]. The sequence alignment has been performed using the MUSCLE program (http://www.ebi.ac.uk/Tools/msa/muscle/) and manually corrected based on their 3D structure comparison. Secondary structure elements are indicated on top for *Efc*IBP and shaded (color code as in Fig. 1) for all aligned proteins. Residues mutated in *Efc*IBP, *Col*AFP, *Ff*IBP, *Tis*AFP6, *Tis*AFP8, *Le*IBP, and IBPv with decreased/unaltered ice-binding properties are shaded in blue/black, respectively. The *Efc*IBP repeat motifs Thr-X-Thr and Thr- X -Asx (x=any residue and Asx=Asn or Asp) are indicated in bold and boxed in red. *Efc*IBP amino acids with side-chains in a double conformation are indicated by a black dot.

Alongside the similarities between *Efc*IBP and other proteins with an IBP-1 fold, clear structural differences are present in the region from the end of strand β5 and the start of helix α1 (**Figs. 1 and 2**). The loop between strands β5 and β6 is 11 amino acid longer in *Tis*AFP6, *Tis*AFP8 and *Le*IBP, while in *Col*AFP, *Ff*IBP and in both domains of IBPv has similar length but different structure, compared to *Efc*IBP. The connection between β7 and α1 is also different, with an insertion of 12 amino acids

in *Col*AFP, 11 in *Ff*IBP and 6 in *Tis*AFP6, *Tis*AFP8 and *Le*IBP. This loop is similar in *Efc*IBP and in the A domain of IBPv, while the IBPv B domain has an insertion of one amino acid (**Fig. 2**). As a result, a cap subdomain is present between β5 and α1 in *Col*AFP, *Ff*IBP, *Tis*AFP6, *Tis*AFP8 and *Le*IBP, but not in *Efc*IBP and in the two domains of IBPv (Fig. 3). Within IBP-1 fold proteins, this cap region has been classified in two groups [106], depending on the presence (group 1: *Col*AFP and *Ff*IBP) or absence (group 2: *Tis*AFP6, *Tis*AFP8 and *Le*IBP) of a disulfide bridge between Cys residues belonging to the β5-β6 and β7-α1 loops. With this respect, *Efc*IBP, together with IBPv, can be classified as a novel third group, where the cap subdomain is totally absent. The role of the capping region in IBPs protein is debated. Studies on chimeras of *Ff*IBP and *Le*IBP showed that the capping region plays an important role in structure stabilization. The *Ff*IBP chimera, with the cap from *Le*IBP, has a Tm value of 47.4 °C, significantly lower than the wild-type (wt) *Ff*IBP (Tm value of 56.4 °C), with a concomitant decrease of TH activity (greater than sevenfold). On the contrary, chimeric *Le*IBP, with the capping head region of *Ff*IBP, had a slightly increased TH activity compared with wt *Le*IBP and a higher Tm value (66.4 °C *vs* 61 °C). Thus, the capping head region of *Ff*IBP is more stable than that of *Le*IBP, likely due to the presence of the disulfide bond, and is important for the overall stability of IBP [106]. Interestingly, recombinant *Efc*IBP is very stable to heat, with a Tm of 66.4 °C, despite the absence of the capping region [18].

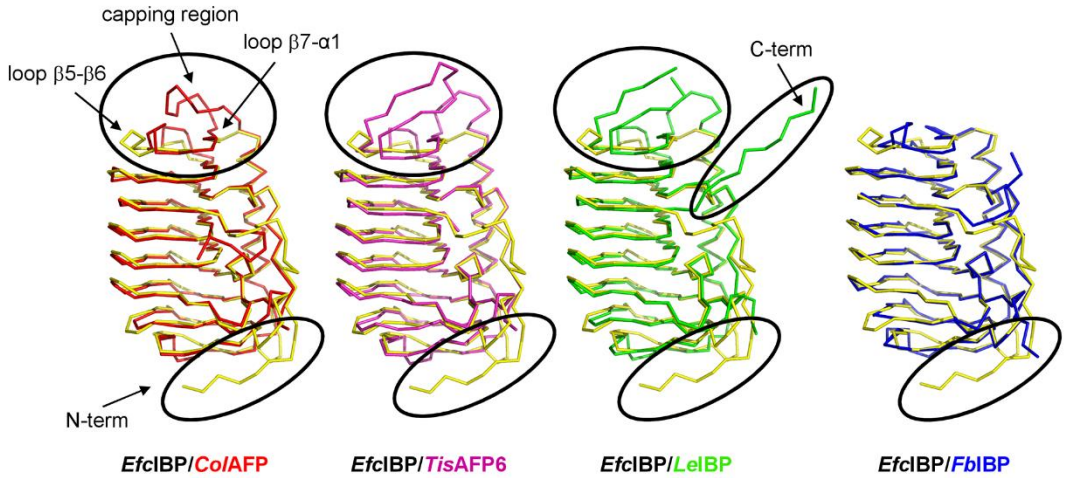

Figure 3. Structural superposition of *Efc*IBP with related IBP-1 fold proteins. Superposition of *Efc*IBP (yellow) with the structures of *Col*AFP (red), *Tis*AFP6 (magenta), *Le*IBP (green), and IBPv (domain B, blue). Regions with high structural divergence are highlighted. The *Efc*IBP C-terminal 6His-tag has been omitted.

Further structural differences that characterize *Efc*IBP compared to IBP-1 fold proteins are located at the N- and C-terminal regions. In particular, the N-terminal extension Thr37-Thr45 is unique for *Efc*IBP, and it has an elongated structure that runs almost parallel to the β-strands of the C face, being anchored to the core of the protein through both polar and non-polar interactions with residues belonging to β8 (B face) and β10 (C face) (**Figs 1, 2 and 3**). In summary, the structure of *Efc*IBP appears to be more compact than homologous IBP-1 proteins, with the absence of the capping region between β5 and α1, and the B face more regular at its terminal filaments (β5 and β9) (**Figs. 2 nd 3**). Overall, *Efc*IBP is much more similar to the two-domain IBPv, where each IBPv domain also misses the capping region, than to other IBP-1 fold proteins.

Structural insights for IBS identification in *Efc*IBP

The identification of the *Efc*IBP ice binding site (IBS) was driven by previous studies on other IBP-1 fold proteins. Mutagenesis experiments and virtual docking to ice planes based on the crystal structures of *Col*AFP, *Ff*IBP, *Tis*AFP6, *Tis*AFP8, *Le*IBP and IBPv reveal that the IBS is located on the flattest surface of the β-helix (B face), while the other facs (A and C) are not involved in ice binding (**Fig. 2**) [71, 72, 95, 96, 106, 108]. These IBP-1 fold proteins typically lack regular ice-binding motifs, such as the Thr–X–Thr and the Thr–X–Asx repeats (X=any residue, Asx=Asn or Asp), typically found in insect and bacterial hyperactive IBPs [48, 153].

Furthermore, the B face of IBP-1 proteins is always quite hydrophobic, with polar residues being only between ~30% and 60% of the total solvent exposed residues. Indeed, the hydrophobic effect is thought to be a pivotal driving force when considering the general functional mechanism of IBPs, with restrained water molecules forming hydrogen-bond networks and producing 'cages' around hydrophobic groups, especially the methyl groups of Thr residues. Then, these anchored waters allow IBPs to bind ice by matching its specific plane(s). The organized solvation shell around the IBSs is involved in the initial recognition and binding of IBPs to ice by lowering the barrier for binding and consolidation of the protein-ice interaction surface [47, 123].

Despite the high structural homology with other IBP-1 fold proteins (**Figs. 2 and 3**), the *Efc*IBP residue distribution on the surface of the β-helix has different properties. A clear pattern of putative IBS repeats, three Thr–X–Thr and three Thr–X–Asx motifs, can be recognized in *Efc*IBP (**Figs. 2 and 4**). Interestingly, they are mostly located on the B face (on strands β2, β15 and β21), but some of them are also present on the C face (strands β10, and β13), in the connecting regions between β strands belonging to different faces (between β3 and β4, and between β18 and β19), and in the N-terminal extension (**Figs. 2 and 4)**. These observations suggest that not only the B face is involved in ice binding in *Efc*IBP.

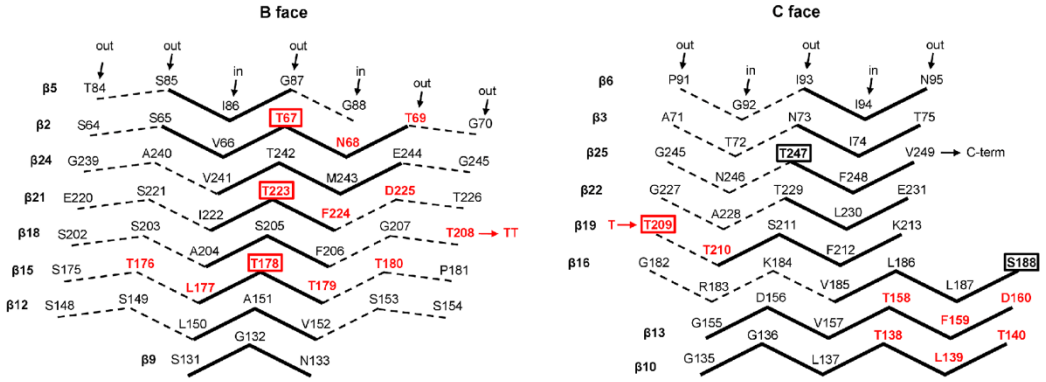

Figure 4. IBS at the B and C faces of *Efc*IBP. Schematic representation of the amino acid distribution on the (left) B face and on the (right) C face of *Efc*IBP. Residues belonging to the Thr–X–Thr and Thr–X–Asx IBS motifs are in red. Residues mutated to Tyr are squared. Solid lines indicate β strands, whose numbering is shown on the left side.

The B face of *Efc*IBP is formed mainly by seven parallel β-strands (β12, β15, β18, β21, β24, β2 and β5) composed of 3-5 residues, with a further minor contribution of the short β9 (**Fig. 4**). Three Thr–X–Thr and one Thr–X–Asx IBS motifs are homogenously distributed along the different parallel β-strands (β2, β15, β21) and converge to form a row of four Thr residues at the center of the B face, with the presence of an additional Ser in the middle and terminated by Ala and Gly residues (**Fig. 4**). This row is the most

repetitive organization in the *Efc*IBP structure and it might be responsible for much of the ice-binding capacity of the protein. On the other hand, the presence of several putative IBSs on the B face of *Efc*IBP decreases dramatically its hydrophobicity (73.6 % of the residues exposed to the solvent are polar) relative to other homologous IBP-1 fold proteins.

The *Efc*IBP C face is less flat and regularly organized than the B face (Fig. 4). However, as found for the B face, it contains putative Thr-rich IBS motifs and the residues pointing towards the solvent are mostly polar (80%). These structural features indicate that the B face is the most likely surface for ice binding, but suggest that the C face might be involved too. Furthermore, the low surface hydrophobicity coupled with the presence of IBS motifs might be the reason of the moderate, and not hyperactive, TH activity of *Efc*IBP.

Table 1. Data collection and structure refinement statistics

Data collection	
Spa**ce Group**	$P2_12_12_1$
a, b, c (Å)	45.48, 50.72, 92.45
α, β, γ (°)	90.0, 90.0, 90.0
Wavelength (Å)	0.82658
Resolution (Å)	46.23-0.84 (0.89-0.84)[a]
[b]R_{merge}	0.108 (0.577)
[c]R_{pim}	0.046 (0.360)
<I/σ(I)>	10.0 (1.8)
Completeness (%)	94.5 (68.8)
Redundancy	5.5 (3.1)
Refinement	
Resolution (Å)	46.226-0.840
Number of reflections	183713
[d]R_{work}/R_{free} (%)	11.5/12.8
Number of molecules	
Copies in the AU	1
Protein residues	223
Sulfate ions	4
Glycerol molecules	1
Water molecules	411
Average B factors (Å^2)	11.7
Rmsd	
Bond lengths (Å)	0.008
Bond angles (°)	1.17
Ramachandran plot statistics	96.3 % in favoured regions
	3.7 % in allowed regions
	0.0 % outliers

[a] Highest-resolution shell is shown in parentheses.

[b] $R_{merge} = \sum_{hkl} |I_{hkl} - < I_{hkl} > | / \sum_{hkl} I_{hkl}$

[c] $R_{pim} = \sum_{hkl} \sqrt{1/(n-1)} \sum_{j=1}^{n} |I_{hkl} - < I_{hkl} > | / \sum_{hkl} \sum_{j=1}^{n} I_{hkl,j}$

[d] $R_{work} = \sum_{hkl} |F_O - F_C| / \sum_{hkl} |F_O|$. R_{free} is calculated from 5% randomly selected data for cross-validation.

Interestingly, most of the residues potentially involved in ice binding (typically Thr and Ser) on the B and C faces are with side-chains in alternative conformations in our high resolution *Efc*IBP crystal structure (**Figs. 2 and 4**). This observation suggests that *Efc*IBP can reorganize the water molecules on its first hydration shell of both faces with high plasticity, thus reproducing the water molecule organization typically found on both the basal and prismatic planes of hexagonal ice crystals. In this respect,

however, the position and the spacing of crystallographic water molecules at the protein surface only partly match those typically found in ice crystal planes, due to the involvement in crystal contacts of both B and C faces, with consequent reorganization of the water molecules at the protein-protein interface.

Ice docking study

Molecular docking techniques were employed to get insights into the interactions of *Efc*IBP with ice. Despite the fact that many moderately active IBSs are known to bind to primary prism plane of ice crystal, but not to basal plane, we decided to test both planes as possible interaction partners of *Efc*IBP, and the surface complementarity (Sc) between the *Efc*IBP IBS and ice was evaluated to validate the docking [156]. As it is known that some hydration water molecules on the IBS are directly involved in binding to ice in certain IBPs [69, 123], a series of *Efc*IBP structures in which the crystallographic water molecules were gradually deleted (starting from those belonging to the most external water shell) was prepared and used for the docking study and Sc calculation. The resulting best docking poses (highest score in terms of steric and electrostatic correlations) indicated that *Efc*IBP binds both ice planes through the B face IBS with Sc values of 0.46 and 0.34 for basal and primary prism planes, respectively. Interestingly, the presence of few (26) crystallographic water molecules located in the troughs of the B face protein surface is sufficient to significantly improve the shape complementarity of this face with ice planes, with Sc values of 0.53 for basal plane and 0.39 for primary prism plane (**Fig. 5A, B**). Both these values are higher than 0.38, which was previously determined as a Sc threshold for IBPs [96, 153]. The interaction models were further validated by calculating the contact surface areas, which are 1390 Å^2 and 1163 Å^2 for basal and prism primary planes, respectively. These values are large and in line with those found for other IBPs of similar fold and size [72, 96, 106]. The B face residues directly interact with ice, with the hydration water molecules contributing to increase the shape complementarity with both ice basal and primary prism planes.

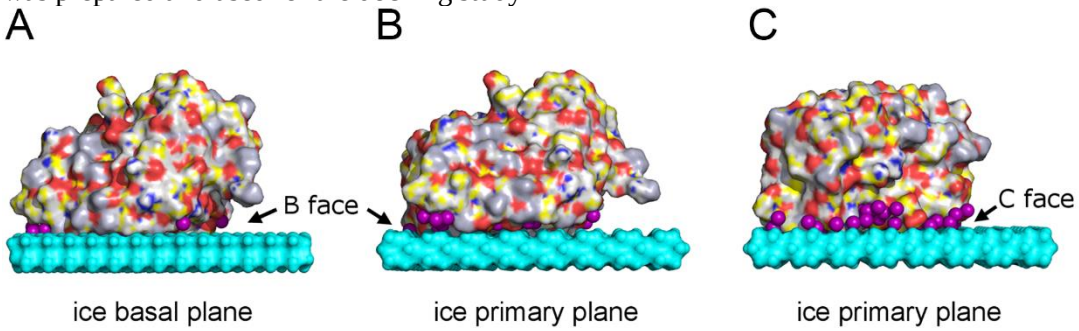

Figure 5. Docking of *Efc*IBP to ice planes. Interface between the B face of *Efc*IBP and **ice** (A) basal and (B) primary prism planes. (C) Interface between the C face of *Efc*IBP and the ice primary prism plane. Residues are colored in yellow for carbon, red for oxygen, blue for nitrogen, green for sulfur and gray for hydrogens**.** Bound crystallographic water molecules are colored in magenta, ice molecules in cyan.

Surprisingly, the docking simulations indicate that the primary prism plane of ice, but not the basal plane, can be bound also by the *Efc*IBP C face, with a Sc value of 0.31 which increases to 0.40 if some (61) water molecules are used in the calculation (**Fig. 5C**). In this scenario, the included crystallographic water molecules compensate for the flatness distortions of the protein C face induced by the presence of filaments β13 and β16 (**Fig. 1**). The contact surface area between the protein C face and

the prism primary plane is 1265 Å^2 and the majority of the ice-protein contacts are water-mediated.

Site-directed mutagenesis of *Efc*IBP IBS residues

In order to investigate which part of the *Efc*IBP surface is involved in ice binding, we designed and expressed a series of single point mutants and evaluated their TH and IRI activities. Based on structural and docking analyses we focused on the putative IBS located on the B and C faces of the protein. The selected B face residues (T67, T178 and T223) belong to three Thr–X–Thr and Thr–X–Asx motifs and are centered on the B face (**Figs. 4 and 6**). The C face mutations involve residues S188, T209 and T247. T247 was selected because it is located at the center of the C face, while T209 is of interest since it is part of a Thr–X–Thr motif laterally located on the C face (**Figs. 4 and 6**). In order to check if the divergent region β10-β13-β16 forms an IBS, S188 was also substituted. This residue is located on β16, adjacent to the Thr–X–Thr and Thr–X–Asx motifs of strands β10 and β13. Yet β10 and β13 are less solvent exposed and, therefore, less likely to take part in ice binding. The selected residues were replaced by Tyr, a bulky residue that would disrupt the flatness of the protein surface and hinder the ability of the protein to bind ice in case it is located on the IBS [72, 95, 96].

All mutants were produced in Zym-5052 medium and purified at high yield (~2 mg from 1L of culture). The degree of purification was comparable to the wt *Efc*IBP. The circular dichroism (CD) spectra of *Efc*IBP variants, except T247Y mutant, were highly similar to those of the wt (**Fig. 7A and B**), indicating that substitutions did not affect the protein secondary structure. The spectra showed a minimum ellipticity at approximately 219 nm and positive ellipticity at ~195 nm, which are characteristic of β sheet-rich proteins. In the case of T247Y mutant, the overall CD spectrum was similar to that of the wt, indicating that the protein retained its fold. However, the minimum ellipticity was shifted to 217 nm and the amplitude was slightly lower relative to the other mutants and to the wt (purple line in **Fig. 7B**). These minor changes possibly indicate a slight decrease in β structure. It should be noted that the T247Y mutation site is located very close to the C-terminus of the protein (Leu253), where the 6His-tag tail is present (**Fig. 6**). A reorientation of this C-terminal tail, due to the T247Y mutation, might partly disturb the N-terminal region of the protein (on the A face) located in front of it, where the protein backbone has an extended β-like structure (**Fig. 1**).

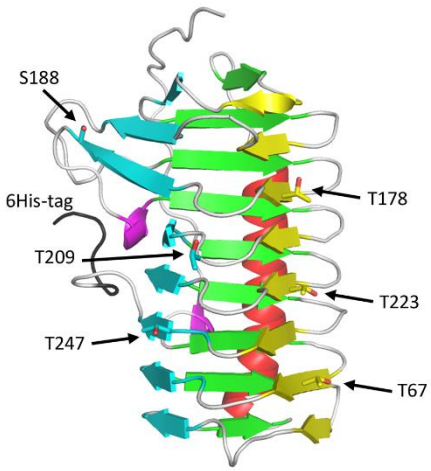

Figure 6. *Efc*IBP mutation sites. Mutated residues on the B (yellow) and C (cyan) faces of the *Efc*IBP structure are shown as sticks and indicated by arrows and labels. The C-terminal 6His-tag is shown in black

Still, the experimental evidence that the thermal stability of the protein remains similar to the wt in all mutants, including the T247Y variant (**Fig. 7C, D**), indicates that the Tyr substitutions did not alter the β-helix structure in the core of the protein, which remains compact and stable. .

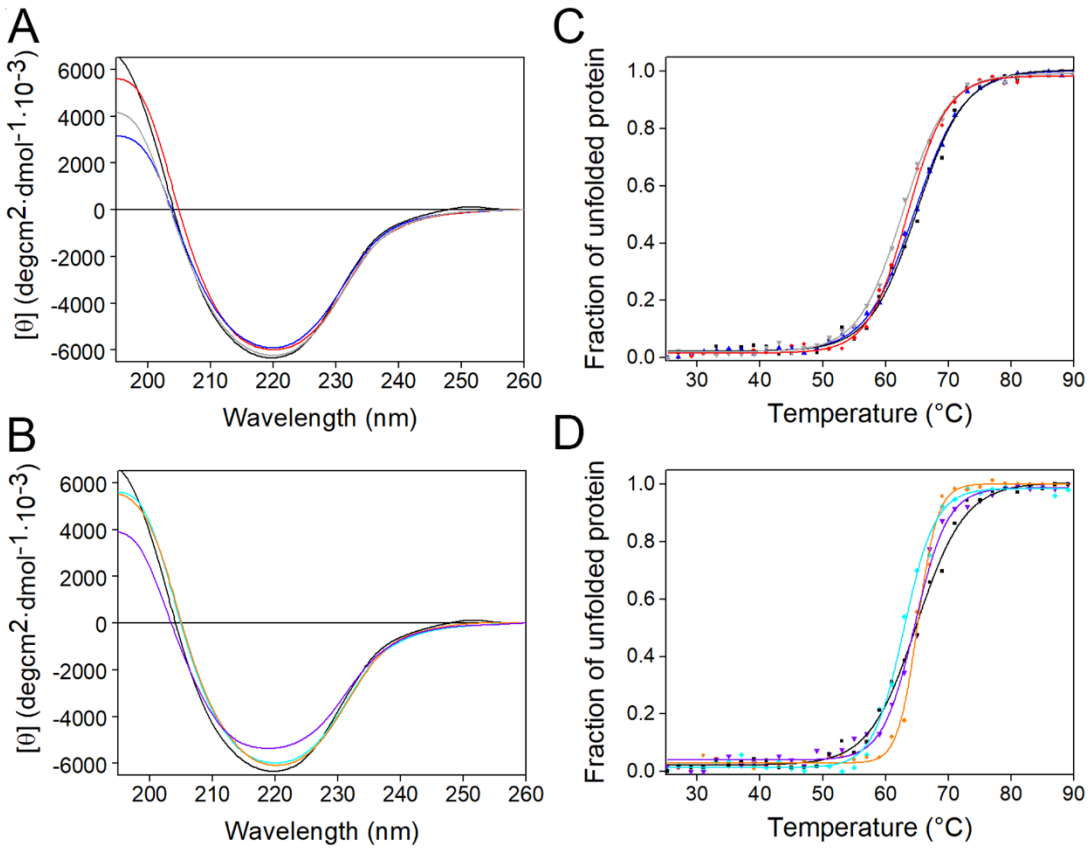

Figure 7. Far-UV CD spectra of *Efc*IBP and its mutants. CD spectra (A) and denaturation profile (C) of face B mutants: in black wt *Efc*IBP, in red T67Y, in blue T178Y, in grey T223Y. CD spectra (B) and denaturation profile (D) of face C mutants: in black wt *Efc*IBP, in cyan S188Y, in orange T209Y and in purple T247Y.

Activity measurements of *Efc*IBP mutants

Following our findings that amino acid substitutions do not disrupt the protein folding neither affect its stability, and with the aim to determine the IBS of *Efc*IBP, we measured the TH activity of the mutants. **Figure 8** shows the TH of all variants in comparison to the wt protein. All B face mutants show TH levels of 10-30% of the wt TH in equivalent protein concentrations. On the C face, S188Y retains 50-60% of activity, indicating that the β10-β13-β16 region is not the major part of the IBS. Instead, T209Y retains only 30% activity, while T247Y is barely active, with no activity at 10 μM and 4-5% activity at higher concentrations. Therefore, our TH measurements on *Efc*IBP mutants indicate the B face as the major IBS (including the Thr–X–Thr and Thr–X–Asx motifs), and the C face also partly involved in ice binding, in agreement with the docking simulations.

We measured the IRI activity of the *Efc*IBP mutants in order to obtain more information on the location of the IBS and the effects of the surface-exposed positions on ice binding (**Fig. 9**). All mutants show low IRI activity at a concentration of 0.02 μM, reducing the recrystallization rate in the range of 0-50% compared to no IBP, with T247Y having no IRI activity. At a higher concentration, 0.1 μM, the IRI activity of all mutants, including T247Y, is more pronounced, in the range 30-95% reduction of the recrystallization rate. In both concentrations, the *wt* reduced the recrystallization rate by 100%. This supports the TH and docking results, suggesting that

*Efc*IBP interacts with ice through both B and C faces. It is likely that each face is responsible for binding of *Efc*IBP to specific sites or planes of ice. Another such case was demonstrated in a study of isoforms of type III AFP from ocean pout. The authors showed by single point mutations that the IBS of the protein is composed of two adjacent surfaces, each responsible for binding to different ice planes [32].

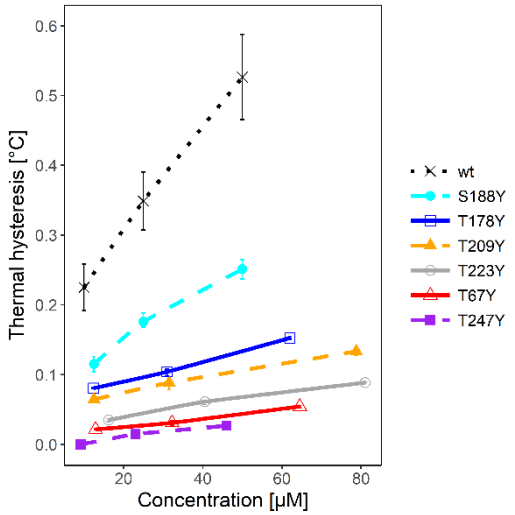

Figure 8. TH activity of *Efc*IBP and mutants. The TH activity as a function of protein concentration is presented for the wt protein (black dotted line), the B face mutants (solid lines, empty markers) and the C face mutants (dashed lines, filled markers). Each point presents the average of three independent measurements, with standard deviations.

A puzzling finding is that there is no obvious correlation between the effects of the mutations on TH and their effects on IRI. Since both IRI and TH depend on the ice binding properties of the proteins [15,33], one would expect the mutants with high TH to have also high IRI. Such a correlation was shown in a study of a series of mutants of the ryegrass IBP [33]. In the case of *Efc*IBP mutants, each mutation most probably affected the binding rates of the protein to particular ice planes in a different manner. It is possible that binding to certain ice planes is more crucial for IRI and less for TH, or vice versa. Furthermore, each face requires appropriate water organization for ice binding and reacts differently to surface perturbations. In particular, the S188Y mutant had the highest TH activity among the mutants (49% of the wt), and the lowest IRI activity (only 25% or 52% reduction of recrystallization rate at 0.02 μM and 0.1 μM concentrations, respectively) after T247Y. One explanation for this effect is that the Tyr introduced into strand β16 induces local organization of water molecules that disrupted binding to a certain ice plane important for IRI more than for TH. Yet this and any other explanation are highly speculative at this stage. While *Efc*IBP presents a non-trivial case of ice recognition, all our findings so far point out that the protein has a compound IBS that involves both the B and the C face with yet unknown specificities.

To summarize, the structural analysis of *Efc*IBP provided new insight into its functional features. The *Efc*IBP tertiary structure consists of a right-handed b-helix which conforms to the IBP-1 fold with some important differences. *Efc*IBP misses the cap subdomain between b5 and a1, typically present in many IBP-1 fold protein. Considering that *Efc*IBP is very stable to heat, with a Tm of 66.4 °C [18], the proposed role of the cap subdomain in the overall stability of IBP [106] seem to be scaled down. This conclusion is further supported by the structure of the recently published two-domain protein IBPv [108], where each β-helix domain misses the cap subdomain but the protein has a Tm of 53.5 °C [97], similar to that of capped IBP-1 fold proteins [71, 72, 95, 96, 106]. Overall, the low hydrophobicity of B and C faces might explain the only moderate TH activity of the protein.

Docking simulation and mutational studies indicate that the *Efc*IBP has a compound IBS that consists of both the B and the C faces. In fact, most mutations on both faces heavily affect TH and IRI activities of the IBP. In some instances, the two effects appear to be fully or partly uncoupled. Although only a

few amino acids have been changed, it emerges that TH and IRI depend at least partly on different features of the binding sites. To date, studies about the correlation of TH and IRI in IBPs are still too scarce to allow drawing general conclusions. However, a recent study showed that also in LeIBP TH and IRI are not necessarily coupled, in fact also in this case a single mutation increases the IRI without affecting the TH [155]. This information calls for further studies aimed at a deeper understanding of IRI, especially in view of developing IBP-based methods for cryoprotection.

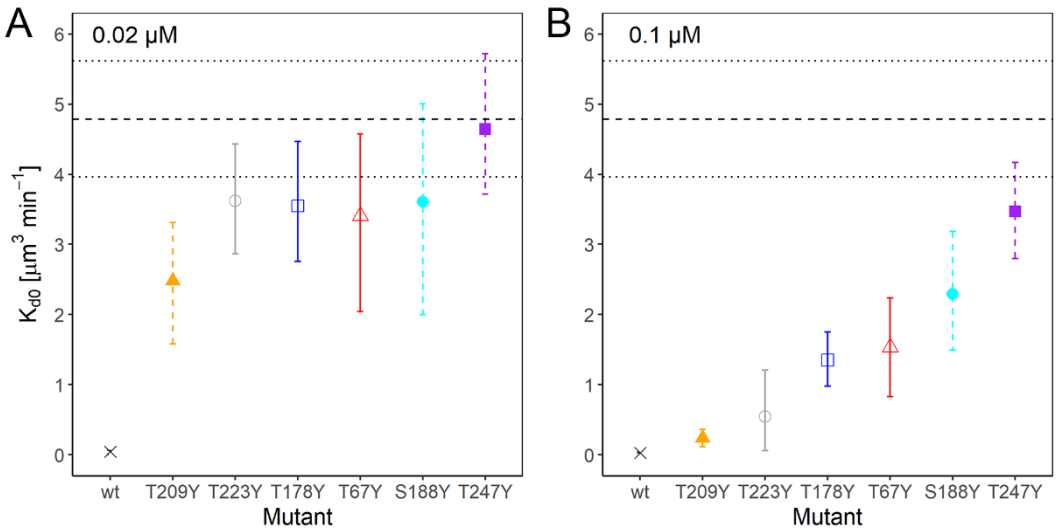

Figure 9. Ice recrystallization efficacy of *Efc*IBP mutants and wt protein. Quantitative analyses of sucrose sandwich assays were performed at concentrations of A) 0.02 µM and B) 0.1 µM. K_{d0} represent the recrystallization rates. Vertical lines are 95% confidence intervals (n = 5). Horizontal dashed and dotted lines represent mean and 95% confidence interval for recrystallization constant of sucrose buffer without protein. Colors and shape codes are the same as in figure 8.

Materials and Methods

Strain and materials

Escherichia coli strain DH5α™ (Invitrogen, Waltham, USA) was used for plasmid amplification, while BL21 (DE3) (EMD Millipore, Billerica, USA) was used as the host strain for heterologous expression. Oligonucleotides are from Metabion (Metabion International, Planegg, AG) and Q5® High-Fidelity DNA Polymerase is from New England Biolabs (New England Biolabs, Ipswich, MA).

Cloning and mutagenesis

pET-21a [*Efc*IBP] was described in a previous work [93]. The recombinant protein carries a 6His tag at the C-terminus. Mutagenesis of *Efc*IBP was carried out by QuickChange® PCR. The forward and reverse primers are described in Table 2. Reactions were carried out using Q5® High-Fidelity DNA Polymerase and Eppendorf Master-cycler (Eppendorf, Hamburg, Germany) under the following conditions: 1 cycle (98 °C for 2 min), 25 cycles (98 °C for 10 s, annealing temperature for 25 s and 72 °C for 180 s), and a final cycle at 72 °C for 3 min. The annealing temperatures (T_A) used for each PCR reaction are indicated in Table 2. Mutations were verified by DNA bidirectional DNA sequencing.

Production and purification of recombinant proteins

Recombinant 6His-tagged proteins were produced in Zym-5052 medium [132] and purified from the soluble fraction of cell extracts by affinity chromatography as

described previously [93]. Samples containing highest protein concentrations were pooled and buffer exchanged to 10 mM ammonium acetate (pH 7.0) by gel filtration using a PD10 column (GE Healthcare, Little Chalfont, UK). Purified proteins were lyophilized and stored at -20 °C. Protein concentration was determined by the Bradford protein assay (Bio-Rad, Hercules, USA), using bovine serum albumin as the standard.

Table 2. Primer sequences utilized for generation of *Efc*IBP variants. The mutation sites are underlined.

Primer ID	Sequence	Length	T_A (°C)
T67Y Forward	5' ACCAACATTACCGGAGATCTGGGC 3'	24	66.9
T67Y Reverse	5' CGCACCAGTGTTGTAAACAGAAGAAC 3'	26	66.2
T179Y Forward	5' CGCAAGGTGCTGCTGAGCGGT 3'	21	67.3
T179Y Reverse	5' ACCCGGTGTGGTGTACAGGGTAG 3'	23	68.3
T223Y Forward	5' CTGGAATCTATCTACTTCGATACCGGC 3'	27	68.2
T223Y Reverse	5' TGCGATCACGGTACCTTTGAAAGAGG 3'	26	67.9
S188Y Forward	5' GTGCTGCTGTACGGTGGTGCGCTG 3'	24	67.0
S188Y Reverse	5' CTTGCGACCTGGGGTGGTGGTCAG 3'	24	67.0
T209Y Forward	5' TTTAAAGGAACCGTGATGCA 3'	21	63.0
T209Y Reverse	5' AGAGGTAGTATAACCGAAAGACGC 3'	24	65.0
T247Y Forward	5' TTTGTTCTGCCGCTAGAGCACCACCAC 3'	27	74.0
T247Y Reverse	5' GGTGTTACCTCCATGTACACTGCGCC 3'	27	74.0

Crystallization, structure determination and refinement

Crystallization trials of *Efc*IBP (5 mg mL^{-1} in pure water) were performed with vapor diffusion techniques (sitting drop) using an Oryx-8 crystallization robot (Douglas Instruments, East Garston, UK). Already after one day crystals were observed under several growth conditions, both at 4 °C and at 20 °C. The best crystals were obtained with the precipitant solution 2.2 M $(NH_4)_2SO_4$, 0.1 M HEPES buffer (pH 7.5), at 20 °C. Crystals were cryoprotected in their mother liquor, supplemented with 25% glycerol and flash-frozen in liquid nitrogen. *Efc*IBP crystals diffracted up to 0.84 Å resolution with space group $P2_12_12_1$ and one protein molecule in the asymmetric unit (Matthews coefficient 2.12 $Å^3$ Da^{-1}, estimated solvent content 42%). Diffraction data were collected at the ID-29 beamline of the European Synchrotron Radiation Facility (ESRF, Grenoble, France) and processed with XDS [157] and SCALA [158]. Data reduction statistics are reported in Table 1. The *Efc*IBP crystal structure was solved by molecular replacement using Phaser [159], with the *Col*AFP structure (PDB code: 3WP9) [96] as a search model (36% sequence identity with *Efc*IBP). The *Efc*IBP sequence was then model-built into the electron density using Coot [160] and restrained-refined with H atoms and anisotropic B-factors using Refmac5 [161] and Phenix [162]. All refinement statistics are reported in detail in Table 1. The stereochemical quality of the model was assessed using MolProbity [163].

Docking modelling to ice

Docked model for *Efc*IBP (without the C-terminal 6His tag) and ice planes with the minimum overall docking score was searched with the program HEX 8.0.0 [164], using default parameters except for correlation type (shape + electrostatics). The

shape complementarities of the IBP–ice interfaces for the resulting models were evaluated using the SC program [156].

Circular dichroism spectroscopy

Lyophilized proteins were suspended in 25 mM phosphate buffer (pH 7.0) to a concentration of 8 µM. CD spectra were measured using a J-815 spectropolarimeter (Jasco Corp., Easton, MD, USA) in 1 mm path-length cuvette as described [165]. In experiments aimed to assess thermal stability spectra were collected by measuring the CD signal at 215 nm fixed wavelength, and the sample was progressively heated from 25 to 90 °C. Measurements were performed with a data pitch of 2 °C and a temperature slope of 0.5 °C/min. Experiments were performed in triplicate.

Thermal hysteresis

Protein samples were prepared by dissolving lyophilized proteins in 20 mM ammonium bicarbonate buffer (pH 8.5) and diluting them to the desired concentration in the same buffer. TH measurements were performed using a custom nanoliter osmometer as described previously [14]. Single crystals of typically 10 µm diameter were obtained and incubated for 1 min slightly below their melting temperature. Then the temperature was dropped at a cooling rate of 0.01 ºC every 4 s. The freezing point was determined as the temperature at which the crystal grew continuously. Each measurement was repeated at least three independent times.

Ice recrystallization inhibition

IRI activity was measured by a sucrose-sandwich assay [147] with some modifications [24]. The sample solutions contained 45% sucrose, 50 mM NaCl, 10 mM Tris buffer (pH 8.0) and 0 or 0.02 µM or 0.1 µM of protein. Samples of 1.4 µL were placed on a sapphire sample holder and covered with a 13-mm diameter circular glass coverslip. The sample was sealed with type B immersion oil (Sigma-Aldrich, St. Louis, MO, USA) to avoid evaporation and mounted on a copper plate with a 2.5-mm diameter slit placed on the stage of the nanoliter osmometer [14]. The sample was cooled from room temperature to -35 °C by the Peltier element of the nanoliter osmometer while slowly pouring liquid nitrogen on top of the sample. Fast rate of cooling was necessary to form polycrystalline ice. The temperature was then elevated to -10 °C at a warming rate of 150 °C·min^{-1} and then warming continued to -8 °C at a rate of 6 °C·min^{-1}. The final stage of heating up to the annealing temperature of -7.4 °C was conducted at a slow rate of 1 °C·min^{-1} to avoid overheating. The sample was maintained at this temperature for 60 min. During this period, recrystallization was recorded using a Basler ace acA1920-155um camera (Basler, Germany) every 10 s. The experiment was repeated at least five times for each concentration.

The IRI was quantified following the mathematical description derived by Budke et al. [24]. The images were processed using Fiji software [166] to calculate the mean radius of the crystals and the total crystal volume. The cube of the mean crystal radius was calculated and plotted against time. The slope of the curve obtained from time points 30-60 min was taken as the recrystallization rate constant (K_d). The average ice volume fraction of this period was used to extrapolate K_d constant to zero ice fraction (K_{d0}), as described by Budke et al. [24]. In all experiments, the ice volume fraction was less than 10%.

Statistical analysis and plotting were performed using R 3.4.3 (R Foundation for Statistical Computing, Vienna, Austria). Mean values and 95% confidence intervals were calculated by nonparametric bootstrapping method from R package 'Hmisc' 4.0-3 using 1000 resamples.

ACKNOWLEDGMENTS

We thank Daniele de Sanctis for data collection support at the ID29 beamline of the European Synchrotron Radiation Facility (ESRF, Grenoble, France). This work was

partly supported by a grant Progetto Nazionale di Ricerche in Antartide PEA 2014-2016 and the RISE-MSCA Project "Metable" to M.L. I.B. acknowledges support by European Research Council (grant No. 281595) and by Israel Science Foundation (grant No. 930/16). A.K. acknowledges support by European Regional Development Fund.

AUTHOR CONTRIBUTIONS

Biochemical and biophysical experiments on the native and mutant proteins were performed by M. Mangiagalli (protein expression and purification, CD), A. Kaleda and G. Sarusi (IRI and TH); V. Nardone, V.F. Vena and M. Nardini grew the protein crystals, collected the diffraction data and solved the structure of the protein; M. Nardini performed the *in silico* docking experiments; M. Bar Dolev and I. Braslavsky designed and analyzed the activity measurements; M. Lotti, I. Braslavsky and M. Nardini conceived the project; M. Bar Dolev, M. Nardini and M. Lotti wrote the paper. All authors have read and approved the manuscript.

Database

Coordinates and structure factors have been deposited in the Protein Data Bank under accession number **6EIO**.

Saturn-shaped ice burst pattern and fast basal binding of an ice-binding protein from an Antarctic bacterial consortium

Aleksei Kaleda[1,2#], Lotem Haleva[1#], Guy Sarusi[1#], Tova Pinsky[1#], Marco Mangiagalli[3], Maya Bar Dolev[1], Marina Lotti[3], Marco Nardini[4] and Ido Braslavsky[1*]

[1] Institute of Biochemistry, Food Science and Nutrition, The Robert H. Smith Faculty of Agriculture, Food and Environment, The Hebrew University of Jerusalem, 7610001 Rehovot, Israel; [2]Department of Chemistry and Biotechnology, School of Science, Tallinn University of Technology, Ehitajate tee 5, 19086 Tallinn, Estonia; [3]Department of Biotechnology and Biosciences, University of Milano-Bicocca, Piazza della Scienza 2, 20126 Milan, Italy; [4]Department of Biosciences, University of Milano, Via Celoria 26, 20133 Milan, Italy

* corresponding author

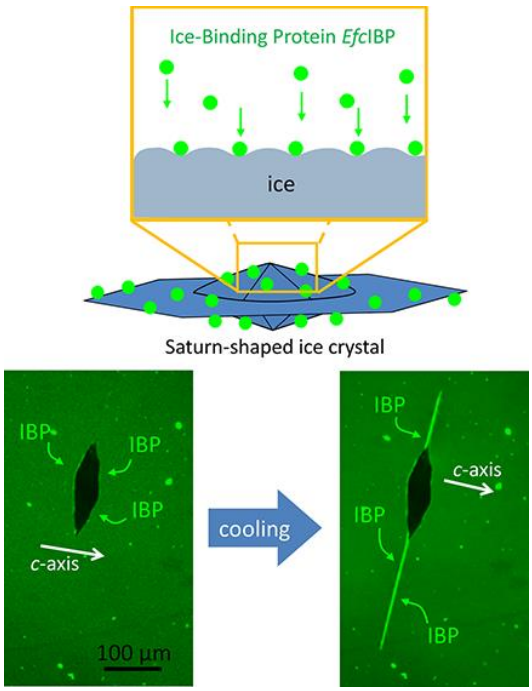

Keywords: ice-binding protein, binding kinetics, FIPA, ice crystal shape, *Efc*IBP, antifreeze protein.

Langmuir (2018)
DOI: 10.1021/acs.langmuir.8b01914

ABSTRACT: Ice-binding proteins (IBPs) bind to ice crystals and control their growth, enabling host organisms to adapt to subzero temperatures. By binding to ice, IBPs can affect the shape and recrystallization of ice crystals. The shapes of ice crystals produced by IBPs vary and are partially due to which ice planes the IBPs are bound to. Previously, we have described a bacterial IBP found in the metagenome of the symbionts of *Euplotes focardii* (*Efc*IBP). *Efc*IBP shows remarkable ice recrystallization inhibition activity. As recrystallization inhibition of IBPs and other materials are important to the cryopreservation of cells and tissues, we speculate that the *Efc*IBP can play a future role as an ice recrystallization inhibitor in cryopreservation applications. Here we show that *Efc*IBP results in a Saturn-shaped ice burst pattern, which may be due to the unique ice-plane affinity of the protein that we elucidated using the fluorescent-based ice-plane affinity analysis. *Efc*IBP binds to ice at a speed similar to that of other moderate IBPs (5 ± 2 mM^{-1} s^{-1}); however, it is unique in that it binds to the basal and previously unobserved pyramidal near-basal planes, while other moderate IBPs typically bind to the prism and pyramidal planes and not basal or near basal planes. These insights into *Efc*IBP allow a better understanding of the recrystallization inhibition for this unique protein.

Abbreviations

AFP, Antifreeze Protein; **BSA**, bovine serum albumin; **FIPA**, Fluorescent-based Ice-Plane Affinity; **IBP**, Ice-Binding Protein; **IRI**, Ice Recrystallization Inhibition; **MCF**, microfluidic cold finger; **SC**, shape complementarity; **TH**, thermal hysteresis; **wt**, wild type.

Introduction

A key strategy of cold-adapted organisms that need to survive at low temperatures is the production of ice-binding proteins (IBPs). The general concept shared by all IBPs, as implied by their name, is the ability to directly adhere to ice crystals, thereby affecting different aspects of ice growth. IBPs have been identified and characterized in many organisms spanning different branches of the tree of life, including fish, terrestrial arthropods, plants, fungi, bacteria and diatoms [6].

IBPs in freeze-avoidant organisms are thought to act by depressing the growth of ice crystals in supercooled solutions, thus are also known as antifreeze proteins (AFPs). Freezing point depression below the melting point is termed thermal hysteresis (TH) [6]. AFPs have typically been classified into hyperactive and moderate AFPs, where moderate AFPs have TH up to 1°C at millimolar concentrations while hyperactive AFPs produce higher TH in micromolar concentrations [15, 167]. In freeze tolerant organisms IBPs act as ice recrystallization inhibition (IRI) proteins, which can help to avoid damage caused by freezing [18]. Research into bacterial and algal communities found at ice water interfaces led to the notion that the role of bacterial IBPs may be to sustain a liquid environment and prevent the freezing of brine pockets. This idea is supported by the fact that many of these IBPs are secreted to the environment surrounding the organism [58, 100]. Extracellular IBPs contain a conserved region initially classified in the Pfam database (http://pfam.xfam.org/) as "domain of unknown function" (DUF) 3494, and most of them carry a signal peptide for secretion at their amino terminus.

Euplotes focardii, a free-swimming psychrophilic ciliate from Terra Nova Bay in Antarctica lives in symbiosis with bacteria. Metagenome analysis of the symbionts of *E. focardii* revealed a coding sequence for a bacterial ice-binding protein (*Efc*IBP) [117]. This protein contains a DUF3494 domain and an N-terminal signal sequence for protein transport. The protein is folded in a right-handed β-helix with a triangular cross-section formed by three parallel β-sheets,

named A, B, and C faces, and an additional single α-helix aligned along the axis of the β-helix [118]. This fold is typical of bacterial IBPs, where it is defined as the IBP-1 fold [6]. However, *Efc*IBP has a shorter β-solenoid, and the sequence and organization of the regions exposed to ice are also different from its homologs.

*Efc*IBP has a peculiar combination of TH and IRI activity. Its TH is 0.53 °C at 50 µM, which is classified as a moderately active, but ice recrystallization 50% inhibition concentration is 2.5 nM, making it one of the most potent IRI agents described in literature to date [93]. This attribute of *Efc*IBP makes it a candidate as an efficient recrystallization inhibition factor in cryobiology applications.

Ice growth inhibition mechanisms of hyperactive and moderate IBPs are not yet fully understood, and no comprehensive model that integrates different attributes of various IBPs exists to date. Drori *et al*. [35] stated that the key property that delineates moderate and hyperactive IBPs is the ability of hyperactive to bind the basal ice plane, in addition to prismatic and pyramidal. However, moderate IBP from *Leucosporidium* sp. AY30 (*Le*IBP) is known to have low TH (0.2 °C at 50 µM), but binds to the basal plane [168]. More exceptions to this rule are *Lp*IBP from *Lolium perenne* [54], *Fc*IBP (isoform 11) from *Fragilariopsis cylindrus* [109] and *Efc*IBP, as discussed further in this paper.

Docking simulations demonstrated that both B and C faces of the protein employ water molecules to increase ice-binding site shape complementarity with an ice lattice, which is especially necessary for the non-flat C face of the protein. According to the simulations [118], B face has a good shape complementarity (SC) to the basal plane (SC 0.53) and low for the primary prismatic plane (SC 0.39), and C face has weak complementarity to the primary prismatic plane (SC 0.40). These SC values are higher than 0.38, which is considered a threshold for IBP [96] and was previously used in *Efc*IBP docking study [118].

Based on structural and simulated ice docking analyses, six mutants were designed with amino acid replacements on the putative ice-binding sites located on the B and C faces of the *Efc*IBP. TH and IRI analyses of B face mutants, and C face mutants confirmed that both faces are vital for activity, as these mutants had significantly reduced TH and IRI. However, no clear distinction of which face is more important was found [118].

Kinetics of IBP adsorption to ice have previously been studied, as have the ice surface affinity by moderate and hyperactive IBPs [33, 169-173]. Thermal hysteresis activity of hyperactive IBPs can increase up to 40 times with a longer incubation period, whereas incubation time only slightly affects moderate IBP TH activity [33, 174]. This was attributed to finding that some hyperactive IBPs adsorb slowly to the basal plane, reaching saturation only after more than one hour. In contrast, moderate IBPs were demonstrated to adsorb to the prism plane rapidly [33].

In a solution where IBPs are not present, ice crystals grow in a circular disc shape [175]. When cooled below the melting point, ice crystals in moderate IBP solutions (such as type I-III AFP) form hexagonal bipyramid or trapezohedron shapes elongated in the direction of the *c*-axis. This growth along the *c*-axis proceeds continuously with diminishing size of the basal planes until the basal planes are almost eliminated, and the bipyramidal tips are formed. The bipyramidal crystal with the two tips is then stable until the freezing point is reached and the crystal bursts in the *c*-axis direction. In contrast, ice crystals in hyperactive IBP solutions, such as sbwAFP from spruce budworm, form bipyramidal or lemon shapes during melting and stay in a constant size and shape in the TH gap and burst in *a*-axis direction [15, 29].

Ice crystal morphology and burst behaviour induced by ice-binding proteins are closely related to the crystal planes which they bind. Recently an article describing moderate

*Fc*IBP11, a member of the DUF3494 family [109], demonstrated that basal binding affinity does not confer hyperactivity. In this article we expand on the topic of basal-binding moderate IBPs, and show that *Efc*IBP, a moderately active IBP from the DUF3494 family, binds to the basal and previously unobserved pyramidal planes at a rate comparable to other moderate IBPs. This causes growth and burst in the *a*-axis direction, which leads to peculiar Saturn-shaped ice crystals.

Results

*Efc*IBP is a unique IBP which has been shown to have high IRI, moderate TH activity, and two faces of binding [93, 118]. Here we describe several phenomena where *Efc*IBP displays uncommon ice shaping, binding kinetics, and binding plane affinity. In this section, we provide details about the different aspects and characteristics of the *Efc*IBP.

Ice crystals in the wild type *Efc*IBP solution

The unique effect of *Efc*IBP can first be noted in its effect on ice crystal shaping. Ice crystal shape of the wild type (wt) *Efc*IBP appears at the beginning of crystal growth as a wide hexagonal truncated trapezohedron (**Fig. 1A**), a model for which is presented in **Figure 1B**. When the temperature of *Efc*IBP solution is lowered at a constant rate, ice crystals grow in small sharp steps in the *a*-axis direction, which was identified by the observed six-fold crystal symmetry. Crystals grow, then stabilize and grow again, until a smoothed obtuse-angled bipyramidal crystal is formed (**Fig. 2 A-F and Movie S1**).
When this growth is observed normal to the *c*-axis, it resembles a bipyramidal growth in *c* direction that is commonly attributed to moderate IBPs (**Fig. 2 D, E**). However, it should be stressed that in the case of *Efc*IBP ice is not a bipyramid pointing in *c* axis, rather a thin disc-shaped crystal which is longer in the *a* direction (with *c* to *a*-axis ratio 1:4.5). In other words, unlike ice crystals of other IBPs that grow into thin bipyramids until basal planes are eliminated, in the presence of *Efc*IBP ice crystals grow wider until prism planes are minimized.

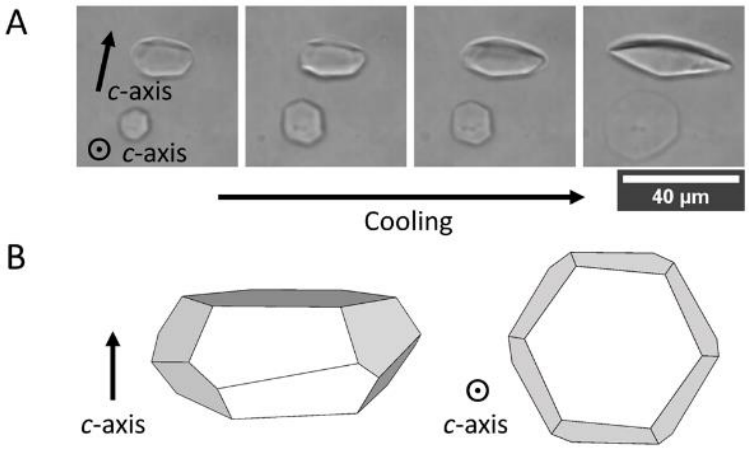

Figure 1. A) Ice crystal shapes and their growth pattern during cooling in 5 µM solution of wt *Efc*IBP. B) Simplified model of the wt *Efc*IBP ice crystal. The circled dot indicates *c*-axis normal to the image plane.

*Efc*IBP has a unique burst behavior. Ice crystals obtained in the presence of *Efc*IBP have a biconvex shape. Upon continuous cooling, the burst happens as a rapid growth of a thin disc protruding from the edge of the crystal (**Fig. 2 G, H**). Note that **Figure 2G** offers a lateral view of the disc, observable as a line in the middle of the crystal. This supports that the burst pattern is in the *a* direction. Coherent with this interpretation,

the bursting produces a circular disc when observed along the crystal *c*-axis. This behavior was observed consistently dozens of times; more examples are in **Figure S1**. A simplified model of such burst is shown in **Figure S2**. This shape suggests that the crystal is blocked on the basal plane and not on the prism plane.

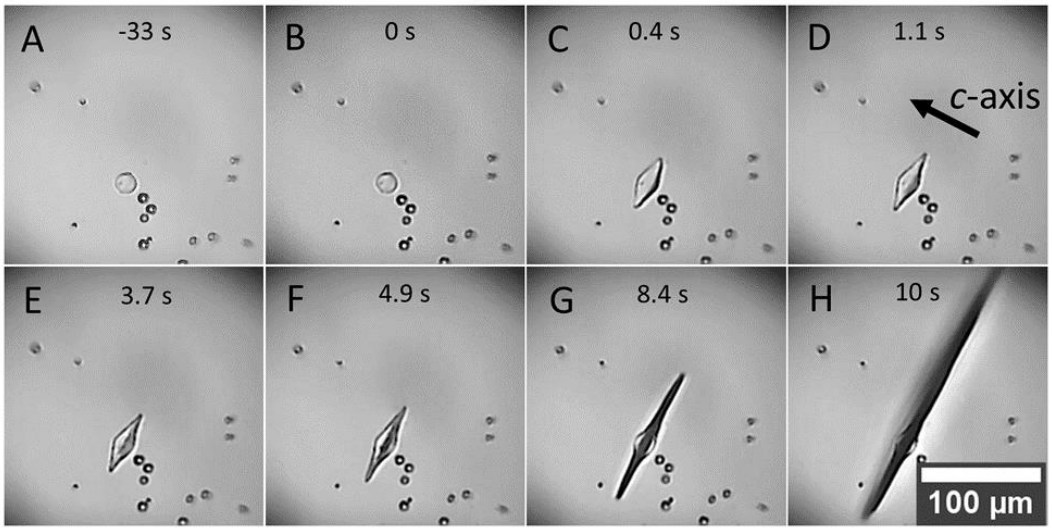

Figure 2. Selected video frames of ice crystal growth (A-F) and burst pattern (G-H) in wt *Efc*IBP 5 µM solution during cooling. Time from the beginning of growth is shown. The burst starts at 7.5 s. The full experiment can be seen in Movie S1.

Homologue IBPs from DUF3494 family *Col*AFP from *Colwellia sp*. strain SLW05 [96], *Ff*IBP from *Flavobacterium frigoris* PS1 [106], *Sf*IBP_1 from *Shewanella frigidimarina* [94], *Le*IBP [71], and *Tis*AFP from *Typhula ishikariensis* [176] produce different crystal shapes. The most similar shape is produced by *L*eIBP, although it forms hexagonal truncated trapezohedron shape that is narrower and elongated along the *c*-axis (*c*:*a* ratio 2.4:1). When the burst pattern is compared to other DUF3494 IBPs we note a difference from *Sf*IBP_1 [94], *Ff*IBP [71], and *Col*AFP [177], which burst dendritically in the *a*-axis direction, as is common for hyperactive proteins [29]. The non-dendritic burst pattern of the wt *Efc*IBP might be explained by the fact that it is a moderately active IBP and the supercooling of the solution is to a lesser degree than that of the hyperactive proteins, thus dendritic growth does not occur.

To further investigate ice crystal plane affinity of this protein, we produced GFP-*Efc*IBP and used the FIPA assay and other fluorescent microscopy methods. The fusion of GFP with the protein did not change the ice crystal shape or its burst behavior (**Fig. S1**). However, the TH of GFP-*Efc*IBP is somewhat lower than that of the wild type (by 35%, **Figure S3**), although there is no distinct effect of incubation time on TH for both proteins. In many cases, the fusion of GFP with AFP, such as type III AFP [178] or sbwAFP [170] does not negatively affect the TH of the sample. In fact, the addition of GFP tends to raise the TH. The negative effect seen here is likely due to some shielding of the ice-binding sites by GFP. The cause of the lowered TH likely does not significantly affect the results presented further, as the ice shaping and burst behavior of GFP-*Efc*IBP are not different.

Ice plane affinity of GFP-*Efc*IBP

Fluorescence-based ice plane affinity analysis of GFP-*Efc*IBP demonstrated an intricate roughly triangular binding pattern (**Fig. 3**). GFP-*Efc*IBP has a general weak affinity towards most pyramidal plane

angles (most of the hemisphere between the basal and prism planes is covered), with two sets of distinct small spots of higher affinity. The first is at a very low angle to the basal plane. By measuring the position of the spots, we estimate the Miller-Bravais indices [30] (1,0,-1,x), where x is between 3 to 10. This position will be further named as pyramidal near-basal plane. The second set of spots is closer to the secondary pyramidal plane (1,1,-2,1). Most of the crystal hemisphere is covered by the protein, except for slightly curved meridian lines running in the direction of the *c*-axis, and an equatorial band on the prismatic planes. The darker spot directly on the basal plane suggests weaker affinity to the plane compared to the near-basal, which is also confirmed by visual observation of the hemisphere etching pattern (**data not shown**).

The six spots near the basal plane form a ring around the center of the basal plane with a symmetrical hexagonal pattern of 12 spots on the whole sphere in total, which is a feature of pyramidal plane binding [32]. This high index near-basal affinity spots are a novel pattern and have not been reported before. Other studied DUF3494 proteins either bind to the basal plane (*Le*IBP [168], *Tis*AFP isoform 6 [95], *Fc*IBP11[109]) or cover the hemisphere completely in FIPA experiments, including the basal plane (*Col*AFP [96], *Sf*IBP_1 [94]).

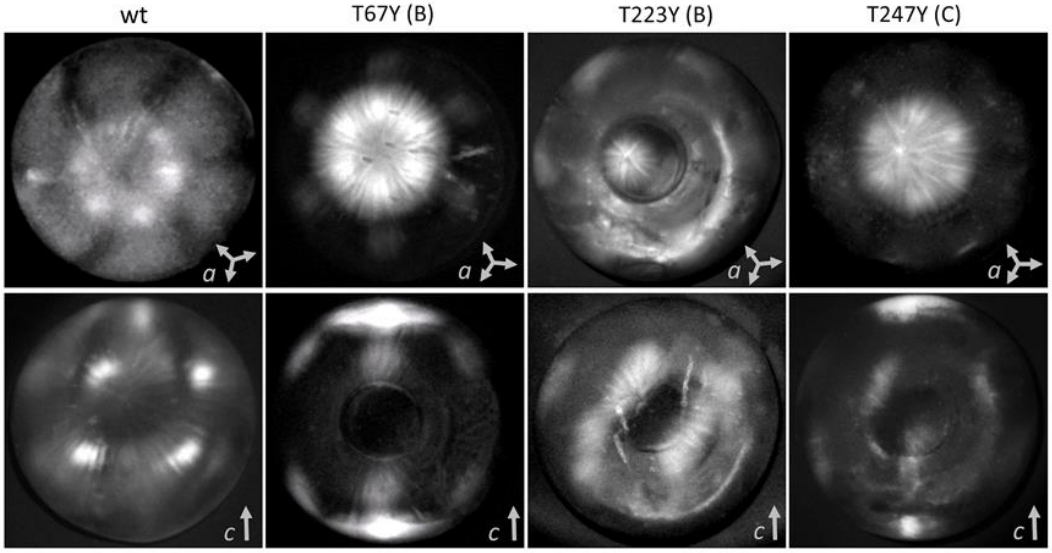

Figure 3. Fluorescence-based ice plane affinity of wt GFP-*Efc*IBP, its B face mutants GFP-T67Y and GFP-T223Y, and C face mutant GFP-T247Y. Crystal axis directions were determined as described in methods and are indicated by arrows.

*Efc*IBP Saturn-like ice crystal shape and bursting direction is consistent with its plane binding specificity. Strong pyramidal near-basal (or basal) affinity, observed with FIPA, prevents the crystal basal plane growth. This makes the formation of bipyramid with a long *c*-axis less likely. Furthermore, most pyramidal angles are covered by the protein, and only prismatic plane is exposed to the solution. This only allows ice crystals growth along the *a*-axis direction and burst as a disc normal to the *c*-axis.

Ice crystals produced by *Le*IBP, a moderate IBP from the DUF3494 family, have been assumed to be bursting in *c*-axis direction, even though this protein has basal plane affinity [72, 168]. However, the binding kinetics and affinity strength of this protein are unknown and might result in *c*-axis

growth; otherwise, it might be that the growth pattern was incorrectly interpreted. Here we established that the *Efc*IBP is indeed inhibiting basal growth through the near-basal binding and does not block prism direction. Still, we note that after crystal burst the ring is very thin. This suggests that the binding to the basal or near-basal plane is fast. To investigate the binding kinetics that are not observable by the FIPA analysis, we performed experiments with fluorescence microscopy of ice grown in a cold microscope stage.

Binding dynamics of GFP-*Efc*IBP

The binding dynamics of GFP-*Efc*IBP were tested in the microfluidics cold finger (MCF) device under fluorescent illumination, and compared to the hyperactive GFP-sbwAFP, known to bind to the basal plane of ice (**Fig. 4**) [36, 170]. Unlike in FIPA, the dynamic of accumulation of GFP-*Efc*IBP can be monitored in the MCF. While in FIPA we note that the preferred accumulation is not exactly on the basal plane, but is in a close proximity, in MCF we observe strong accumulation on the basal plane, which can be distinguished as a straight edge [36] of a mostly round crystal (**Fig. 4**). We acknowledge that in the MCF device the crystallographic orientations of ice are not exposed as they are in the FIPA experiments, therefore near-basal plane binding may be indistinguishable compared to basal plane binding. It is noted that there is no significant difference in the TH values of *Efc*IBP when incubation time is altered before cooling [93]. This is indicative of a moderately active IBP, compared to some hyperactive IBPs, which may accumulate on the basal plane of ice for a few hours [33], thus increasing TH. GFP-*Efc*IBP accumulates on the crystal for approximately one minute, after which it remains constant for at least 20 minutes (**Fig. 4A**). GFP-sbwAFP accumulates on the basal plane for much longer, as is common in hyperactive AFPs (**Fig. 4B**). We note that the higher fluorescence intensity next to the ice surface observed at 0 s is due to pushing protein off the surface of the growing ice front and not to accumulation.

A complementary method useful to study the accumulation kinetics on ice surfaces is to perform experiments between two coverslips and observe free growth of crystals and protein accumulation in semi-2D confinement using fluorescent microscopy. When grown between two coverslips, ice is forced into a height of 10 µm, leading to the growth of truncated crystals when burst. This setup allows for protein accumulation measurements on ice, however results in changes to the crystal shape because of the height constraint. Due to the height confinement, the observed crystals are cross-sections of the shapes that have been observed in the nanoliter osmometer (**Fig. 5 A-F**). The thin bright lines visible in **Figure 5** (B, D, E, F) are truncated ice sheets forced to grow in a very thin layer perpendicular to the image plane. The phenomenon of ice spicules has previously been documented with other IBPs, but in the *c*-axis direction when the growth in the *a* direction was blocked by the proteins [173].

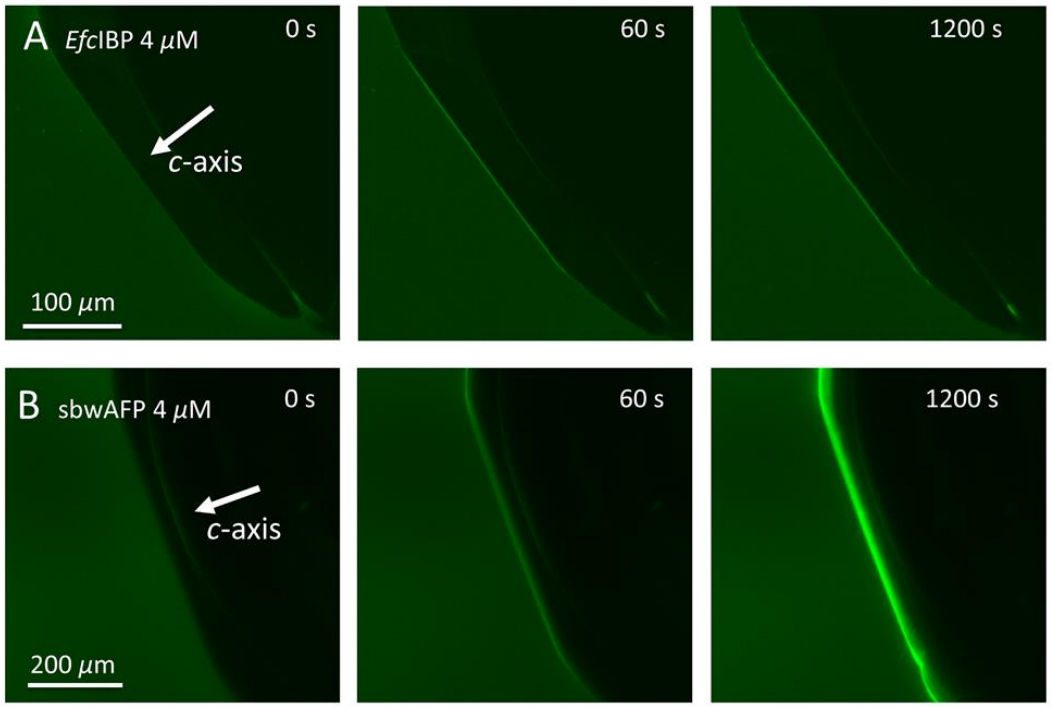

Figure 4. Accumulation of GFP-*Efc*IBP and GFP-sbwAFP to the flat stationary basal plane of ice using the MCF. The ice is the darker area on the top right side. A) 4 μM GFP-*Efc*IBP B) 4 μM GFP-sbwAFP (part of this figure is reprinted with permission).[31] Time legend indicates the number of seconds from the time that the basal plane stopped growing and IBPs started accumulating on the ice front.

In the case of *Efc*IBP, the geometric restriction transformed planar growth into spicule-like growth in the *a* direction on both sides of the crystal, exposing a large basal plane [179]. The crystals show two main orientations when bursting, in which the *c*-axis is at an angle to the coverslips (**Fig. 5 A, B**), and where the *c*-axis is nearly perpendicular relation to the coverslips (**Fig. 5 B-F**). Flat, wide fluorescent ice sheets can be seen (**Fig. 5 D-F**) when the *c*-axis is nearly perpendicular to the coverslips. When the *c*-axis is at an angle to the coverslips, the burst "spicule" can block the growth of other crystals (**Fig. 5 E, F**), as the thin line is a sheet of ice (seen in **Fig. S2B**) spanning from one coverslip to another. As the large ice sheet (crystal 3) seen in Figure 5F grows, it is blocked by a spanning ice sheet (crystal 4), which bends from the force of crystal 3. This is seen in **Movie S2** (18 s). When the two ice crystals collide the spanning ice sheet is bent due to the force of the parallel ice (**Fig. 5F**, crystals 3 and 4). We also note that the large spanning ice sheet (crystal 3) is covered in fluorescent protein. The large sheet is likely the basal plane of ice, which is bound by GFP-*Efc*IBP. This experiment helps to validate the hypothesis that *Efc*IBP is a basal or near basal binder.

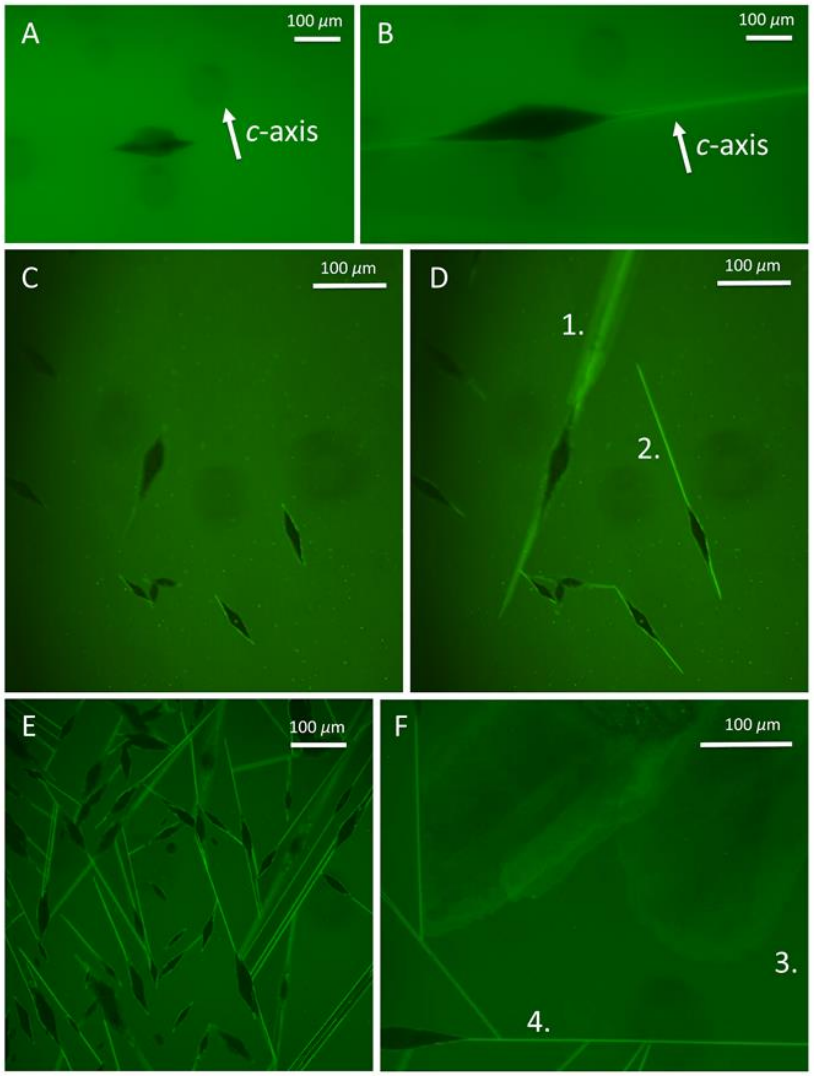

Figure 5. Experiments in 2D confinement in GFP-*Efc*IBP solution. A) A single crystal observed in the TH gap with the *c*-axis parallel to the coverslips. B) The burst pattern of A) is shown. C) Multiple ice crystals observed in the TH gap. D) The burst pattern of C) is shown. The *c*-axis of crystal 1 is tilted to the coverslips, while the rest of the crystals, including crystal 2, are parallel. E, F) The burst pattern of many crystals shows the ice sheet bursts both *c*-axis parallel (shown as a bright line) and tilted (shown as a sheet) in relation to the coverslips. F) Crystals burst perpendicular (crystal 4) to the coverslips can block the growth of neighbouring ice (crystal 3, seen in Movie S2).

Basal plane fluorescence intensity profiles of GFP-*Efc*IBP (**Fig. 6 A-C**) and GFP-sbwAFP (**Fig. 6D**) were analyzed over time and compared to the results obtained from MCF. The accumulation rate value (K_{on}) of each protein can then be calculated from Equation 1 in the Materials and Methods section, as the concentration (C) and time (t) are known (**Fig. 6 E, F**).

The K_{on} values were calculated from both the MCF and coverslip methods separately. The K_{on} value for the basal plane of GFP-*Efc*IBP was found to be 4 ± 1 mM^{-1} s^{-1} between coverslips (truncated sheets) (SD, n=3 for all measurements) and 6 ± 2 mM^{-1} s^{-1} in MCF, while on the pyramidal plane (crystal side, seen in Figures 6E and S4) the average K_{on} value was found to be 2 ± 1 mM^{-1} s^{-1}. The binding of GFP-*Efc*IBP on the

pyramidal plane is therefore approximately the same rate as on the basal plane, however it has a significantly lower fluorescent intensity. On the other hand, K_{on} value of GFP-sbwAFP on the basal plane was found to be an order of magnitude lower: 0.3 ± 0.1 mM^{-1} s^{-1} (coverslips) and 0.6 ± 0.3 mM^{-1} s^{-1} (MCF). These methods agree with one another for both the *Efc*IBP and for the sbwAFP, which show K_{on} values within the standard deviation range. To simplify these findings, we averaged the two rates obtained by each method with weights according to their accuracy. We concluded that the final K_{on} value for GFP-sbwAFP on the basal plane is 0.4 ± 0.2 mM^{-1} s^{-1}. The K_{on} value for GFP-*Efc*IBP on the basal plane is 5 ± 2 mM^{-1} s^{-1}.

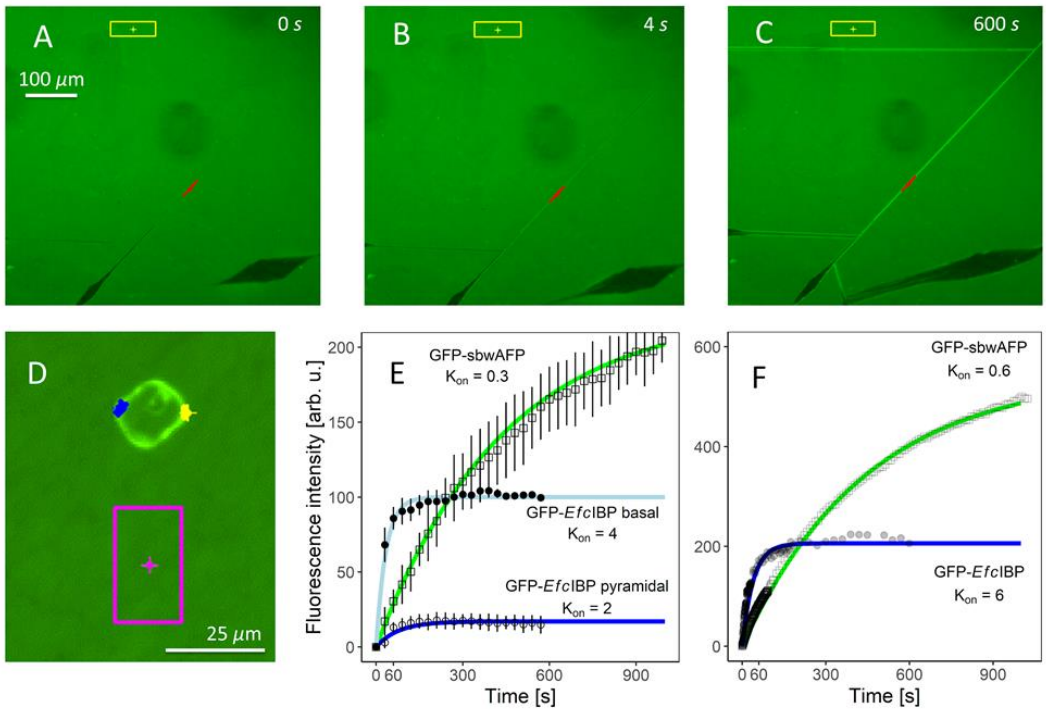

Figure 6. A-C) Bursting ice crystals in 7.6 µM GFP-*Efc*IBP solution between coverslips. Fluorescent measurements represent the difference between the fluorescence of the basal plane (red line) at a given time and the fluorescence at the beginning of accumulation. The background fluorescence (yellow rectangle) was measured during the experiment to confirm that stable conditions were maintained. D) Ice crystal grown in 7.6 µM GFP-sbwAFP solution within the TH gap. Fluorescent measurements represent the difference between the fluorescence of the basal plane (blue and yellow rectangles) at a given time and the fluorescence when the crystal stopped melting and began accumulating protein. The background fluorescence (pink rectangle) was measured during the experiment to confirm that stable conditions were maintained. E) Fluorescence intensity over time of 10 µM GFP-*Efc*IBP (on basal and pyramidal planes) and 7.6 µM GFP-sbwAFP (on basal plane) measured between coverslips. The K_{on} values of GFP-sbwAFP, and GFP-*Efc*IBP are shown (mM^{-1} s^{-1}). Vertical bars represent standard deviation (n=3). F) Fluorescence intensity of 4 µM GFP-*Efc*IBP and 4 µM GFP-sbwAFP in the MCF over time. The K_{on} values of GFP-*Efc*IBP and GFP-sbwAFP are shown (mM^{-1} s^{-1}).

The rapid binding of *Efc*IBP is comparable to the rapid binding of AFP type III, previously determined to be 8 ± 1 mM^{-1} s^{-1} [36]. This indicates that *Efc*IBP and AFP type III bind to ice at a comparable rate. Yet the dramatic difference between the two proteins is which planes the proteins are binding to (basal *vs.* prism). This is a direct and quantitative measurement of the fast accumulation of *Efc*IBP on the basal plane,

which has not been noted before for any IBP. Future research should include elucidating the mechanism that allows this IBP to bind to the basal plane at such a rate.

Previous studies compared the difference between GFP-tagged moderate type III AFP and hyperactive *Tm*AFP from *Tenebrio molitor* and sbwAFP, and revealed that the hyperactive IBPs accumulate relatively slowly on both prism and basal planes and that the accumulation on the basal plane can take hours [33-35, 170]. In contrast, moderate IBPs that were represented by the type III AFP bind fast to the prism plane and cannot bind to the basal plane [33, 35, 36]. Thus, basal plane affinity was denoted as a feature that characterized hyperactive IBPs with high TH. Yet *Efc*IBP has low TH activity and is a fast basal binder compared to sbwAFP and reached a plateau after one minute (**Fig. 6 E, F**). These findings, along with FIPA analysis, indicate that basal plane affinity by its own does not guarantee hyperactivity (high TH), as prismatic binding is important as well. It also demonstrates that basal affinity can be fast and not intrinsically slow as was found in several hyperactive proteins.

Asymmetrical pyramidal binding of GFP-*Efc*IBP

A notable feature of the wt *Efc*IBP FIPA is the overall asymmetry of the binding pattern, which is slightly rotated around the *c*-axis. The bright spots that are closer to the prismatic planes are located on the meridians of *a*-axes, and also are not centered on them, but rather slightly shifted counterclockwise around the *c*-axis. This asymmetric binding observed in FIPA is reflected in the ice crystal shape, which appears as a trapezohedron instead of a symmetric bipyramid.

Such off-axis binding has been reported for fish AFP types I and III [32, 180, 181], yeast *Le*IBP [168], mold fungus *Tis*AFP6 [95], and plant *Dc*AFP (from *Daucus carota*) [182]. All these proteins have a different degree of binding asymmetry even among mutants of the same protein [180] and demonstrate corresponding twisting in the ice crystal shape. This emphasizes the importance of pyramidal binding for the ice crystal shape.

***Efc*IBP mutants**

To further understand the relation between ice binding affinity and different aspects of IBP interaction with ice, we examined mutants of the *Efc*IBP, which were previously described (**Fig. S5**) [118]. These mutants included modifications of ice-binding surfaces on the B and C faces, which drastically affected the TH activity of the mutants. Indeed, the TH activity at 40 μM of B face mutants is 0.04 ℃, 0.06 ℃, and 0.12 ℃ for T67Y, T223Y, and T178Y respectively, while those of C face mutants is 0.22 ℃, 0.1 ℃, and 0.02 ℃ for S188Y, T209Y, and T247Y respectively [118].

The B face mutants T178Y, T223Y, and C face mutants S188Y, T209Y, T247Y had a similar to the wt ice crystal shape with a different degree of asymmetry (**Fig. S6**). However, T67Y produced symmetrical and well-defined hexagonal bifrustum (**Fig. S6**), a model for which is presented in **Figure S2A**. Accordingly, GFP-T67Y mutant has an entirely symmetric FIPA pattern, with no twisting or tilting of spots that is observed in other mutants (**Fig. 3**).

We note that the mutants least active in TH (GFP-T67Y, GFP-T223Y, and GFP-T247Y) retain affinity to the basal or near-basal plane and some generally weak affinity to other pyramidal angles (**Fig. 3**). GFP-T223Y is missing the near-basal ring of spots, indicating that this particular affinity is a feature of a specific region on the B face. The mutants still produce a wide ice crystal shape that grows in the *a*-axis direction (**Fig. S6**), although their TH is an order of magnitude lower compared to the wt [118]. Therefore, basal binding is not sufficient to achieve high TH when pyramidal or prism affinity is low, as seen in the mutants. Hemisphere area covered by the bound IBP in FIPA analysis has been correlated to the

ice growth inhibition by IBPs [181]. In the FIPA picture of the weakest mutant GFP-T247Y we observed a faint signal that covers most of the hemisphere with few stronger spots. Thus, IBP activity is determined not only by the specific ice planes bound by the protein, but also affinity strength and probably accumulation speed.

The FIPA patterns of the B and C face mutants (**Fig. 3**) have affinity spots at different positions than those of the wt. This leads to the conclusion that tyrosine introduced on the B or C faces does not completely switch off the ice-binding site, but instead modifies its planes affinity. It is possible that the water molecules participating in the ice recognition, particularly at the C face, can accommodate the disruption caused by the bulky amino acid.

Docking

To complement the docking studies already published on the wt *Efc*IBP interaction with basal and prismatic planes [118], we provide here the corresponding docking simulation with a pyramidal plane (**Fig. 7**). The docking study was performed with the (1,0,-1,4) pyramidal plane, as representative of a pyramidal plane with low angle to the basal plane. Initial docking results (highest score in terms of steric and electrostatic correlations) show that *Efc*IBP binds the ice pyramidal plane through the B face, the C face and also the surface corresponding to the A face, including the α-helix. The addition of few crystallographic water molecules located in the troughs of the B, C, and A faces (26, 34, and 27 water molecules, respectively) is sufficient to reach a good shape complementarity between the ice pyramidal plane and the B and A faces (SC value of 0.45 for both) and a somewhat lower SC value (0.40) for the C face. The interaction models were further validated by calculating the contact surface areas, which are 1135 $Å^2$, 1305 $Å^2$, and 885 $Å^2$ for B, C, and A faces, respectively. These values are similar in size with those reported for other IBP-1 folded proteins [72, 96, 106]. If compared with the docking results on basal and primary prism planes, the SC and interface analyses suggest that the wt *Efc*IBP binding on the pyramidal plane is less efficient than that to the basal plane (SC 0.53) but better than that hypothesized for the primary prism plane, which is marginally significant with SC 0.39 [118].

Crystal growth behavior

As mentioned before, *Efc*IBP ice crystals grow in a stepwise manner. This stepwise growth is more observable at medium IBP concentration (10 μM), as at a higher concentration there are fewer steps (sometimes no more than one), and at a lower concentration, there is less stabilization between burst steps and growth becomes more continuous. In contrast to *Efc*IBP, hyperactive IBPs do not grow in steps as the cooling progresses to the hysteresis freezing point. Nevertheless, the phenomenon of growth by steps was also observed in other IBPs, but in the *c*-axis direction [29]. When crystals are grown in a microfluidic chip with a height of 40 μm instead of 10 μm, "spicular" growth is not observed due to a tendency of the crystals to orient themselves with the basal plane parallel to the coverslip (Movie S3). Additionally, the crystal in Movie S3 grows and stabilizes in less than 0.3 seconds, showing a typical growth step (note that this is not a full burst).

During cooling ice crystals of the B face mutant T178Y, and C face mutants S188Y, T209Y, similarly to wt, grow in a stepwise manner. Differently, B face mutants T67Y, and T223Y, and C face mutant T247Y demonstrate gradual crystal growth. Such differences can be correlated to the low TH observed (T223Y 15% of wt activity, T67Y 10%, and T247Y 5%) [118]. Nevertheless, during the burst, wt and all mutants grow as thin circular discs in *a*-axis direction (Fig. S6).

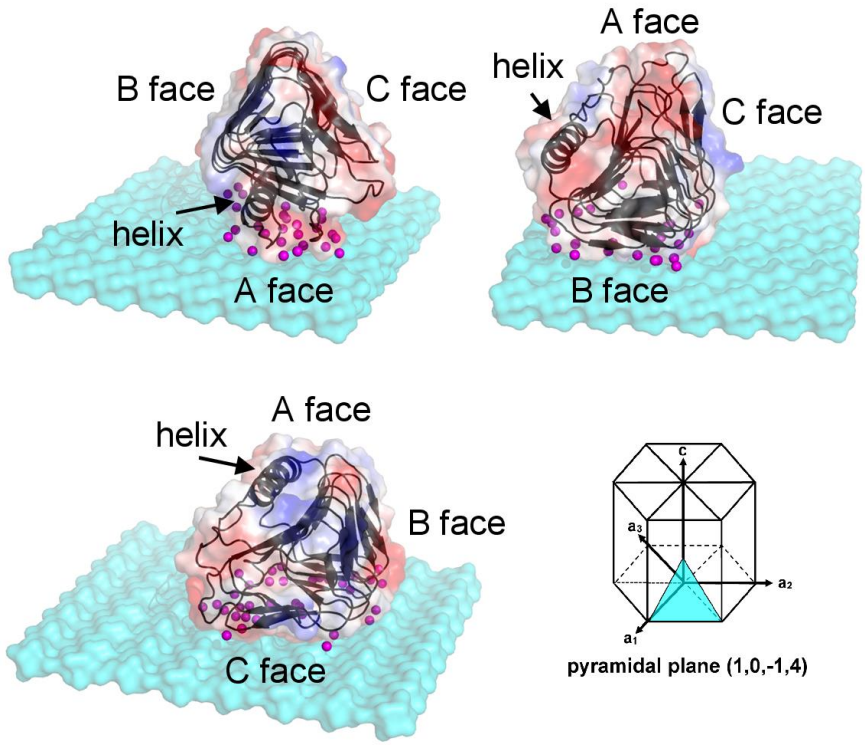

Figure 7. Docking of the wt *Efc*IBP to the ice pyramidal plane. The *Efc*IBP structure is shown as a black cartoon under the semi-transparent protein electrostatic surface. Bound crystallographic water molecules are colored in magenta, ice molecule surface in cyan. On the bottom right, the schematic view of the ice pyramidal plane (1,0,-1,4) is shown.

Ice crystal behavior in 2D confinement within mutant solutions

GFP-*Efc*IBP mutants T67Y, T223Y, and T247Y were placed between coverslips in an attempt to investigate their binding kinetics to ice. Of the six mutants studied, these three mutants show the lowest TH activity.[8] For all three mutants, ice shaping was observed; however, there was no complete block of ice growth, and we did not see the accumulation of fluorescent signal on the ice surface (Fig. S7). Consistently with previous work [118], we see ice recrystallization in a solution of GFP-T247Y, the weakest ice recrystallization inhibitor of the mutants (Fig. S7C).

Conclusion

This study reveals new shaping and plane binding dynamics of the *Efc*IBP that were not described in other IBPs before. Through docking simulations, *Efc*IBP is shown to bind to the basal and pyramidal planes of ice with a higher surface complementarity than to the prism plane. Surprisingly, all three (A, B, and C) faces of the protein show surface complementarity to the pyramidal plane, while only the B and C faces are thought to be used when binding to the basal plane. These docking simulations provide insight into the possible mechanism of *Efc*IBP action.

*Efc*IBP has TH activity, and by that, it can prevent the ice growth and keep crystals stable at a constant temperature within the TH gap but is less effective in preventing ice from growth compared to other IBPs. Lowering the temperature within the TH gap but not below the hysteresis freezing point revealed a stepwise planar growth of the ice crystal. This observed behavior of *Efc*IBP suggests that freezing point depression it is not likely the natural role of this protein. As

was discussed by Mangiagalli *et al*. [93], the *Efc*IBP possesses an N-terminal sequence that is a potential transport signal for excretion. We suggest that the protein is secreted into the local environment around the bacteria and acts to shape and control ice growth. In particular, the fast basal binding by this protein may contribute to the high ability to inhibit ice recrystallization. The experiments show that *Efc*IBP has low TH [93] and fast adsorption dynamics like moderate proteins, but it has a clear basal and near-basal plane affinity with unique fast basal accumulation that was not observed in other known basal binders. While hyperactivity has previously been attributed to basal binding, we stress that this takes the prismatic adsorption into account as well. Here we define a new moderate AFP class, which we term "Moderate Basal Binders," that binds to the basal plane but is a weak prismatic binder. The basal affinity and fast kinetics explain the unique Saturn-like ice burst shape of *Efc*IBP.

It remains to be investigated how fast basal binding by IBPs is important for IRI. This paper provides insight into the properties of *Efc*IBP binding to ice, which may shed light on IBP recrystallization inhibition characteristics.

Materials and Methods

Cloning and mutagenesis

*Efc*IBP and its variants (T67Y, T178Y, T223Y, S188Y, T209Y, and T247Y) were cloned in pET-21a vector [93, 118]. Briefly, the single point mutations were introduced by QuickChange® PCR using pET-21a [*Efc*IBP] as the template as previously described in Mangiagalli *et al* [118].

The GFP-*Efc*IBP chimera was obtained by excision of green fluorescent protein (GFP) gene with *Nde*I (Jena Bioscience, Jena, Germany) from pUC18 [GFP] [165] and cloned into pET-21a [*Efc*IBP] linearized with the same enzyme. The cloning gave raise to pET-21a [GFP-*Efc*IBP] which was verified by restriction analysis and by bidirectional DNA sequencing.

Mutagenesis of GFP-*Efc*IBP to obtain GFP-T67Y, GFP-T223Y and GFP-T247Y variants was carried out by QuickChange® PCR using pET-21a [GFP-*Efc*IBP] as a template and the forward and reverse primers [118]. Reactions were carried out using Q5® High-Fidelity DNA Polymerase (New England Biolabs, Ipswich, MA) and Eppendorf Master-cycler (Eppendorf, Hamburg, Germany) under the following conditions: 1 cycle (98°C for 2 min), 25 cycles (98°C 10 sec, T_A 25 sec and 72°C 180 sec), and a final cycle at 72°C for 3 min. Here T_A is the annealing temperature optimized for each mutant plasmid corresponding to the following temperatures: 66 °C for GFP-T67Y, 67.5°C for GFP-T223Y and 70°C for GFP-T247Y. Mutations were verified by bidirectional DNA sequencing.

Production and purification of recombinant proteins

Escherichia coli strain BL21[DE3] (EMD, Millipore, Billerica, MA, USA) was used as the host for heterologous production of proteins. All the His-tagged proteins used in this study were produced in Zym-5052 medium [132] and purified from the soluble fraction of cell extracts by affinity chromatography [93]. Proteins from more concentrated samples were pooled and buffer exchanged by gel filtration on PD10 column (GE Healthcare, Little Chalfont, UK) against 10 mM ammonium acetate buffer pH 7.0. Purified proteins were lyophilized. *Efc*IBP and its variants were produced and purified at comparable yield (~2 mg from 1 L of culture), while the fusion proteins were produced and purified at higher yield (~5 mg from 1 L of culture).

Protein concentration was determined by the Bradford protein assay (Bio-Rad, Hercules, USA), or the Micro BCA Protein Assay Kit (Thermo Scientific, Rockford, USA), using bovine serum albumin (BSA) as the standard.

Ice growth shapes by the nanoliter osmometer

Ice shaping of *Efc*IBP and its mutants was performed using a custom nanoliter osmometer [14]. Samples contained 3.3-50 μM of protein in 20 mM ammonium bicarbonate buffer (pH 8.5). Single crystals of typically 30 μm diameter were obtained slightly below their melting temperature. Then the temperature was slowly dropped (-0.0025 °C s^{-1}), and the crystal shapes were observed during growth and burst, when growth suddenly becomes fast. Each experiment was repeated several times to observe growth from different *c*-axis orientations.

Fluorescence-based Ice Plane Affinity

Fluorescence-based ice plane affinity (FIPA) was used to determine IBP ice plane binding preference. A modified method of Basu *et al.* [32] was used. Ice monocrystals were grown as described by Knight *et al.* [30]. Plastic or glass beakers were insulated from the sides and filled with 2.5 L of degassed double distilled water. A weighted 50 mL tube with a small hole in the cap was placed on the bottom of each beaker to reduce pressure buildup. The beakers were then left in a freezer at -1 °C for three days, and a slab of ice approximately 6 cm thick grew on top of the water. The ice was then examined through crossed polarizers, and large single crystals were cut out by melting the ice with hot metal plates. The orientation of the *c*-axis was established by careful observation of birefringence color pattern that appears when looking through crossed polarizers [32, 179].

A small oriented single ice crystal block was mounted on a brass cold finger as described by Knight *et al.* [30] A hemispherical glass cup (diameter 60 mm) was filled with cold double distilled water, and the crystal was submerged in the water. The cup and cold finger were enclosed within an isolated styrofoam box. The crystal was then allowed to grow into a 40 mm in diameter hemisphere; then the water was replaced by 50 mL of 0.01-0.07 mg mL^{-1} protein solution in cold 10 mM Tris buffer (pH 8.4). The hemisphere was then allowed to grow at a constant temperature -4.5 °C for 3.5 h until it reached approximately 46 mm in diameter, thus adding a layer of 3 mm of ice to the hemisphere. Cold finger with the hemisphere was then rotated upside down, and the flat part of the sphere was evened out by a warm metal plate. The temperature of the cold finger was then set to +1 °C, and the hemisphere was carefully wiped by a paper tissue to remove non-specifically bound protein [96] and was put into a -18 °C freezer as soon as it detached from the cold finger. The hemisphere was allowed to etch at least overnight and then was imaged in fluorescent light and observed visually. The fluorescent imaging was done inside the -18 °C freezer with a 470 nm LED lamp with a 469 nm GFP excitation filter and a 525 nm GFP emission filter on The Imaging Source DMK 23UP031 (Bremen, Germany) camera.

Ice crystal *a*-axes orientation was determined by pit etching. The hemisphere was covered with plastic wrap, and a small hole was made with a needle in the center of the basal plane. The hemisphere was then put into a lyophilizer for 15-30 min until a clearly visible hexagonal hole appeared. Sides of the hexagonal pit coincide with the primary prism planes of the ice crystal lattice [183].

Microfluidic cold finger

The microfluidic cold finger (MCF) system used here has been described previously in detail [36]. Briefly, a microfluidic device containing a copper tip (cold finger) was placed on a LabVIEW-controlled cold stage mounted on a fluorescence microscope (Ti Eclipse, Nikon, Japan), and a sCMOS camera (Neo 5.5 sCMOS, Andor, UK) was used for video capture and analysis. The experiment started by flowing 5 μL BSA solution (10 mg mL^{-1}) for 20 min. Then, double distilled water was flown through the

MCF to remove unbound BSA. The stage temperature was then lowered until the water in the MCF was frozen around -25 °C, after which the temperature of the stage was increased slowly to the ice melting point, while the temperature of the cold finger was kept a few degrees below melting temperature. The temperature of the stage was then reduced to allow growth of the crystal, which was controlled by independently adjusting the temperatures of the cold-finger and the metal stage beneath the sample, forming a temperature gradient. The stage was warmed and cooled until only one or two parallel flat planes were observed, indicating the presence of a single crystal. At this point, GFP-*Efc*IBP or GFP-sbwAFP was injected in the MFC, surrounding and adsorbing to the ice crystal. Then the temperature was lowered to grow a new basal plane. The protein-bound ice crystal was observed by fluorescence microscopy for 20 min. Image analysis was performed using NIS Elements AR software (Nikon, Tokyo, Japan). Fluorescent measurements represent the difference between the fluorescence at a given time and the fluorescence at the time that the ice crystal stopped growing and started accumulating protein at the moment the basal plane became stationary.

Crystal growth in 2D confinement

The fluorescence experiment between two coverslips was also based on the cold stage setup described for MCF and followed the method by Pertaya *et al*. [178] and Celik *et al*. [34]. A sample of 1.6 µL containing GFP-*Efc*IBP or GFP-sbwAFP (in 10 mM Tris-HCl pH 8.0, 20 mM NaCl) in different concentrations was placed on a sapphire slide and covered with a 16-mm diameter circular glass coverslip, or was placed in a microfluidic device similar to that described above, without a cold finger, with a height of 40 µm. The gap between the sapphire and the coverslip was sealed by immersion oil to prevent drying of the sample. The sapphire was placed on a copper slab with a 2-mm diameter hole to observe the fluorescence. The combination of sapphire and a small hole was designed to minimize temperature gradients in the sample. Oil was placed between the copper stage and the sapphire to improve the thermal contact. The stage temperature was then lowered until the solution froze, typically at -25 °C. The temperature was then raised past the melting point until only a few crystals remained. The temperature of the stage was then slowly lowered until crystal growth and burst as "spicules". The stationary protein-bound ice was observed for 15 minutes in fluorescent light. Image analysis was performed using NIS Elements AR software (Nikon, Tokyo, Japan). Fluorescent measurements represent the difference between the fluorescence at a given time and the fluorescence at the start of accumulation when the ice front became stationary. The binding kinetics of the IBPs were then calculated by fitting measured fluorescence intensity I to the Equation 1:

$$I = I_{max}(1 - e^{-t/\tau}) \qquad \text{Equation 1}$$

This equation was previously proposed to describe AFP type III accumulation kinetics on ice [33]. Here τ is a typical accumulation time and is equal to $\frac{1}{K_{on}C}$.

Protein-ice docking

Docked model for *Efc*IBP and ice pyramidal plane (1,0,-1,4), with the minimum overall docking score, was performed with the program HEX 8.0.0 [164], using default parameters except for correlation type (shape + electrostatics). The shape complementarities (SC) of the *Efc*IBP–ice interfaces for the resulting models were calculated using the SC program [156] and the surface contact determined with the program AreaIMol [184].

ACKNOWLEDGMENTS

This work was partly supported by a grant Progetto Nazionale di Ricerche in Antartide PEA 2014–2016 and the RISE-MSCA Project 'Metable' to ML. IB acknowledges

support by European Research Council (grant No. 281595) and by Israel Science Foundation (grant No. 930/16). AK acknowledges support by European Regional Development Fund. We thank Sivan Ben Bassat for TH measurements.

AUTHOR CONTRIBUTIONS

The manuscript was written through contributions of all authors. All authors have given approval to the final version of the manuscript. [#]These authors contributed equally.

Supplementary materials

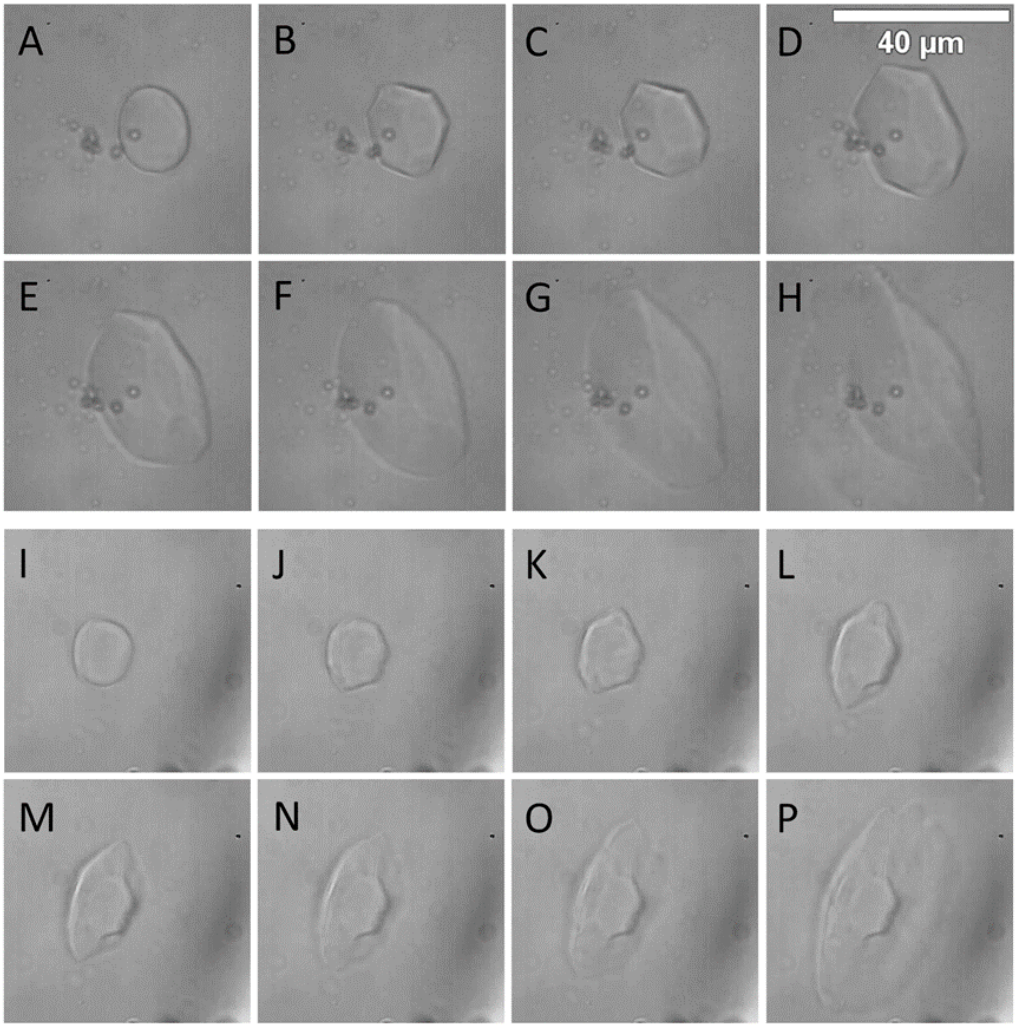

Figure S1. Ice crystal growth and burst in A-H) 10 µM *Efc*IBP and I-P) in 25 µM GFP-*Efc*IBP. Letters indicate the sequence of frames.

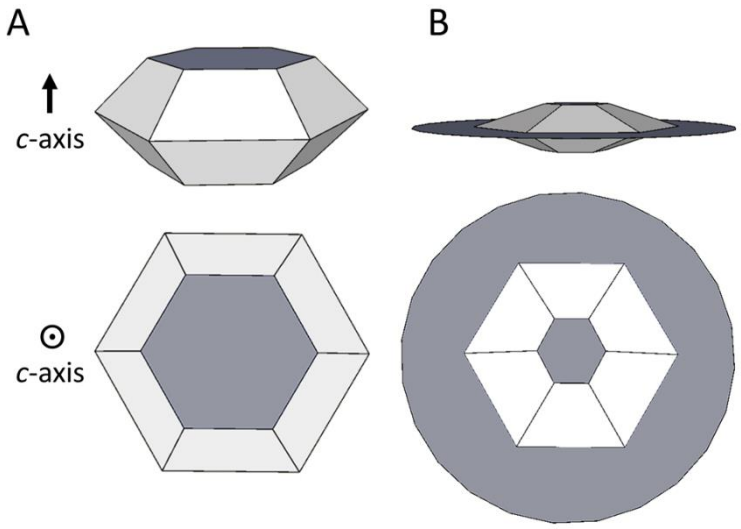

Figure S2. Models of ice crystal shapes formed in *Efc*IBP solutions. A) Hexagonal bifrustum, ice crystal shape formed by the T67Y mutant. B) A simplified model of Saturn-shaped burst perpendicular to the *c*-axis. For simplicity, the example is given for the T67Y mutant.

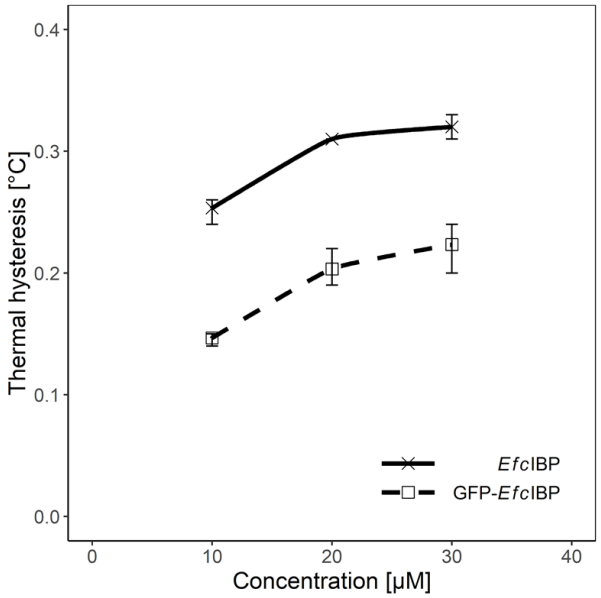

Figure S3. Thermal hysteresis activity of *Efc*IBP compared to GFP-*Efc*IBP. Each point presents the average of three independent measurements, with 95% confidence intervals.

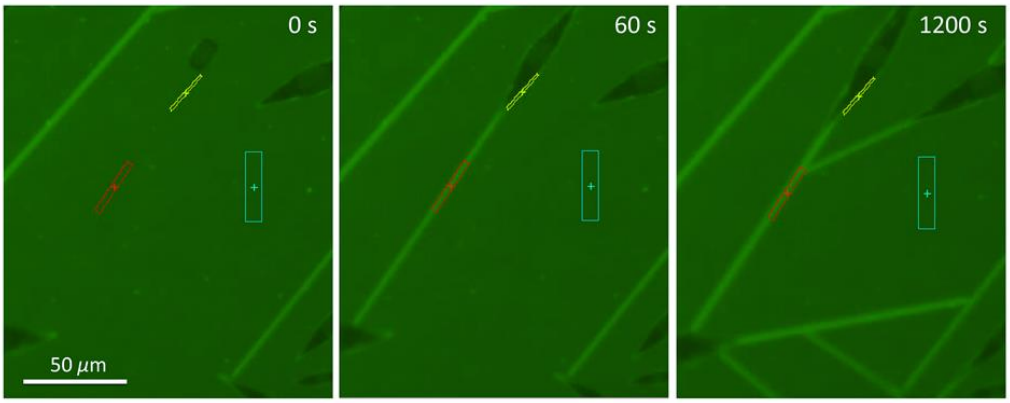

Figure S4. Wild type *Efc*IBP accumulation on ice crystals. Colored rectangles show areas of fluorescence intensity measurements: red - basal plane (truncated sheet), yellow - pyramidal plane (crystal side), cyan - background.

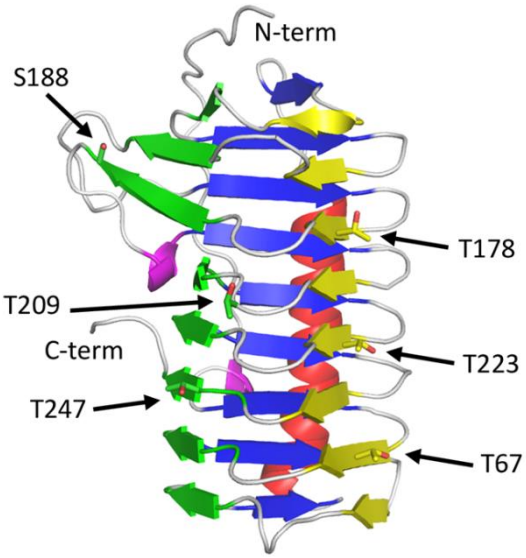

Figure S5. *Efc*IBP mutation sites. Mutated residues on the B (yellow) and C (green) faces of the *Efc*IBP structure are shown as sticks and indicated by arrows and labels.

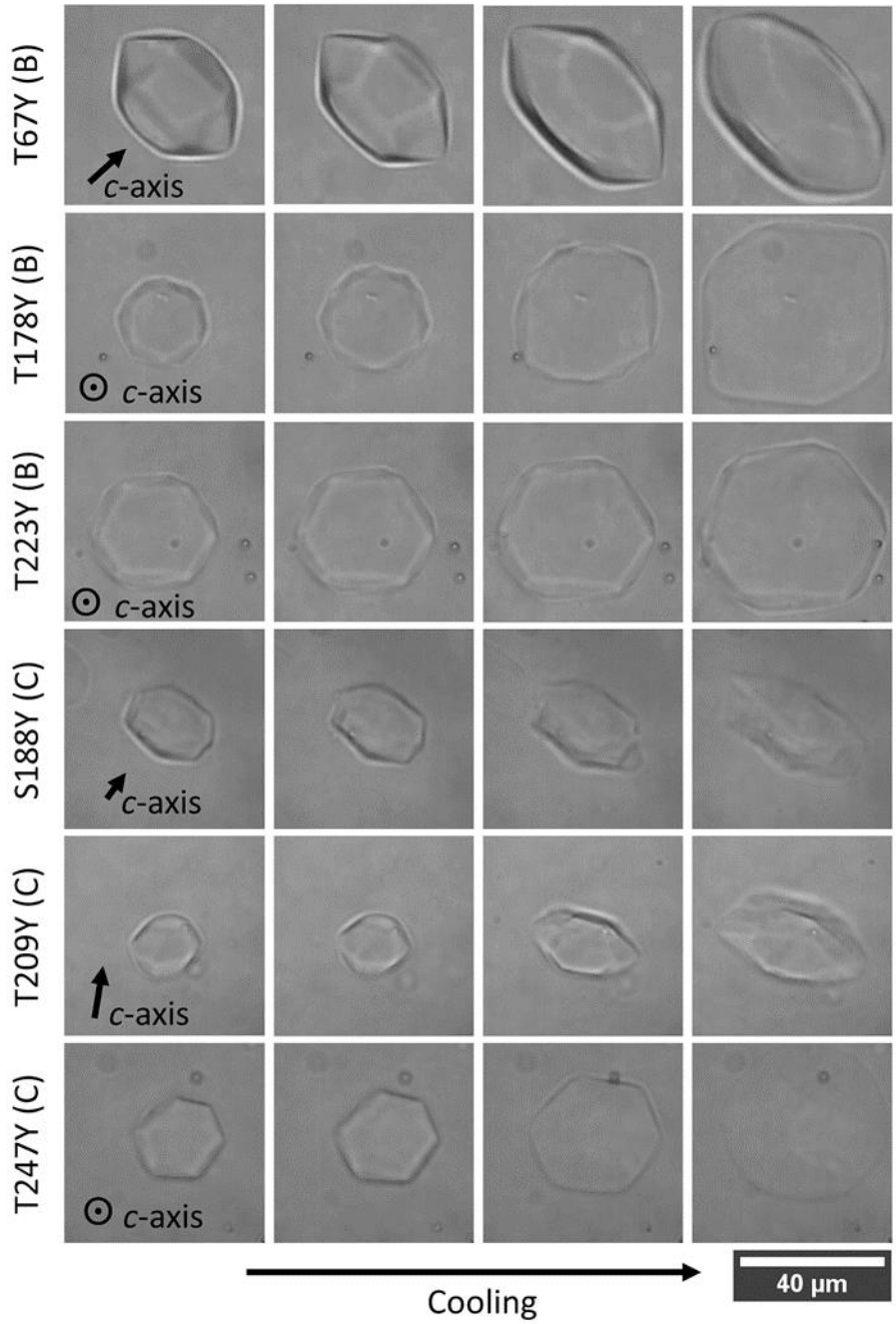

Figure S6. Ice crystal shapes and their growth pattern during cooling in solutions of *Efc*IBP mutants. The letter in parenthesis indicates the protein face that was mutated. T67Y, T178Y, T223Y, and T209Y are 10 µM; S188Y 3.3 µM; T247Y 50 µM. The circled dot indicates *c*-axis normal to the image plane.

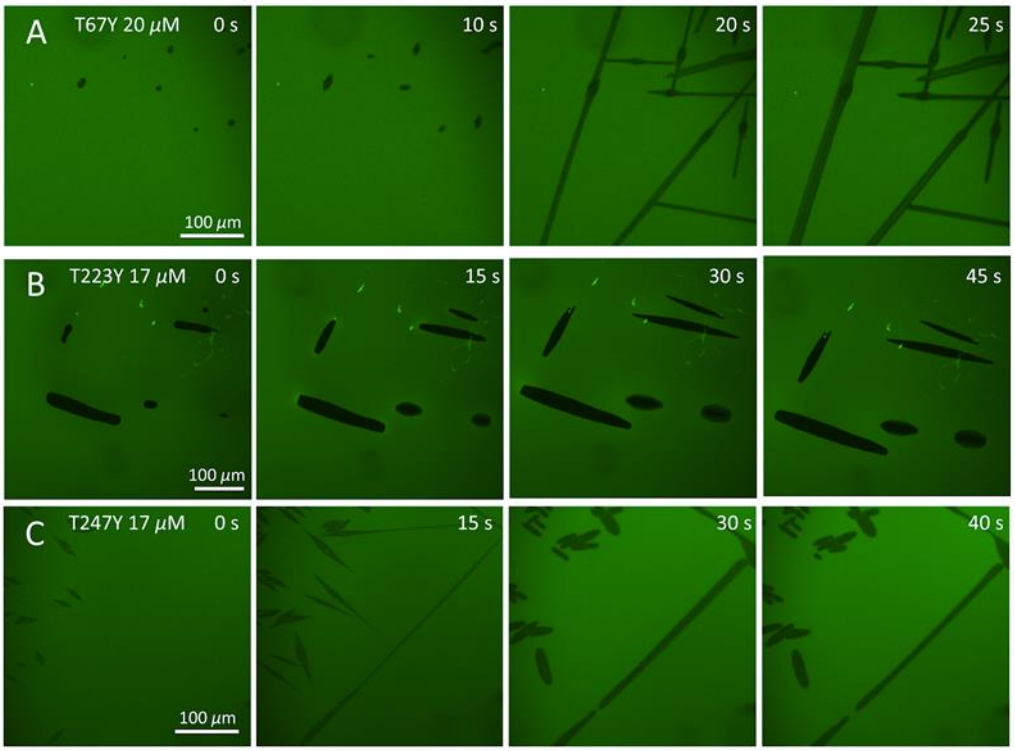

Figure S7. GFP-*Efc*IBP mutants growth and burst after cooling below the TH freezing point, as seen between two coverslips. After the burst, the temperature is held constant. A) GFP-T67Y mutant at 20 μM. B) GFP-T223Y mutant at 17 μM. C) GFP-T247Y mutant at 17 μM.

Movie S1. Ice crystal growth and burst in the wt *Efc*IBP 5 μM solution during cooling.
la8b01914_si_008.avi

Movie S2. Ice crystals burst in 7.6 μM GFP-*Efc*IBP solution. A growing parallel ice sheet is blocked by a perpendicular ice sheet (tilted *a*-axis).
la8b01914_si_009.avi

Movie S3. Single ice crystal in 10 μM GFP-*Efc*IBP grown in a microfluidic chip with a height of 40 μm. Photos were taken with a time interval of 0.3 seconds. The edge of the PDMS chip can be seen in the frame as curved lines around the ice crystal.
la8b01914_si_010.avi

4. References

1. De Maayer, P., Anderson, D., Cary, C. & Cowan, D. A. (2014) Some like it cold: understanding the survival strategies of psychrophiles, *EMBO reports*, e201338170.
2. D'Amico, S., Collins, T., Marx, J. C., Feller, G. & Gerday, C. (2006) Psychrophilic microorganisms: challenges for life, *Embo Reports.* **7**, 385-389.
3. Pischedda, A., Ramasamy, K. P., Mangiagalli, M., Chiappori, F., Milanesi, L., Miceli, C., Pucciarelli, S. & Lotti, M. (2018) Antarctic marine ciliates under stress: superoxide dismutases from the psychrophilic Euplotes focardii are cold-active yet heat tolerant enzymes., *Scientific reports.* **8**, 14721.
4. Mazur, P. (1984) Freezing of living cells: mechanisms and implications, *American Journal of Physiology-Cell Physiology.* **247**, C125-C142.
5. Meryman, H. T. (1971) Osmotic stress as a mechanism of freezing injury, *Cryobiology.* **8**, 489-500.
6. Bar Dolev, M., Braslavsky, I. & Davies, P. L. (2016) Ice-binding proteins and their function, *Annual review of biochemistry.* **85**, 515-542.
7. Davies, P. L. (2014) Ice-binding proteins: a remarkable diversity of structures for stopping and starting ice growth, *Trends in Biochemical Sciences.* **39**, 548-555.
8. DeVries, A. L. & Wohlschlag, D. E. (1969) Freezing resistance in some Antarctic fishes, *Science (New York, NY).* **163**, 1073-5.
9. Voets, I. K. (2017) From ice-binding proteins to bio-inspired antifreeze materials, *Soft Matter*. **13**, 4808-4823.
10. Poynting, J. H. (1881) Change of state: Solid-liquid in *Philosophical Magazine* pp. 32-48.
11. Raymond, J. A. & DeVries, A. L. (1977) Adsorption inhibition as a mechanism of freezing resistance in polar fishes, *Proceedings of the National Academy of Sciences.* **74**, 2589-2593.
12. Kristiansen, E. & Zachariassen, K. E. (2005) The mechanism by which fish antifreeze proteins cause thermal hysteresis, *Cryobiology.* **51**, 262-280.

13. Raymond, J. A. (1992) Glycerol is a colligative antifreeze in some northern fishes, *Journal of Experimental Zoology Part A: Ecological Genetics and Physiology*. **262**, 347-352.

14. Braslavsky, I. & Drori, R. (2013) LabVIEW-operated Novel Nanoliter Osmometer for Ice Binding Protein Investigations, *Jove-Journal of Visualized Experiments*. **72**, e4189.

15. Scotter, A. J., Marshall, C. B., Graham, L. A., Gilbert, J. A., Garnham, C. P. & Davies, P. L. (2006) The basis for hyperactivity of antifreeze proteins, *Cryobiology*. **53**, 229-239.

16. Mangiagalli, M., Brocca, S., Orlando, M., & Lotti, M. (in submission) The "cold revolution". Present and future applications of cold-active enzymes and ice-binding proteins. *New Biotechnology Journal*.

17. Hassas-Roudsari, M. & Goff, H. D. (2012) Ice structuring proteins from plants: Mechanism of action and food application, *Food Research International*. **46**, 425-436.

18. Knight, C. A. & Duman, J. G. (1986) Inhibition of recrystallization of ice by insect thermal hysteresis proteins: a possible cryoprotective role, *Cryobiology*. **23**, 256-262.

19. Capicciotti, C. J., Doshi, M. & Ben, R. N. (2013) Ice Recrystallization Inhibitors: From Biological Antifreezes to Small Molecules in Recent developments in the study of recrystallization, Intech. doi: 10.5772/54992.

20. Huang, Z., Su, M., Yang, Q., Li, Z., Chen, S., Li, Y., Zhou, X., Li, F. & Song, Y. (2017) A general patterning approach by manipulating the evolution of two-dimensional liquid foams, *Nature communications.* **8**, 14110.

21. Fennema, O. R., Powrie, W. D. & Marth, E. H. (1973) Low temperature preservation of foods and living matter in *Low temperature preservation of foods and living matter* (Fennema, O. R. P., W. D. & Marth, E. H., eds) pp. 151-227.

22. Zaritzky, N. (2006) Physical–chemical principles in freezing in *Handbook of frozen food processing and packaging* (Sun, D., ed) pp. 23-25, Florida: taylor and Francis Group.

23. Knight, C. A., Hallett, J. & DeVries, A. L. (1988) Solute effects on ice recrystallization: an assessment technique, *Cryobiology*. **25**, 55-60.

24. Budke, C., Heggemann, C., Koch, M., Sewald, N. & Koop, T. (2009) Ice recrystallization kinetics in the presence of synthetic antifreeze glycoprotein analogues using the framework of LSW theory, *The Journal of Physical Chemistry B.* **113**, 2865-2873.

25. Budke, C., Dreyer, A., Jaeger, J., Gimpel, K., Berkemeier, T., Bonin, A. S., Nagel, L., Plattner, C., DeVries, A. L. & Sewald, N. (2014) Quantitative efficacy classification of ice recrystallization inhibition agents, *Crystal Growth & Design.* **14**, 4285-4294.

26. Olijve, L. L. C., Meister, K., DeVries, A. L., Duman, J. G., Guo, S., Bakker, H. J. & Voets, I. K. (2016) Blocking rapid ice crystal growth through nonbasal plane adsorption of antifreeze proteins, *Proceedings of the National Academy of Sciences.* **113**, 3740-3745.

27. Vance, T. D. R., Bayer-Giraldi, M., Davies, P. L., & Mangiagalli, M. (in revision) Ice-binding proteins and the 'domain of unknown function' 3494 family *The FEBS journal.*

28. Pauling, L. (1935) The structure and entropy of ice and of other crystals with some randomness of atomic arrangement, *Journal of the American Chemical Society.* **57**, 2680-2684.

29. Bar-Dolev, M., Celik, Y., Wettlaufer, J. S., Davies, P. L. & Braslavsky, I. (2012) New insights into ice growth and melting modifications by antifreeze proteins, *Journal of the Royal Society Interface.* **9**, 3249-3259.

30. Knight, C. A., Cheng, C. C. & DeVries, A. L. (1991) Adsorption of alpha-helical antifreeze peptides on specific ice crystal surface planes, *Biophysical journal.* **59**, 409-418.

31. Knight, C. A., Wierzbicki, A., Laursen, R. A. & Zhang, W. (2001) Adsorption of biomolecules to ice and their effects upon ice growth. 1. Measuring adsorption orientations and initial results, *Crystal Growth & Design.* **1**, 429-438.

32. Basu, K., Garnham, C. P., Nishimiya, Y., Tsuda, S., Braslavsky, I. & Davies, P. (2014) Determining the ice-binding planes of antifreeze proteins by fluorescence-based ice plane affinity, *Journal of visualized experiments: JoVE*. **83**, e51185.

33. Drori, R., Celik, Y., Davies, P. L. & Braslavsky, I. (2014) Ice-binding proteins that accumulate on different ice crystal planes produce distinct thermal hysteresis dynamics, *Journal of The Royal Society Interface.* **11**, 20140526.

34. Celik, Y., Drori, R., Pertaya-Braun, N., Altan, A., Barton, T., Bar-Dolev, M., Groisman, A., Davies, P. L. & Braslavsky, I. (2013) Microfluidic experiments reveal that antifreeze proteins bound to ice crystals suffice to prevent their growth, *Proceedings of the National Academy of Sciences.* **110**, 1309-1314.

35. Drori, R., Davies, P. L. & Braslavsky, I. (2015) When are antifreeze proteins in solution essential for ice growth inhibition?, *Langmuir*. **31**, 5805-5811.

36. Haleva, L., Celik, Y., Bar-Dolev, M., Pertaya-Braun, N., Kaner, A., Davies, P. L. & Braslavsky, I. (2016) Microfluidic Cold-Finger Device for the Investigation of Ice-Binding Proteins, *Biophysical journal.* **111**, 1143-1150.

37. Lindow, S. E. (1983) The role of bacterial ice nucleation in frost injury to plants, *Annual review of phytopathology.* **21**, 363-384.

38. Maki, L. R., Galyan, E. L., Chang-Chien, M.-M. & Caldwell, D. R. (1974) Ice nucleation induced by Pseudomonas syringae, *Applied microbiology.* **28**, 456-459.

39. Kawahara, H., Nakano, Y., Omiya, K., Muryoi, N., Nishikawa, J. & Obata, H. (2004) Production of two types of ice crystal-controlling proteins in Antarctic bacterium, *Journal of bioscience and bioengineering.* **98**, 220-223.

40. Garnham, C. P., Campbell, R. L., Walker, V. K. & Davies, P. L. (2011) Novel dimeric β-helical model of an ice nucleation protein with bridged active sites, *BMC structural biology.* **11**, 36.

41. Graether, S. P. & Jia, Z. (2001) Modeling Pseudomonas syringae ice-nucleation protein as aβ-helical protein, *Biophysical journal.* **80**, 1169-1173.

42. Kobashigawa, Y., Nishimiya, Y., Miura, K., Ohgiya, S., Miura, A. & Tsuda, S. (2005) A part of ice nucleation protein exhibits the ice-binding ability, *FEBS letters.* **579**, 1493-1497.

43. Drori, R., Davies, P. L. & Braslavsky, I. (2015) Experimental correlation between thermal hysteresis activity and the distance between antifreeze proteins on an ice surface, *RSC Advances.* **5**, 7848-7853.

44. Knight, C. A., Driggers, E. & DeVries, A. L. (1993) Adsorption to ice of fish antifreeze glycopeptides 7 and 8, *Biophysical journal.* **64**, 252-259.

45. Chao, H., Houston, M. E., Hodges, R. S., Kay, C. M., Sykes, B. D., Loewen, M. C., Davies, P. L. & Sönnichsen, F. D. (1997) A diminished role for hydrogen bonds in antifreeze protein binding to ice, *Biochemistry.* **36**, 14652-14660.

46. Sönnichsen, F. D., DeLuca, C. I., Davies, P. L. & Sykes, B. D. (1996) Refined solution structure of type III antifreeze protein: hydrophobic groups may be involved in the energetics of the protein–ice interaction, *Structure.* **4**, 1325-1337.

47. Nutt, D. R. & Smith, J. C. (2008) Dual function of the hydration layer around an antifreeze protein revealed by atomistic molecular dynamics simulations, *Journal of the American Chemical Society.* **130**, 13066-13073.

48. Garnham, C. P., Gilbert, J. A., Hartman, C. P., Campbell, R. L., Laybourn-Parry, J. & Davies, P. L. (2008) A Ca2+-dependent bacterial antifreeze protein domain has a novel beta-helical ice-binding fold, *Biochemical Journal.* **411**, 171-180.

49. Liou, Y.-C., Tocilj, A., Davies, P. L. & Jia, Z. (2000) Mimicry of ice structure by surface hydroxyls and water of a β-helix antifreeze protein, *Nature.* **406**, 322-324.

50. Duman, J. G. (2001) Antifreeze and ice nucleator proteins in terrestrial arthropods, *Annual Review of Physiology.* **63**, 327-357.

51. Fletcher, G. L., Hew, C. L. & Davies, P. L. (2001) Antifreeze proteins of teleost fishes, *Annual review of physiology.* **63**, 359-390.

52. Sidebottom, C., Buckley, S., Pudney, P., Twigg, S., Jarman, C., Holt, C., Telford, J., McArthur, A., Worrall, D., Hubbard, R. & Lillford, P. (2000) Phytochemistry - Heat-stable antifreeze protein from grass, *Nature.* **406**, 256-256.

53. Middleton, A. J., Brown, A. M., Davies, P. L. & Walker, V. K. (2009) Identification of the ice-binding face of a plant antifreeze protein, *Febs Letters.* **583**, 815-819.

54. Middleton, A. J., Marshall, C. B., Faucher, F., Bar-Dolev, M., Braslavsky, I., Campbell, R. L., Walker, V. K. & Davies, P. L. (2012) Antifreeze Protein from Freeze-Tolerant Grass Has a Beta-Roll Fold with an Irregularly Structured Ice-Binding Site, *Journal of Molecular Biology.* **416**, 713-724.

55. Raymond, J. A., Fritsen, C. & Shen, K. (2007) An ice-binding protein from an Antarctic sea ice bacterium, *FEMS microbiology ecology.* **61**, 214-221.

56. Raymond, J. A., Janech, M. G. & Fritsen, C. H. (2009) Novel ice-binding proteins from a psychrophilic antarctic alga (Chlamydomonadaceae, Chlorophyceae) 1, *Journal of phycology.* **45**, 130-136.

57. Raymond, J. A. & Morgan-Kiss, R. (2013) Separate origins of ice-binding proteins in Antarctic Chlamydomonas species, *PloS one.* **8**, e59186.

58. Raymond, J. A. (2016) Dependence on epiphytic bacteria for freezing protection in an Antarctic moss, Bryum argenteum, *Environmental microbiology reports.* **8**, 14-19.

59. Guo, S., Garnham, C. P., Whitney, J. C., Graham, L. A. & Davies, P. L. (2012) Re-evaluation of a bacterial antifreeze protein as an adhesin with ice-binding activity, *PloS one.* **7**, e48805.

60. Guo, S., Stevens, C. A., Vance, T. D. R., Olijve, L. L. C., Graham, L. A., Campbell, R. L., Yazdi, S. R., Escobedo, C., Bar-Dolev, M. & Yashunsky, V. (2017) Structure of a 1.5-MDa adhesin that binds its Antarctic bacterium to diatoms and ice, *Science advances.* **3**, e1701440.

61. Cochet, N. & Widehem, P. (2000) Ice crystallization by Pseudomonas syringae, *Applied microbiology and biotechnology.* **54**, 153-161.

62. Sicheri, F. & Yang, D. S. C. (1995) Ice-binding structure and mechanism of an antifreeze protein from winter flounder, *Nature.* **375**, 427-431.

63. Jia, Z., DeLuca, C. I., Chao, H. & Davies, P. L. (1996) Structural basis for the binding of a globular antifreeze protein to ice, *Nature.* **384**, 285-288.

64. Liu, Y., Li, Z., Lin, Q., Kosinski, J., Seetharaman, J., Bujnicki, J. M., Sivaraman, J. & Hew, C.-L. (2007) Structure and evolutionary origin of Ca2+-dependent herring type II antifreeze protein, *PLoS One.* **2**, e548.

65. Gauthier, S. Y., Scotter, A. J., Lin, F.-H., Baardsnes, J., Fletcher, G. L. & Davies, P. L. (2008) A re-evaluation of the role of type IV antifreeze protein, *Cryobiology.* **57**, 292-296.

66. Deng, G., Andrews, D. W. & Laursen, R. A. (1997) Amino acid sequence of a new type of antifreeze protein, from the longhorn sculpin Myoxocephalus octodecimspinosis, *FEBS letters.* **402**, 17-20.

67. Harding, M. M., Anderberg, P. I. & Haymet, A. D. J. (2003) 'Antifreeze'glycoproteins from polar fish, *European journal of biochemistry.* **270**, 1381-1392.

68. Feeney, R. E., Burcham, T. S. & Yeh, Y. (1986) Antifreeze glycoproteins from polar fish blood, *Annual review of biophysics and biophysical chemistry.* **15**, 59-78.

69. Hakim, A., Nguyen, J. B., Basu, K., Zhu, D. F., Thakral, D., Davies, P. L., Isaacs, F. J., Modis, Y. & Meng, W. (2013) Crystal Structure of an Insect Antifreeze Protein and Its Implications for Ice Binding, *Journal of Biological Chemistry.* **288**, 12295-12304.

70. Pentelute, B. L., Gates, Z. P., Tereshko, V., Dashnau, J. L., Vanderkooi, J. M., Kossiakoff, A. A. & Kent, S. B. H. (2008) X-ray structure of snow flea antifreeze protein determined by racemic crystallization of synthetic protein enantiomers, *Journal of the American Chemical Society.* **130**, 9695-9701.

71. Lee, J. H., Park, A. K., Do, H., Park, K. S., Moh, S. H., Chi, Y. M. & Kim, H. J. (2012) Structural basis for antifreeze activity of ice-binding protein from arctic yeast, *Journal of Biological Chemistry.* **287**, 11460-11468.

72. Kondo, H., Hanada, Y., Sugimoto, H., Hoshino, T., Garnham, C. P., Davies, P. L. & Tsuda, S. (2012) Ice-binding site of snow mold fungus antifreeze protein deviates from structural regularity and high conservation, *Proceedings of the National Academy of Sciences.* **109**, 9360-9365.

73. Graham, L. A., Lougheed, S. C., Ewart, K. V. & Davies, P. L. (2008) Lateral Transfer of a Lectin-Like Antifreeze Protein Gene in Fishes, *Plos One.* **3**, e2616.

74. Graether, S. P., Kuiper, M. J., Gagne, S. M., Walker, V. K., Jia, Z. C., Sykes, B. D. & Davies, P. L. (2000) beta-helix structure and ice-binding properties of a hyperactive antifreeze protein from an insect, *Nature.* **406**, 325-328.

75. Marshall, C. B., Daley, M. E., Graham, L. A., Sykes, B. D. & Davies, P. L. (2002) Identification of the ice-binding face of antifreeze protein from Tenebrio molitor, *FEBS letters.* **529**, 261-267.

76. Basu, K., Wasserman, S. S., Jeronimo, P. S., Graham, L. A. & Davies, P. L. (2016) Intermediate activity of midge antifreeze protein is due to a tyrosine-rich ice-binding site and atypical ice plane affinity, *The FEBS journal.* **283**, 1504-1515.

77. Ustun, N. S. & Turhan, N. (2015) Antifreeze Proteins: Characteristics, Function, Mechanism of Action, Sources and Application to Foods in, Journal of Food Processing and Preservation,

78. Feeney, R. E. Y., Y. (1998) Antifreeze proteins: current status and possible food uses, *Trends in Food Science & Technology*. **9**, 102-106.

79. Kaleda, A., Tsanev, R., Klesment, T., Vilu, R. & Laos, K. (2018) Ice cream structure modification by ice-binding proteins, *Food chemistry.* **246**, 164-171.

80. Kim, H. J., Lee, J. H., Hur, Y. B., Lee, C. W., Park, S.-H. & Koo, B.-W. (2017) Marine antifreeze proteins: structure, function, and application to cryopreservation as a potential cryoprotectant, *Marine drugs.* **15**, 27.

81. Makarevich, A. V., Kubovičová, E., Popelková, M., Fabian, D., Čikoš, Š., Pivko, J. & Chrenek, P. (2010) Several aspects of animal embryo cryopreservation: anti-freeze protein (AFP) as a potential cryoprotectant, *Zygote.* **18**, 145-153.

82. Bakhach, J. (2009) The cryopreservation of composite tissues: principles and recent advancement on cryopreservation of different type of tissues, *Organogenesis.* **5**, 119-126.

83. Fahy, G. M. (1986) The relevance of cryoprotectant "toxicity" to cryobiology, *Cryobiology.* **23**, 1-13.

84. Fahy, G. M., Lilley, T. H., Linsdell, H., Douglas, M. S. J. & Meryman, H. T. (1990) Cryoprotectant toxicity and cryoprotectant toxicity reduction: in search of molecular mechanisms, *Cryobiology.* **27**, 247-268.

85. Kim, H. J., Shim, H. E., Lee, J. H., Kang, Y.-C. & Hur, Y. B. (2015) Ice-binding protein derived from Glaciozyma can improve the viability of cryopreserved mammalian cells, *J Microbiol Biotechnol.* **25**, 1989-1996.

86. Nishijima, K., Tanaka, M., Sakai, Y., Koshimoto, C., Morimoto, M., Watanabe, T., Fan, J. & Kitajima, S. (2014) Effects of type III antifreeze protein on sperm and embryo cryopreservation in rabbit, *Cryobiology.* **69**, 22-25.

87. Rubinsky, B. & DeVries, A. L. (1989) Effect of ice crystal habit on the viability of glycerol-protected red blood cells, *Cryobiology.* **26**, 580.

88. Wang, T., Zhu, Q., Yang, X., Layne Jr, J. R. & Devries, A. L. (1994) Antifreeze glycoproteins from antarctic notothenioid fishes fail to protect the rat cardiac explant during hypothermic and freezing preservation, *Cryobiology.* **31**, 185-192.

89. Mugnano, J. A., Wang, T., Layne Jr, J. R., DeVries, A. L. & Lee Jr, R. E. (1995) Antifreeze glycoproteins promote intracellular freezing of rat cardiomyocytes at high subzero temperatures, *American Journal of Physiology-Regulatory, Integrative and Comparative Physiology.* **269**, R474-R479.

90. Bowman, J. P. (2017) Genomics of Psychrophilic Bacteria and Archaea in *Psychrophiles: From Biodiversity to Biotechnology* pp. 345-387, Springer.

91. Bayer-Giraldi, M., Weikusat, I., Besir, H. & Dieckmann, G. (2011) Characterization of an antifreeze protein from the polar diatom Fragilariopsis cylindrus and its relevance in sea ice, *Cryobiology.* **63**, 210-219.

92. Gwak, I. G., sic Jung, W., Kim, H. J., Kang, S.-H. & Jin, E. (2010) Antifreeze protein in Antarctic marine diatom, Chaetoceros neogracile, *Marine biotechnology*. **12**, 630-639.

93. Mangiagalli, M., Bar-Dolev, M., Tedesco, P., Natalello, A., Kaleda, A., Brocca, S., de Pascale, D., Pucciarelli, S., Miceli, C., Braslavsky, I. & Lotti, M. (2017) Cryo-protective effect of an ice-binding protein derived from Antarctic bacteria, *Febs Journal.* **284**, 163-177.

94. Vance, T. D. R., Graham, L. A. & Davies, P. L. (2018) An ice-binding and tandem beta-sandwich domain-containing protein in Shewanella frigidimarina is a potential new type of ice adhesin, *The FEBS journal*. **285**, 1511-1527.

95. Cheng, J., Hanada, Y., Miura, A., Tsuda, S. & Kondo, H. (2016) Hydrophobic ice-binding sites confer hyperactivity of an antifreeze protein from a snow mold fungus, *Biochemical Journal.* **473**, 4011-4026.

96. Hanada, Y., Nishimiya, Y., Miura, A., Tsuda, S. & Kondo, H. (2014) Hyperactive antifreeze protein from an Antarctic sea ice bacterium Colwellia sp has a compound ice-binding site without repetitive sequences, *Febs Journal.* **281**, 3576-3590.

97. Wang, C., Oliver, E. E., Christner, B. C. & Luo, B.-H. (2016) Functional Analysis of a bacterial antifreeze protein indicates a cooperative effect between its two ice-binding domains, *Biochemistry*. **55**, 3975-3983.

98. Hashim, N. H. F., Sulaiman, S., Bakar, F. D. A., Illias, R. M., Kawahara, H., Najimudin, N., Mahadi, N. M. & Murad, A. M. A. (2014) Molecular cloning, expression and characterisation of Afp4, an antifreeze protein from Glaciozyma antarctica, *Polar Biology.* **37**, 1495-1505.

99. Xiao, N., Hanada, Y., Seki, H., Kondo, H., Tsuda, S. & Hoshino, T. (2014) Annealing condition influences thermal hysteresis of fungal type ice-binding proteins, *Cryobiology.* **68**, 159-161.

100. Davies, P. L. (2016) Antarctic moss is home to many epiphytic bacteria that secrete antifreeze proteins, *Environmental Microbiology Reports*. **8**, 1-2.

101. Sorhannus, U. (2011) Evolution of antifreeze protein genes in the diatom genus fragilariopsis: evidence for horizontal gene transfer, gene duplication and episodic diversifying selection, *Evolutionary Bioinformatics.* **7**, 279.

102. Bayer-Giraldi, M., Uhlig, C., John, U., Mock, T. & Valentin, K. (2010) Antifreeze proteins in polar sea ice diatoms: diversity and gene expression in the genus Fragilariopsis, *Environmental microbiology.* **12**, 1041-1052.

103. Raymond, J. A. & Kim, H. J. (2012) Possible role of horizontal gene transfer in the colonization of sea ice by algae, *PloS one.* **7**, e35968.

104. Kiko, R. (2010) Acquisition of freeze protection in a sea-ice crustacean through horizontal gene transfer?, *Polar Biology.* **33**, 543-556.

105. Raymond, J. A. (2011) Algal ice-binding proteins change the structure of sea ice, *Proceedings of the National Academy of Sciences.* **108**, E198-E198.

106. Do, H., Kim, S. J., Kim, H. J. & Lee, J. H. (2014) Structure-based characterization and antifreeze properties of a hyperactive ice-binding protein from the Antarctic bacterium Flavobacterium frigoris PS1, *Acta Crystallographica Section D: Biological Crystallography.* **70**, 1061-1073.

107. Kondo, H., Mochizuki, K. & Bayer-Giraldi, M. (2018) Multiple binding Modes of a moderate Ice-binding Protein from a polar Microalga, *Physical Chemistry Chemical Physics*. **20**, 25295-25303.

108. Wang, C., Pakhomova, S., Newcomer, M. E., Christner, B. C. & Luo, B.-H. (2017) Structural basis of antifreeze activity of a bacterial multi-domain antifreeze protein, *PloS one.* **12**, e0187169.

109. Bayer-Giraldi, M., Sazaki, G., Nagashima, K., Kipfstuhl, S., Vorontsov, D. A. & Furukawa, Y. (2018) Growth suppression of ice crystal basal face in the presence of a moderate ice-binding protein does not confer hyperactivity, *Proceedings of the National Academy of Sciences*. **115**, 7479–7484.

110. Banach, M., Konieczny, L. & Roterman, I. (2018) Why do antifreeze proteins require a solenoid?, *Biochimie*. **144**, 74-84.

111. DeLuca, C. I., Comley, R. & Davies, P. L. (1998) Antifreeze proteins bind independently to ice, *Biophysical journal.* **74**, 1502-1508.

112. Baardsnes, J., Kuiper, M. J. & Davies, P. L. (2003) Antifreeze protein dimer when two ice-binding faces are better than one, *Journal of Biological Chemistry.* **278**, 38942-38947.

113. Marshall, C. B., Daley, M. E., Sykes, B. D. & Davies, P. L. (2004) Enhancing the activity of a β-helical antifreeze protein by the engineered addition of coils, *Biochemistry.* **43**, 11637-11646.

114. Valbonesi, A. & Luporini, P. (1993) Biology of Euplotes focardii, an Antarctic ciliate, *Polar Biology.* **13**, 489-493.

115. Pucciarelli, S., La Terza, A., Ballarini, P., Barchetta, S., Yu, T., Marziale, F., Passini, V., Methe, B., Detrich, H. W., III & Miceli, C. (2009) Molecular cold-adaptation of protein function and gene regulation: The case for comparative genomic analyses in marine ciliated protozoa, *Marine Genomics.* **2**, 57-66.

116. Orsi, W., Charvet, S., Vd'acny, P., Bernhard, J. M. & Edgcomb, V. P. (2012) Prevalence of partnerships between bacteria and ciliates in oxygen-depleted marine water columns, *Frontiers in Microbiology.* 3, 341.

117. Pucciarelli, S., Chiappori, F., Devaraj, R. R., Yang, G., Yu, T., Ballarini, P. & Miceli, C. (2014) Identification and analysis of two sequences encoding ice-binding proteins obtained from a putative bacterial symbiont of the psychrophilic Antarctic ciliate Euplotes focardii, *Antarctic Science.* **26**, 491-501.

118. Mangiagalli, M., Sarusi, G., Kaleda, A., Bar Dolev, M., Nardone, V., Vena, V. F., Braslavsky, I., Lotti, M. & Nardini, M. (2018) Structure of a bacterial ice binding protein with two faces of interaction with ice, *Febs Journal.* **285**, 1653-1666.

119. Peralta, M. D. R., Karsai, A., Ngo, A., Sierra, C., Fong, K. T., Hayre, N. R., Mirzaee, N., Ravikumar, K. M., Kluber, A. J. & Chen, X. (2015) Engineering amyloid fibrils from β-solenoid proteins for biomaterials applications, *ACS nano.* **9**, 449-463.

120. Bryan, A. W., Starner-Kreinbrink, J. L., Hosur, R., Clark, P. L. & Berger, B. (2011) Structure-based prediction reveals capping motifs that inhibit β-helix aggregation, *Proceedings of the National Academy of Sciences.* **108**, 11099-11104.

121. Hudait, A., Moberg, D. R., Qiu, Y., Odendahl, N., Paesani, F. & Molinero, V. (2018) Preordering of water is not needed for ice recognition by hyperactive antifreeze proteins, *Proceedings of the National Academy of Sciences*. **115**, 8266–8271.

122. Kaleda, A., Haleva, L., Sarusi, G., Pinsky, T., Mangiagalli, M., Bar-Dolev, M., Lotti, M., Nardini, M. & Braslavsky, I. (2018) Saturn-shaped ice burst pattern and fast basal binding of an ice-binding protein from an Antarctic bacterial consortium., *Langmuir : the ACS journal of surfaces and colloids* doi: 10.1021/acs.langmuir.8b01914.

123. Garnham, C. P., Campbell, R. L. & Davies, P. L. (2011) Anchored clathrate waters bind antifreeze proteins to ice, *Proceedings of the National Academy of Sciences of the United States of America.* **108**, 7363-7367.

124. Bouvet, V. & Ben, R. N. (2003) Antifreeze glycoproteins - Structure, conformation, and biological applications, *Cell Biochemistry and Biophysics.* **39**, 133-144.

125. DeVries, A. L. & Lin, Y. (1977) *The role of glycoprotein antifreezes in the survival of Antarctic fishes.*

126. Knight, C. A., DeVries, A. L. & Oolman, L. D. (1984) Fish antifreeze protein and the freezing and recrystallization of ice, *Nature.* **308**, 295-6.

127. Raymond, J. A. (2014) The ice-binding proteins of a snow alga, Chloromonas brevispina: probable acquisition by horizontal gene transfer, *Extremophiles.* **18**, 987-994.

128. Yang, G., De Santi, C., de Pascale, D., Pucciarelli, S., Pucciarelli, S. & Miceli, C. (2013) Characterization of the first eukaryotic cold-adapted patatin-like phospholipase from the psychrophilic Euplotes focardii: identification of putative

determinants of thermal-adaptation by comparison with the homologous protein from the mesophilic Euplotes crassus, *Biochimie.* **95**, 1795-1806.

129. Pucciarelli, S., Devaraj, R. R., Mancini, A., Ballarini, P., Castelli, M., Schrallhammer, M., Petroni, G. & Miceli, C. (2015) Microbial Consortium Associated with the Antarctic Marine Ciliate Euplotes focardii: An Investigation from Genomic Sequences, *Microbial ecology*, 1-14.

130. Sigrist, C. J. A., de Castro, E., Cerutti, L., Cuche, B. A., Hulo, N., Bridge, A., Bougueleret, L. & Xenarios, I. (2013) New and continuing developments at PROSITE, *Nucleic Acids Research.* **41**, E344-E347.

131. Petersen, T. N., Brunak, S., von Heijne, G. & Nielsen, H. (2011) SignalP 4.0: discriminating signal peptides from transmembrane regions, *Nature Methods.* **8**, 785-786.

132. Studier, F. W. (2005) Protein production by auto-induction in high-density shaking cultures, *Protein Expression and Purification.* **41**, 207-234.

133. Byler, D. M. & Susi, H. (1986) Examination of the secondary structure of proteins by deconvolved FTIR spectra, *Biopolymers.* **25**, 469-487.

134. Barth, A. (2007) Infrared spectroscopy of proteins, *Biochimica et Biophysica Acta (BBA)-Bioenergetics.* **1767**, 1073-1101.

135. Cerf, E., Sarroukh, R., Tamamizu-Kato, S., Breydo, L., Derclaye, S., Dufrêne, Y., Narayanaswami, V., Goormaghtigh, E., Ruysschaert, J. & Raussens, V. (2009) Antiparallel beta-sheet: a signature structure of the oligomeric amyloid beta-peptide, *Biochem J.* **421**, 415-423.

136. Graham, L. A., Liou, Y. C., Walker, V. K. & Davies, P. L. (1997) Hyperactive antifreeze protein from beetles, *Nature.* **388**, 727-728.

137. Hughes, S. & Graether, S. P. (2011) Cryoprotective mechanism of a small intrinsically disordered dehydrin protein, *Protein Science.* **20**, 42-50.

138. Finn, R. D., Coggill, P., Eberhardt, R. Y., Eddy, S. R., Mistry, J., Mitchell, A. L., Potter, S. C., Punta, M., Qureshi, M. & Sangrador-Vegas, A. (2016) The Pfam

protein families database: towards a more sustainable future, *Nucleic acids research.* **44**, D279-D285.

139. Xiao, N., Suzuki, K., Nishimiya, Y., Kondo, H., Miura, A., Tsuda, S. & Hoshino, T. (2010) Comparison of functional properties of two fungal antifreeze proteins from Antarctomyces psychrotrophicus and Typhula ishikariensis, *FEBS journal.* **277**, 394-403.

140. Uhlig, C., Kilpert, F., Frickenhaus, S., Kegel, J. U., Krell, A., Mock, T., Valentin, K. & Beszteri, B. (2015) In situ expression of eukaryotic ice-binding proteins in microbial communities of Arctic and Antarctic sea ice, *The ISME journal*. **277**, 394-403.

141. Robert, X. & Gouet, P. (2014) Deciphering key features in protein structures with the new ENDscript server, *Nucleic acids research.* **42**, W320-W324.

142. Sambi, I., Gatti-Lafranconi, P., Longhi, S. & Lotti, M. (2010) How disorder influences order and vice versa - mutual effects in fusion proteins containing an intrinsically disordered and a globular protein, *Febs Journal.* **277**, 4438-4451.

143. DeLuca, C. I., Comley, R. & Davies, P. L. (1998) Antifreeze proteins bind independently to ice, *Biophys J.* **74**, 1502-1508.

144. Laemmli, U. K. (1970) Cleavage of structural proteins during the assembly of the head of bacteriophage T4, *nature.* **227**, 680-685.

145. Biasini, M., Bienert, S., Waterhouse, A., Arnold, K., Studer, G., Schmidt, T., Kiefer, F., Cassarino, T. G., Bertoni, M. & Bordoli, L. (2014) SWISS-MODEL: modelling protein tertiary and quaternary structure using evolutionary information, *Nucleic acids research*, gku340.

146. Pertaya, N., Celik, Y., DiPrinzio, C. L., Wettlaufer, J. S., Davies, P. L. & Braslavsky, I. (2007) Growth-melt asymmetry in ice crystals under the influence of spruce budworm antifreeze protein, *Journal of Physics-Condensed Matter.* **19**.

147. Regand, A. & Goff, H. D. (2006) Ice recrystallization inhibition in ice cream as affected by ice structuring proteins from winter wheat grass, *Journal of dairy science.* **89**, 49-57.

148. Jones, D. T., Taylor, W. R. & Thornton, J. M. (1992) The rapid generation of mutation data matrices from protein sequences, *Computer applications in the biosciences: CABIOS.* **8**, 275-282.

149. Felsenstein, J. (1985) Confidence limits on phylogenies: an approach using the bootstrap, *Evolution*, 783-791.

150. Tamura, K., Peterson, D., Peterson, N., Stecher, G., Nei, M. & Kumar, S. (2011) MEGA5: molecular evolutionary genetics analysis using maximum likelihood, evolutionary distance, and maximum parsimony methods, *Molecular biology and evolution.* **28**, 2731-2739.

151. DeVries, A. L., Komatsu, S. K. & Feeney, R. E. (1970) Chemical and physical properties of freezing point-depressing glycoproteins from Antarctic fishes, *Journal of Biological Chemistry.* **245**, 2901-2908.

152. Devries, A. L. & Lin, Y. (1977) Structure of a peptide antifreeze and mechanism of adsorption to ice, *Biochimica et Biophysica Acta (BBA)-Protein Structure.* **495**, 388-392.

153. Leinala, E. K., Davies, P. L. & Jia, Z. C. (2002) Crystal structure of beta-helical antifreeze protein points to a general ice binding model, *Structure.* **10**, 619-627.

154. Knight, C. A., De Vries, A. L. & Oolman, L. D. (1984) Fish antifreeze protein and the freezing and recrystallization of ice, *Nature.* **308**, 295-296.

155. Capicciotti, C. J., Poisson, J. S., Boddy, C. N. & Ben, R. N. (2015) Modulation of antifreeze activity and the effect upon post-thaw HepG2 cell viability after cryopreservation, *Cryobiology.* **70**, 79-89.

156. Lawrence, M. C. & Colman, P. M. (1993) Shape complementarity at protein/protein interfaces, *Journal of molecular biology.* **234**, 946-950.

157. Kabsch, W. (2010) Xds, *Acta Crystallographica Section D: Biological Crystallography.* **66**, 125-132.

158. Evans, P. (2006) Scaling and assessment of data quality, *Acta Crystallographica Section D: Biological Crystallography.* **62**, 72-82.

159. Storoni, L. C., McCoy, A. J. & Read, R. J. (2004) Likelihood-enhanced fast rotation functions, *Acta Crystallographica Section D: Biological Crystallography.* **60**, 432-438.

160. Emsley, P. & Cowtan, K. (2004) Coot: model-building tools for molecular graphics, *Acta Crystallographica Section D: Biological Crystallography.* **60**, 2126-2132.

161. Murshudov, G. N., Vagin, A. A. & Dodson, E. J. (1997) Refinement of macromolecular structures by the maximum-likelihood method, *Acta Crystallographica Section D: Biological Crystallography.* **53**, 240-255.

162. Adams, P. D., Afonine, P. V., Bunkóczi, G., Chen, V. B., Davis, I. W., Echols, N., Headd, J. J., Hung, L. W., Kapral, G. J. & Grosse-Kunstleve, R. W. (2010) PHENIX: a comprehensive Python-based system for macromolecular structure solution, *Acta Crystallographica Section D: Biological Crystallography.* **66**, 213-221.

163. Chen, V. B., Arendall, W. B., Headd, J. J., Keedy, D. A., Immormino, R. M., Kapral, G. J., Murray, L. W., Richardson, J. S. & Richardson, D. C. (2010) MolProbity: all-atom structure validation for macromolecular crystallography, *Acta Crystallographica Section D: Biological Crystallography.* **66**, 12-21.

164. Ritchie, D. W. & Venkatraman, V. (2010) Ultra-fast FFT protein docking on graphics processors, *Bioinformatics.* **26**, 2398-2405.

165. Tedeschi, G., Mangiagalli, M., Chmielewska, S., Lotti, M., Natalello, A. & Brocca, S. (2017) Aggregation properties of a disordered protein are tunable by pH and depend on its net charge per residue, *Biochimica Et Biophysica Acta-General Subjects.* **1861**, 2543-2550.

166. Schindelin, J., Arganda-Carreras, I., Frise, E., Kaynig, V., Longair, M., Pietzsch, T., Preibisch, S., Rueden, C., Saalfeld, S. & Schmid, B. (2012) Fiji: an open-source platform for biological-image analysis, *Nature methods.* **9**, 676-682.

167. Celik, Y., Graham, L. A., Mok, Y.-F., Bar, M., Davies, P. L. & Braslavsky, I. (2010) Superheating of ice crystals in antifreeze protein solutions, *Proceedings of the National Academy of Sciences of the United States of America.* **107**, 5423-5428.
168. Park, K. S., Do, H., Lee, J. H., Park, S. I., jung Kim, E., Kim, S.-J., Kang, S.-H. & Kim, H. J. (2012) Characterization of the ice-binding protein from Arctic yeast Leucosporidium sp. AY30, *Cryobiology.* **64**, 286-296.
169. Davies, P. L., Baardsnes, J., Kuiper, M. J. & Walker, V. K. (2002) Structure and function of antifreeze proteins, *Philosophical Transactions of the Royal Society of London B: Biological Sciences.* **357**, 927-935.
170. Pertaya, N., Marshall, C. B., Celik, Y., Davies, P. L. & Braslavsky, I. (2008) Direct visualization of spruce budworm antifreeze protein interacting with ice crystals: basal plane affinity confers hyperactivity, *Biophysical journal.* **95**, 333-341.
171. Wilson, P. W., Beaglehole, D. & DeVries, A. L. (1993) Antifreeze glycopeptide adsorption on single crystal ice surfaces using ellipsometry, *Biophysical journal.* **64**, 1878-1884.
172. Chapsky, L. & Rubinsky, B. (1997) Kinetics of antifreeze protein-induced ice growth inhibition, *FEBS letters.* **412**, 241-244.
173. Knight, C. A. & DeVries, A. L. (2009) Ice growth in supercooled solutions of a biological "antifreeze", AFGP 1–5: An explanation in terms of adsorption rate for the concentration dependence of the freezing point, *Physical Chemistry Chemical Physics.* **11**, 5749-5761.
174. Takamichi, M., Nishimiya, Y., Miura, A. & Tsuda, S. (2007) Effect of annealing time of an ice crystal on the activity of type III antifreeze protein, *The FEBS journal.* **274**, 6469-6476.
175. Bredow, M., Tomalty, H. E., Smith, L. & Walker, V. K. (2018) Ice and anti-nucleating activities of an ice-binding protein from the annual grass, Brachypodium distachyon, *Plant, cell & environment.* **41**, 983-992.

176. Hoshino, T., Kiriaki, M., Ohgiya, S., Fujiwara, M., Kondo, H., Nishimiya, Y., Yumoto, I. & Tsuda, S. (2003) Antifreeze proteins from snow mold fungi, *Canadian Journal of Botany.* **81**, 1175-1181.

177. Do, H., Lee, J. H., Lee, S. G. & Kim, H. J. (2012) Crystallization and preliminary X-ray crystallographic analysis of an ice-binding protein (FfIBP) from Flavobacterium frigoris PS1, *Acta Crystallographica Section F: Structural Biology and Crystallization Communications.* **68**, 806-809.

178. Pertaya, N., Marshall, C. B., DiPrinzio, C. L., Wilen, L., Thomson, E. S., Wettlaufer, J. S., Davies, P. L. & Braslavsky, I. (2007) Fluorescence microscopy evidence for quasi-permanent attachment of antifreeze proteins to ice surfaces, *Biophysical Journal.* **92**, 3663-3673.

179. Petrenko, V. F. & Whitworth, R. W. (1999) *Physics of ice*, OUP Oxford.

180. Garnham, C. P., Nishimiya, Y., Tsuda, S. & Davies, P. L. (2012) Engineering a naturally inactive isoform of type III antifreeze protein into one that can stop the growth of ice, *Febs Letters.* **586**, 3876-3881.

181. Mahatabuddin, S., Hanada, Y., Nishimiya, Y., Miura, A., Kondo, H., Davies, P. L. & Tsuda, S. (2017) Concentration-dependent oligomerization of an alpha-helical antifreeze polypeptide makes it hyperactive, *Scientific reports.* **7**, 42501.

182. Meyer, K., Keil, M. & Naldrett, M. J. (1999) A leucine-rich repeat protein of carrot that exhibits antifreeze activity, *Febs Letters.* **447**, 171-178.

183. Brumberg, A., Hammonds, K., Baker, I., Backus, E. H. G., Bisson, P. J., Bonn, M., Daghlian, C. P., Mezger, M. & Shultz, M. J. (2017) Single-crystal Ih ice surfaces unveil connection between macroscopic and molecular structure, *Proceedings of the National Academy of Sciences.* **114**, 5349-5354.

184. Winn, M. D., Ballard, C. C., Cowtan, K. D., Dodson, E. J., Emsley, P., Evans, P. R., Keegan, R. M., Krissinel, E. B., Leslie, A. G. W. & McCoy, A. (2011) Overview of the CCP4 suite and current developments, *Acta Crystallographica Section D.* **67**, 235-242.